Inclusive Reconstruction of the Λ^0 Hyperon at Center-of-Mass Energies from 4.13 GeV to 4.44 GeV at BESIII

Dissertation zur Erlangung des Grades
"Doktor der Naturwissenschaften"

am Fachbereich Physik, Institut für Kernphysik Frankfurt,
der Goethe-Universität Frankfurt

vorgelegt von Mathilde Himmelreich
aus Frankfurt am Main

Frankfurt am Main, 22. November 2022

Vom Fachbereich Physik der
Johann Wolfgang Goethe-Universität als Dissertation angenommen.

Dekan: Prof. Dr. Harald Appelshäuser

Gutachter: Prof. Dr. Klaus Peters
Prof. Dr. Miriam Fritsch

Datum der Disputation: 29.06.2023

Abstract

In the last twenty years, a variety of unexpected resonances had been observed within the charmonium mass region. Although the existence of unconventional states has been predicted by the quantum chromodynamics (QCD), a quantum field theory describing the strong force, a clear evidence was missing. The $Y(4260)$ is such an unexpected and supernummerary state, first observed at BaBar in 2005, and aroused great interest, because it couples much stronger to hidden charm decays ($c\bar{c}$ states like J/ψ or h_c) instead of open charm decays (D meson pairs). This is unusual for states with masses above the $D\bar{D}$ threshold. Furthermore, it decays into a charged exotic state $Y(4260) \to Z_c(3900)^{\pm}\pi^{\mp}$. The charge of the $Z_c(3900)^{\pm}$ is an indication that it comprises of two more quarks than the $c\bar{c}$ pair, and could therefore be assumed to be a four-quark state. Due to these still not understood properties of these QCD-allowed states, they are referred to as exotic XYZ states to emphasize their particularity.

In 2017, the collaboration of the Beijing Spectrometer III (BESIII) investigated the production reaction of the $Y(4260)$ resonance based on a high-luminosity data set. This significantly improved precision of the measurement of the cross-section $\sigma(e^+e^- \to J/\psi\pi^+\pi^-)$ permitted a resolution into two resonances, the $Y(4230)$ and the $Y(4360)$. The $Z_c(3900)^{\pm}$ had been discovered by the BESIII collaboration in 2013, thus this experiment at the Beijing Electron-Positron Collider II (BEPCII) is a top-performing facililty to study exotic charmonium-like states.

In this work, an inclusive reconstruction of the strange hyperon Λ^0 in the charmonium mass region is performed to study possible decays of Y states in order to provide further insight into their nature. Finding more states or new decay channels may provide crucial hints to understand the strong interaction beyond nonperturbative approaches.

Three resonances are observed in the energy dependent cross-section: the first with a mass of (4222.01 ± 5.68) MeV and a width of (154.26 ± 28.16) MeV, the second with a mass of (4358.88 ± 4.97) MeV and a width of (49.58 ± 13.54) MeV and the third with a mass of (4416.41 ± 2.37) MeV and a width of (23.88 ± 7.18) MeV. These resonances, with a statistical significance $Z > 5\sigma$, can be interpreted as the states $Y(4230)$, $Y(4360)$ and $\psi(4415)$.

Additionally, a proton momentum-dependent analysis strategy has been used in terms of the inclusiveness of the reconstruction and to adress the momentum discrepancies between *generic MC* and measured data.

Kurzfassung

In den letzten zwanzig Jahren wurde im Charmoniamassebereich eine Vielzahl unerwarteter Resonanzen beobachtet. Obwohl die Existenz dieser unkonventionellen Zustände bereits von der Quantenchromodynamik (QCD) vorhergesagt wurde, einer Quantenfeldtheorie, welche die starke Kraft beschreibt, fehlte bisher ein eindeutiger Beweis. Eine dieser überzähligen und unerwarteten Zustände ist das $Y(4260)$, 2005 zuerst durch BaBar beobachtet, und erweckte großes Interesse, da es Zerfälle in $c\bar{c}$ Zustände, wie das J/ψ oder das h_c ("hidden charm decay"), deutlich gegenüber Zerfällen in D Mesonen Paare ("open charm decay") bevorzugt. Dies ist sehr ungewöhnlich für Zustände mit Massen oberhalb der $D\bar{D}$ Schwelle. Weiterhin wurde der Zerfall in einen geladenen exotischen Zustand beobachtet: $Y(4260) \to Z_c(3900)^{\pm}\pi^{\mp}$. Die Ladung des $Z_c(3900)^{\pm}$ ist ein Hinweis darauf, dass es neben einem $c\bar{c}$ Paar zwei weitere Quarks enthält, und es sich somit um einen vier Quark Zustand handeln könnte. Aufgrund der noch unverstandenen Eigenschaften dieser QCD-erlaubten Zustände, werden sie als exotische oder XYZ Zustände bezeichnet, um ihre Eigenartigkeit zu unterstreichen.

Im Jahr 2017 untersuchte die Kollaboration am BESIII eine Produktionsreaktion des $Y(4260)$ mit einem Datansatz hoher zeitintegrierter Luminosität. Die dadurch deutlich erhöhte Präzision der Messung des Wirkungsquerschnittes $\sigma(e^+e^- \to J/\psi\pi^+\pi^-)$ erlaubte eine Auflösung in zwei Resonanzen, das $Y(4230)$ und das $Y(4360)$. Zudem wurde 2013 das $Z_c(3900)^{\pm}$ erstmal durch die BESIII Kollaboration nachgewiesen. Daher stellt das Experiment am BEPCII eine leistungsstarke Einrichtung dar, um exotische Zustände zu untersuchen.

In dieser Arbeit wurde eine inklusive Rekonstruktion des Hyperons Λ^0 in der Charmoniamasseregion zur Untersuchung möglicher Zerfälle von Y Zuständen durchgeführt, um weitere Erkenntnisse bezüglich ihrer Beschaffenheit zu erlangen. Der Nachweis von weiteren Zuständen oder von neuartigen Zerfallsarten kann wesentliche Hinweise geben, die starke Wechselwirkung jenseits störungstheoretischer Ansätze besser zu verstehen.

Es wurden drei Resonanzen in dem energieabhängigen Wirkungsquerschnitt beobachtet: Die erste mit einer Masse von $(4222.01 \pm 5.68)\,\mathrm{MeV}$ und einer Breite von $(154.26 \pm 28.16)\,\mathrm{MeV}$, die zweite mit einer Masse von $(4358.88 \pm 4.97)\,\mathrm{MeV}$ und einer Breite von $(49.58 \pm 13.54)\,\mathrm{MeV}$ und eine dritte mit einer Masse von $(4416.41 \pm 2.37)\,\mathrm{MeV}$ und einer Breite von $(23.88 \pm 7.18)\,\mathrm{MeV}$. Diese Resonanzen, mit einer jeweiligen statistischen Signifikanz $Z > 5\sigma$, können als die Zustände $Y(4230)$, $Y(4360)$ und $\psi(4415)$ interpretiert werden.

Bedingt durch die Inklusivität der Rekonstruktion, als auch aufgrund der Abweichung der Protonenimpulsverteilung der *generischen MC* Simulation von der gemessenen Impulsverteilung, wurde eine protonenimpulsabhängige Analysestrategie verwendet.

Contents

1. Introduction

1.1. The Standard Model of Particle Physics

The Standard Model (SM) of particle physics is the theory, which governs elementary particles, such as quarks and leptons, and had been of great success within the last five decades [1], as it has been validated by a variety of experiments.

All visible matter in the universe consists of quarks and leptons, forming protons and neutrons, and finally atoms. The quarks and leptons, six of each, are fermions of non-integer spin $S = \frac{1}{2}$ and are organised into three different generations by the SM (figure 1.1). Each generation comprises two quarks and two leptons and their corresponding antiparticles. With each generation, the mass of the elemantary particles increase, e.g. $m_u \ll m_t$.

The interaction of quarks and leptons is mediated by gauge bosons (particles with integer spin), transmitters of three fundamental forces. These three fundamental forces, electromagnetism, the weak and the strong nuclear force, have been shown to be manifestations of gauge theories, quantum field theories with an underlying local symmetry. The symmetry group of the SM is $SU(3)_C \otimes SU(2)_L \otimes U(1)$, where $SU(3)_C$ is the symmetry group the strong nuclear force, and $SU(2)_L \otimes U(1)$ is the symmetry group of the electroweak interaction.

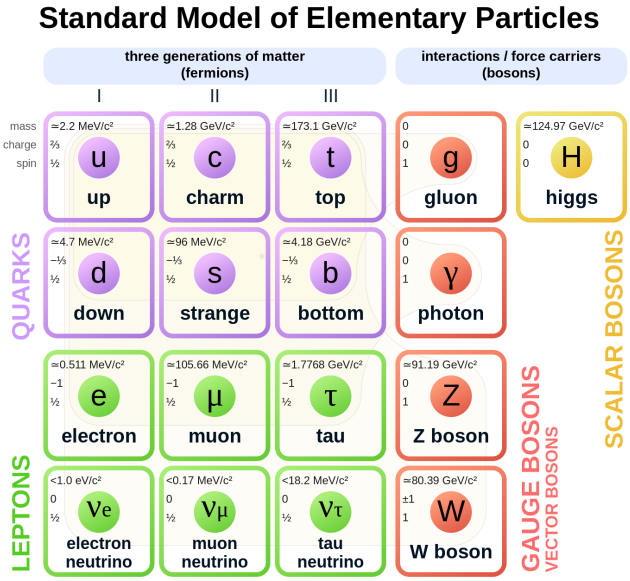

Figure 1.1: Standard Model of elementary particles [2]. The particles can be subdivided into the three currently known categories, quarks, leptons and gauge bosons. The higgs boson is the only scalar gauge boson.

The unified electroweak force describes the electromagnetic and the weak force as different aspects of the same fundamental force and its formulation has been awarded with the Nobel Prize in 1979[1]. All quarks and charged leptons are affected by the electromagentic field. Its range is infinite since its mediating particle, the photon (γ), is massless. With increasing distance of two charged particles, the potential diminishes as the probability of vacuum polarisation increases, screening the other charge and weaken the force.

[1]Steven Weinberg, Sheldon Glasgow and Abdus Salam received the Nobel Prize. Research into aspects of the SM have been awarded with 54 Nobel Prizes to date.

The weak force, acting on all elemantary particles, has a range of less than $\sim 10^{-15}$ m, since the transmitting gauge bosons (Z^0 and $W^{\pm}$) are massive. The strong force is mediated by eight gluons (g) and couples to colour-charged particles, quarks and the gluons themselves. Considering the symmetry group of $SU(N = 3)_C$, there are eight possible combinations of colour and anticolour: $3 \otimes \overline{3} = 8 \oplus 1$ leading to $N^2 - 1 = 3^2 - 1 = 8$, eight generators of gluon wave functions.

Gravity, acting on massive particles, is the only fundamental force not covered by the SM. The mass of particles (electrons, quarks, gauge bosons) is generated by their interaction with the Higgs-field. The recently discovered Higgs-boson [3], the quantum mechanic exitation of the Higgs-field, has been predicted within the SM [4], and its mass lies within one percent of the theoretical value anticipated by the model. However, the carrier of the gravitational force ("graviton") has not been discovered until now despite there are strong indications for its existence. In the subatomic region the gravitational force can be neglected.

Color charged quarks (q) and antiquarks ($\bar{q}$), carrying anticolour, can build colour-neutral states, called hadrons. Hadronic particles are subdivided into mesons, a quark-antiquark pair ($q\bar{q}$) and (anti-)baryons, triplets of (anti-)quarks. The nuclear components protons and neutrons are baryons, comprising three quarks (figure 1.2). Two down quarks (d) of the electromagnetic charge $\mathrm{q}_d = -\frac{1}{3}$ and one up quark (u) with $\mathrm{q}_u = +\frac{2}{3}$ are generating an electromagnetic and colour-neutral neutron n^0. Here, the colour charge of the respective quarks are selected exemplarily, the neutron is a superposition of the wavefunctions udd with all permitted permutations of colour charge.

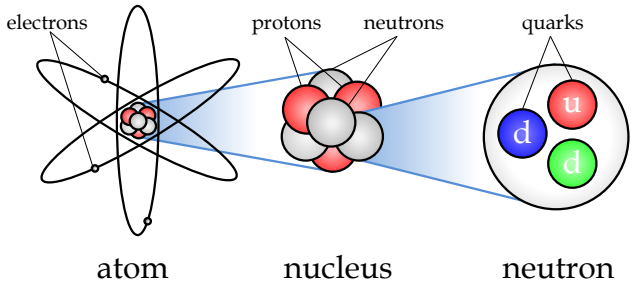

Figure 1.2: Nature of matter: atoms are composed of a shell (electrons) and a nucleus. The nucleus consists of nucleons, positively charged protons ($\mathrm{q} = +1$) and uncharged neutrons. Each nucleon consists of three quarks of the first generation. The quark constituents of a proton are uud and of a neutron udd, with $\mathrm{q}_u = +\frac{2}{3}$ and $\mathrm{q}_d = -\frac{1}{3}$.

The pion, a meson of three different combinations of up and down (anti-)quarks, can be electrically charged: $\pi^+(u\bar{d})$, $\pi^-(d\bar{u})$ and $\pi^0 = \frac{1}{2}\sqrt{u\bar{u} - d\bar{d}}$. A further classification of hadrons is based on the spin quantum numbers J^{PC} and is described in section 1.3.

1.2. The Theory of Quantum Chromodynamics (QCD)

In the mid of the last century particle physics experiments discovered a variety of new hadronic states. The properties of these new particles (hadrons) led to a new model: quarks with fractional elementary charges were introduced [5, 6], and the different hadrons are different combinations of those. Deep inelastic scattering experiments validated the quark model [7].

The discovery of the Δ^{++} baryon (top right in figure 1.3) with a spin of $\frac{3}{2}$ required a new degree of freedom, since its components, three up quarks, have the same spin alignment, which

is a contradiction to the Pauli-Principle. An additional degree of freedom, the quantum number "colour" had been introduced. This pragmatical distinction of three charge types helps to describe colour-neutral states as mesons and baryons. Either a colour and an anticolour composition (meson) or three colour states together (baryon) are colour-neutral, following the additive colour mixing of visible light.

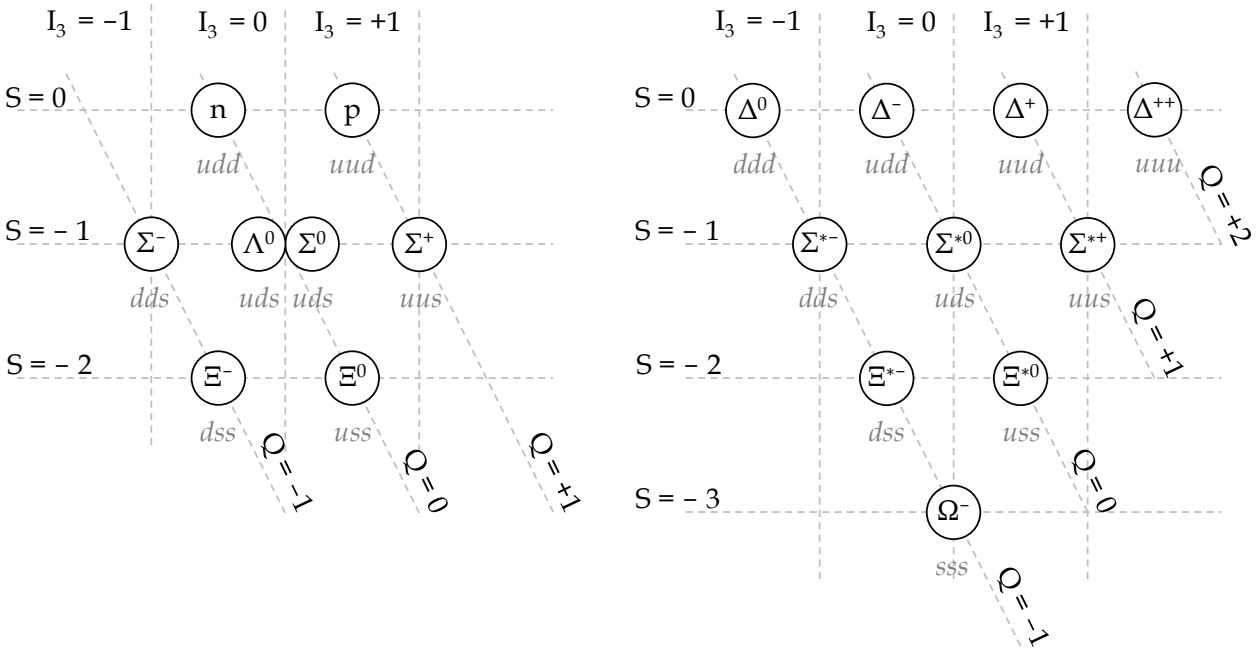

Figure 1.3: The SU(3) baryon octet with $J^P = \frac{1}{2}^+$ and decuplet with $J^P = \frac{3}{2}^+$, ordered by isospin component I_3, strangeness S and charge Q based on [8]. Shown are baryons and their quark content, e.g. $n(udd)$. Antibaryons consist of antiquarks form equivalent multiplets and are not shown.

The ground-state baryons (e.g. n, p and Λ) are classed into an octet and an decuplet regarding their spin (figure 1.3). Antibaryons are also colour-neutral, as the combination of three anticolours is also neutral.

The existence of three colour charges has been verified by the measurement of the ratio R, the hadronic cross-section over the muonic one in e^+e^- annihilation processes

$$R \equiv \frac{\sigma(e^+e^- \to \text{hadrons})}{\sigma(e^+e^- \to \mu^+\mu^-)} = 3\sum_f Q_f^2 \tag{1.1}$$

which is sensitive to the involved number of charges [9]. Q_f is the fractional charge of the quark, and the factor 3 counts the three colours of each flavour. Predictions favoring one colour charge have been disproven as experimental studies on R are significantly supporting three charges.

The dynamics of quarks and gluons is described by QCD, the quantum field theory for the strong force, similar to the well established quantum field theory for the electromagentic force. Gluons have combinations of color and anticolor, whereas (anti-)quarks carry (anti-)colour. The Lagrangian density [10] of QCD is given by

$$\mathcal{L}_{QCD} = \sum_q \bar{\psi}_{q,i}\left(i\gamma^\mu (D_\mu)_{ij} - m\delta_{ij}\right)\psi_{q,j} - \tfrac{1}{4}G^a_{\mu\nu}G^{\mu\nu}_a \tag{1.2}$$

where repeated indices are summed over. The $\psi_{q,i}$ are quark-field spinors of mass m, with quark flavour index q (u, d, c, s, t, b) and colour index i running from one to three (*red*, *green*, *blue*).

The Dirac matrices, given by γ^μ, are connecting the spinor to the vector representation. The covariant derivative $(D_\mu)_{ij}$ couples the quark field to the gluon fields and is given by

$$(D_\mu)_{ij} = \partial_\mu \delta_{ij} - ig(T_a)_{ij}\mathcal{A}^a_\mu \tag{1.3}$$

where g is the coupling constant, corresponding to the QCD coupling strength $\alpha_s = \frac{g^2}{4\pi}$. The SU(3) generators $(T_a)_{ij}$ correspond to eight 3×3 matrices, with $T_a = \lambda_a/2$, where λ_a are Gell-Mann matrix entries. The representation of the gluon fields is $\mathcal{A}^a_\mu$, with a running from one to eight. The gauge invariant gluon field strength tensor given by

$$G^a_{\mu\nu} = \partial_\mu \mathcal{A}^a_\nu - \partial_\nu \mathcal{A}^a_\mu + g f^{abc} \mathcal{A}^b_\mu \mathcal{A}^c_\nu \tag{1.4}$$

with the structure constant f_{abc}. a, b and c are running from one to eight. Since the field strength tensors contain a quadratic term in the gauge fields, self coupling of gluon fields occurs. Self-interactions between three and four gluons are possible besides the "common" interaction of gluons with quarks (figure 1.4)

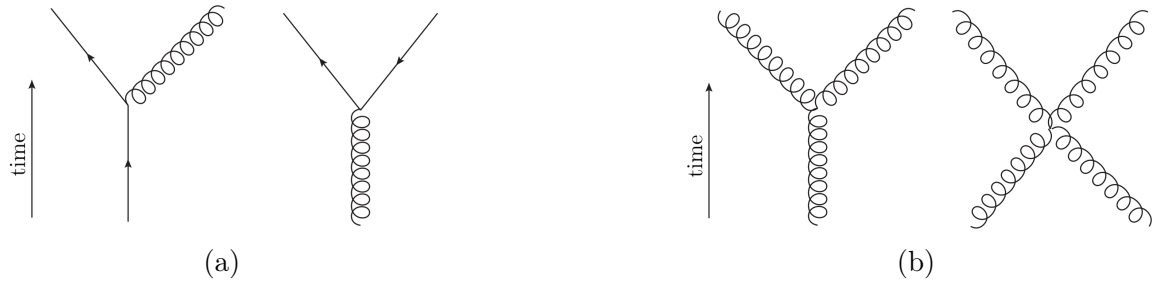

Figure 1.4: Interactions of quarks and gluons in QCD [11]. (a) Radiation of a gluon (curly line) by a quark (plain line) and gluon decay to a quark-antiquark pair. Lines of antiquarks are pointing reverse in time. (b) Self-coupling of three or four gluons.

This self-interaction of gluons is the origin of both confinement and asymptotic freedom [12]. In short: confinement occurs at large distances (r) or rather low momentum transfers (Q^2) of two quarks and means quarks cannot be observed as free particles and are confined in a colour-neutral state.

Asymptotic freedom describes the behaviour of quarks at short distances, thus high momentum transfers, where they act more or less as quasi-free. Using perturbation theory [13], the behaviour of the QCD coupling strength $\alpha_s(Q^2)$ can be derived as

$$\alpha_s(Q^2) = \frac{12\pi}{(11n_c - 2n_f) \cdot \ln(Q^2/{\Lambda_{QCD}}^2)} \qquad \text{with } Q^2 \gg {\Lambda_{QCD}}^2, \tag{1.5}$$

where n_c is the number of colours, n_f is the number of quark flavors and Λ_{QCD} is a free parameter of QCD with an estimated value of 100 to 500 MeV. Figure 1.5 shows the dependence of the coupling strength on the momentum transfer. The region of low momentum transfer (small Q^2) is not accessible for theoretical calculations using the perturbation theory. Several different alternative approaches have been developed: the "effective field theory" uses symmetries in the limit of vanishing quark masses and light mesons as degrees of freedom. The most general approach is "lattice QCD", where space-time is discretised to reduce the problem to a numerical calculation. And finally, the "non-relativistic QCD", based on the assumption that relativistic effects are small in bound states of heavy quark-antiquark pairs, such as the charmonium.

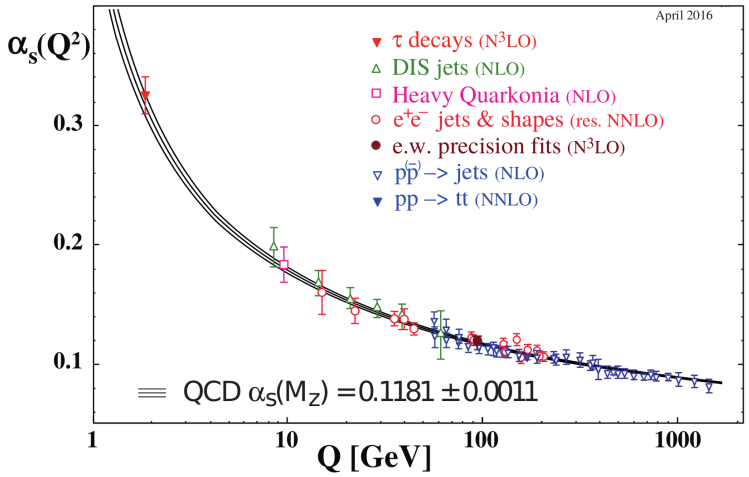

Figure 1.5: Summary of measurements of α_S as a function of the momentum transfer Q. The curves represent QCD predictions for different values of Λ [14].

1.3. Charmonium Spectroscopy

The beginning of the charmonium spectroscopy was the discovery of the J/ψ meson in 1974. Two experiments, at SLAC in an e^+e^- annihilation and at BNL in the reaction $p + \mathrm{Be} \rightarrow e^+ + e^- + X$, provided the first evidence of its existence [15, 16]. This state is electrically neutral, has a high mass ($m_{J/\psi} = 3.096\,\mathrm{GeV}/c^2$), and a long life time[1] of approximately 10^{-20} s, roughly a thousand times higher than other states in this mass region. The J/ψ was interpreted as a mesonic state of a previously unknown fourth quark species ("flavour"), the charm quark [13]. Before its observation, the existence of a fourth flavour had been predicted by the Glashow-Iliopoulos-Maiani (GIM) mechanism (until the late 1960s only the u, d, s flavours had been known) and its proof led to the acceptance of the quark model. The GIM mechanism provided an explanation for the discrepancy between the calculated and the experimentally observed decay rate of $K^0 \rightarrow \mu^+\mu^-$.

Shortly after the discovery of the J/ψ meson, two other charmed hadrons were observed: the narrow charmonium state $\psi(2S)$ at SLAC and the charmed baryon Λ_c^+ (udc) at BNL [17, 18]. The discovery of the J/ψ meson is called the "November Revolution" (of particle physics) due to its importance for the acceptance of the quark model.

Because of the high mass of the charm quark, the $c\bar{c}$ bound states can be described by non-relativistic quantum mechanics using interaction potential models, such as the Cornell potential:

$$V(r) = -\frac{4}{3} \cdot \frac{\alpha_s(r)}{r} + k \cdot r \tag{1.6}$$

with the distance r between the quark and antiquark and the string tension k, based on the very basic "string model" where two quarks are connected by an elastic string. With increasing distance, the second term increases linearly and becomes dominant, describing the confined behaviour of the strong force.

This potential is an analogy to the one of the positronium, an electron-positron bound state formed by the electroweak interaction. Therefore, $c\bar{c}$ bound states are called charmonium.

[1] Their decays are suppressed by the Okubo-Zweig-Iizuka rule: Processes mediated by the strong interaction are suppressed if the associated Feynman diagram can be divided by cutting only internal gluon lines.

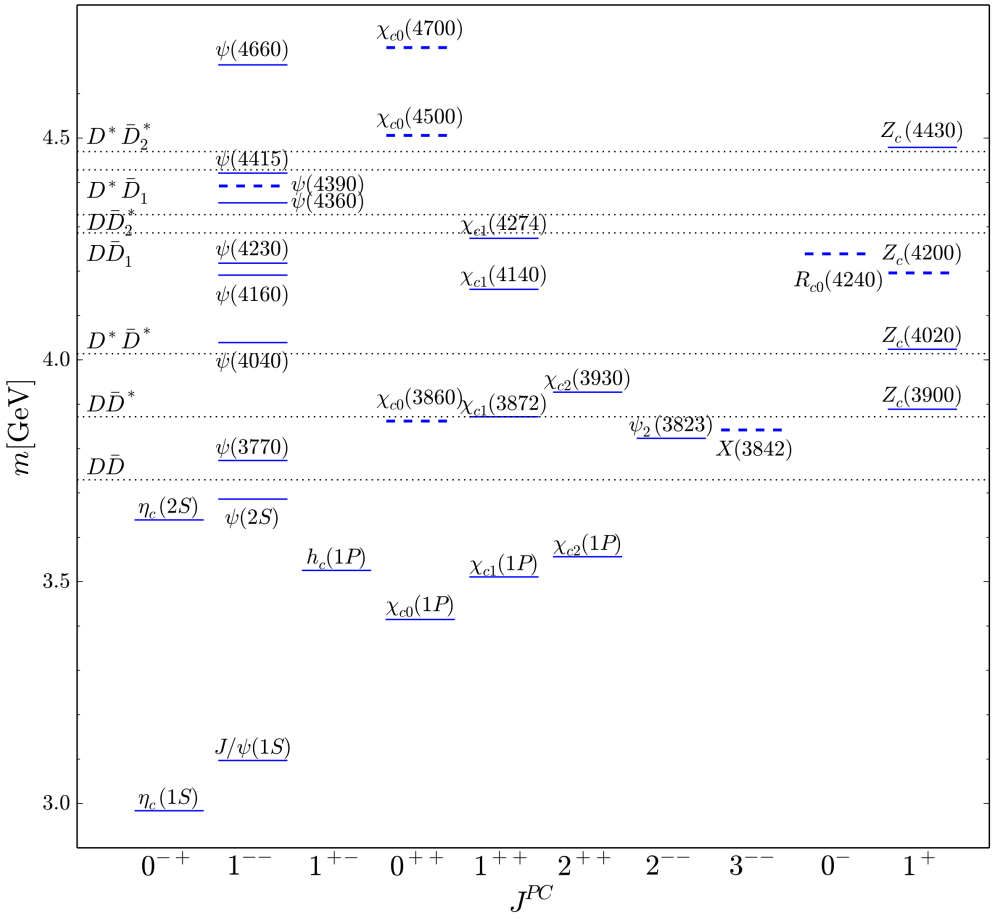

Figure 1.6: The spectrum of $c\bar{c}$ states as of July 2019 [12]. Solid lines represent experimentally established states and dashed lines are claimed but not (yet) established states. Not shown are states whose quantum numbers are yet unknown, e.g. $X(4350)$ [19]. The two columns to the right show isovectors containing a $c\bar{c}$ pair; they are necessarily exotic.

On the basis of the interaction potential and the respective masses, the charmonium states can be arranged to the charmonium spectrum (figure 1.6). States below the $D\bar{D}$ threshold (lowest dottet line) are labeled using the notation $X(nL)$ where n is the radial exitation, equal to 1, 2, 3, $\cdots$ and L is the orbital angular momentum, due to quarks orbiting each other (usually referred to as *S, P, D, F*): e.g. the $\psi(2S)$ is the first radial exitation of the $J/\psi(1S)$. The charmonia are sorted vertically according to their masses and horizontally according to their J^{PC} quantum numbers, which are conserved in strong interactions. The total angular momentum J is given by

$$J = L \oplus S \qquad \text{with} \qquad |L - S| \leq J \leq L + S \tag{1.7}$$

where S is the combined spin of the $q\bar{q}$ pair. Mathematically, the parity P is a reflection operator, and if the wave functions of the particle are eigenstates of the parity operator, then a twofold application of P should return the original state. Using the angular momentum L, parity is given as $P = (-1)^{L+1}$. The eigenvalues of P can only be ± 1.

The quantum number C is the charge conjugation, representing a transformation of the particle into its antiparticle, which reverses properties such as charge and magnetic moment. It is related to L and S by $C = (-1)^{L+S}$. A particle must be electrically neutral and its own

charged conjugated state in order to be an eigenstate of the C operator. The eigenvalues of C can only be ± 1. The allowed quantum numbers J^{PC} for mesons with regarding the quark model are listed in table 1:

spectroscopic notation	S	L	J	P	C	J^{PC}	name
1^1S_0	0	0	0	$-$	$+$	0^{-+}	pseudo scalar
1^3S_1	1	0	1	$-$	$-$	1^{--}	vector
1^1P_1	0	1	1	$+$	$-$	1^{+-}	pseudo vector
1^3P_0	1	1	0	$+$	$+$	0^{++}	scalar
1^3P_1	1	1	1	$+$	$+$	1^{++}	axial vector
1^3P_2	1	1	2	$+$	$+$	2^{++}	tensor

Table 1: Allowed J^{PC} quantum numbers for $q\bar{q}$ systems [20] with their spectroscopic notation ($n^{(2S+1)}L_J$). Exited states where $n > 1$, such as the $\psi(2S)$ with 2^3S_1, are not listed.

1.4. Exotic States

Mesons and baryons are the established bound states of QCD. As recent discoveries indicate, QCD seems not to be limited to these conventional states, so any bound state of quarks and/or gluons is allowed while fulfilling the restrictions of QCD. These states are referred to as exotic states (figure 1.7) and are briefly described here:

Hadro-quarkonium: Bound state composed of a preformed heavy quarkonium (e.g. $Q\bar{Q}$) surrounded by a cloud of light mesons ($q\bar{q}$) [21].

Tetraquark: States composed of two tightly bound pairs, a Qq and a $\bar{Q}\bar{q}$ pair.

Hybrid state: Bound states of quarks and (an) exited gluon(s), e.g. $q\bar{q}g$ [22].

Molecular state: Two mesons loosly bound together by two mechanisms: gluon exchange at short distances and pion exchange at long distances [23]

Glueball: Bound states entirely formed from gluons (e.g. gg or ggg).

Pentaquark: Bound state of a conventional baryon and a conventional meson.

Two of these configurations have been already proposed by Gell-Mann: The tetra- and the pentaquark states. Below the $D\bar{D}$ threshold, lattice QCD calculations and the observed conventional states, such as the J/ψ, are in good agreement [24]. Above this threshold, theoretical predictions and experimentally confirmed states diverge. There are predicted states, which have not been discovered (yet), such as the $h_c(2^1P_1)$ and are discovered unexpected states, such as the $Y(4260)$.

The search for exotic states is more promising in the charmonium mass region (masses higher than $2.5\,\mathrm{GeV}/c^2$), as states of heavy quarkonia are narrower than the ones of light quarks. The width of a resonance is linked to its lifetime: the longer the lifetime, the narrower the width. Additionally, the search in the lower mass region is more complicated due to the high density of conventional meson states of light quarks.

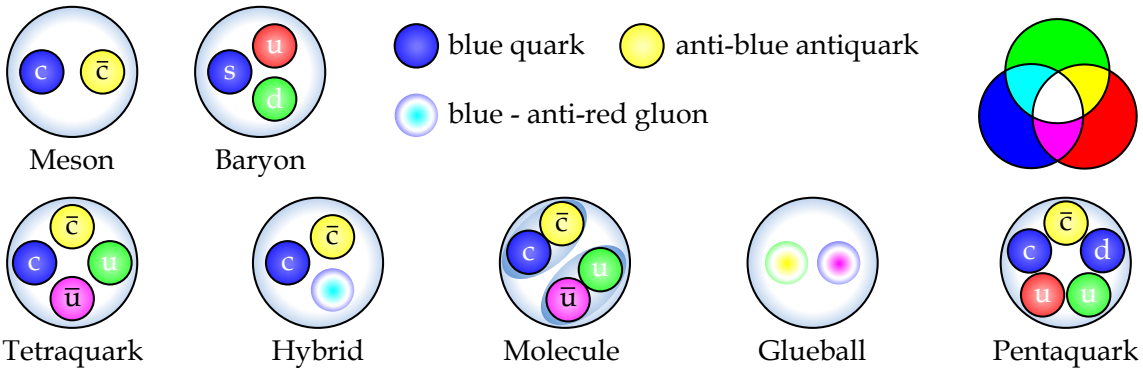

Figure 1.7: Representation of established hadrons and the QCD allowed exotic hadrons. Not shown is the hadroquarkonium listed first in the enumeration above.

Exotic states, also referred to as "XYZ" states, can be grouped according to their properties:

Exotic properties: States showing uncommon properties compared to conventional states such as being charged ($Q \neq 0$) or decays not including a D meson pair in combination with a high mass.

Spin exotics: Mesons with forbidden combinations of quantum numbers reffering to the quark model: 0^{--}, 0^{+-}, $(2n+1)^{-+}$ and $(2n+2)^{+-}$ with $n \in \mathbb{N}_0$.

Hidden exotics: States of conventional quantum numbers and no obvious exotic properties. These states could mix with conventional hadrons and their internal structure could not easily be identified.

1.5. The Charmonium-like *XYZ* States

An exotic charmonium-like state is a resonant structure comprising a $c\bar{c}$ pair but has properties that are incompatible with a conventional charmonium state. The denotations X, Y and Z are used, to distinguish between different properties of the states: X are neutral states with quantum numbers $J^{PC} \neq 1^{--}$, while Y states are vector states with quantum numbers $J^{PC} = 1^{--}$ and Z states are charged. Subsequently discovered neutral isospin partners of the charged resonances are named also Z.

The properties of the experimentally observed XYZ states give rise to the assumption that they are non-$q\bar{q}$ mesons. Since the observation of the first XYZ state, the $X(3872)$, in 2003 [25], charmonium-like states have been produced at several experiments in different reactions: Via B meson decays (BaBar, Belle and LHCb [26, 27]), via dileptonic anihilations (BESIII [28]) or by double charm production (Belle [29]).

A selection of important XYZ resonances is introduced in the following, whereas the introduction of the $Y(4260)$ is given separately due to its complex background.

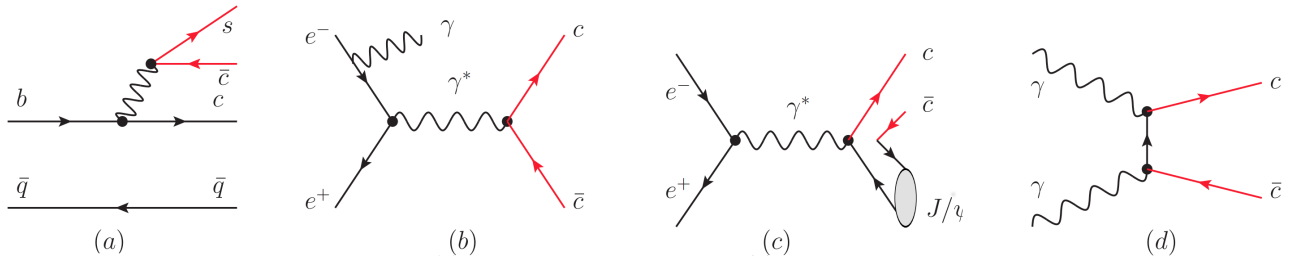

Figure 1.8: Diagramatic descriptions of four selected production mechanisms of XYZ states: (a) B meson decay ($B \to K+\ XYZ$), (b) e^+e^- annihilation ($e^+e^- \to XYZ$), (c) double charm production($e^+e^- \to J/\psi +\ XYZ$), (d) $\gamma\gamma$ fusion process ($\gamma\gamma \to XYZ$) [30].

1.5.1. Experimental Status of Selected *XYZ* States

Several candidates for charmoniumlike particles have been observed within the past two decades. The first was the $X(3872)$, discovered by the Belle collaboration [31] in exclusive $B^\pm \to K^\pm X \to K^\pm\pi^+\pi^- J/\psi$ decays and shortly after confirmed by the CDFII and the BaBar collaboration [32, 33]. Since its discovery, several other experiments confirmed its existence and determined characteristics, such as its quantum numbers $J^{PC} = 1^{++}$ [34]. Nevertheless, the nature of $X(3872)$ still remains unclear to date because of its lower mass, narrower width and puzzling decay properties, e.g. the comparable branching fractions into $J/\psi\rho$ and $J/\psi\omega$, implying an isospin symmetry violation.

The $X(3872)$ can not be assigend to the $\chi'_{c1}(2^3P_1)$ state, due to the mass difference of about $100\,\mathrm{MeV}/c^2$ between prediction and measurement [35]. In all the observed decay modes of the $X(3872)$, the final states contain charm and anti-charm quarks, hence it should comprise a $c\bar{c}$ pair at least. Several interpretations of the $X(3872)$ have been proposed, such as a tetraquark $c\bar{c}q\bar{q}$ [36], a hybrid $c\bar{c}g$ [37] and a molecule state [38], the latter due to its vicinity to the $D^0\bar{D}^{0*}$ threshold. The BESIII collaboration linked the $X(3872)$ to the $Y(4260)$ by the observation $X(4260) \to \gamma X(3872)$ [39], an indication that both states share the same quark content.

The Belle collaboration discovered the charged charmonium-like state $Z_c(4430)^\pm$ [40] in the decay $B^0 \to K^\mp Z_c(4430)^\pm \to K^\mp\pi^\pm\psi(2S)$, which is clearly an exotic state because of its charge in combination with its mass.

Six years later, in 2013, the BESIII collaboration observed another charged state and thus manifestly exotic: The $Z_c(3900)^{\pm}$ (figure 1.9, left), decaying into $J/\psi\pi^{\pm}$ in the reaction $e^+e^- \to J/\psi\pi^+\pi^-$ [41]. In the $(D\bar{D}^*)^{\mp}$ invariant mass distribution of the reaction $e^+e^- \to \pi^{\pm}(D\bar{D}^*)^{\mp}$ at $\sqrt{s} = 4.26\,\text{GeV}$, a resoncance at $3888.9\,\text{MeV}/c^2$ has been observed, which is interpreted as a $Z_c(3900)^{\pm}$ [42]. Therefore, due to its charge and its open charm decays, interpretations favor it to be either a tetraquark or a D meson molecule.

Moreover, the BESIII collaboration discovered the charged resonance $Z_c(4020)^{\pm}$ (figure 1.9, right) in the $h_c\pi^{\pm}$ subsystem of the decay $Y(4260) \to h_c\pi^+\pi^-$ [43]. One year later, the BESIII collaboration confirmed the existence of its neutral isospin partner $Z_c(4020)^0$ [44].

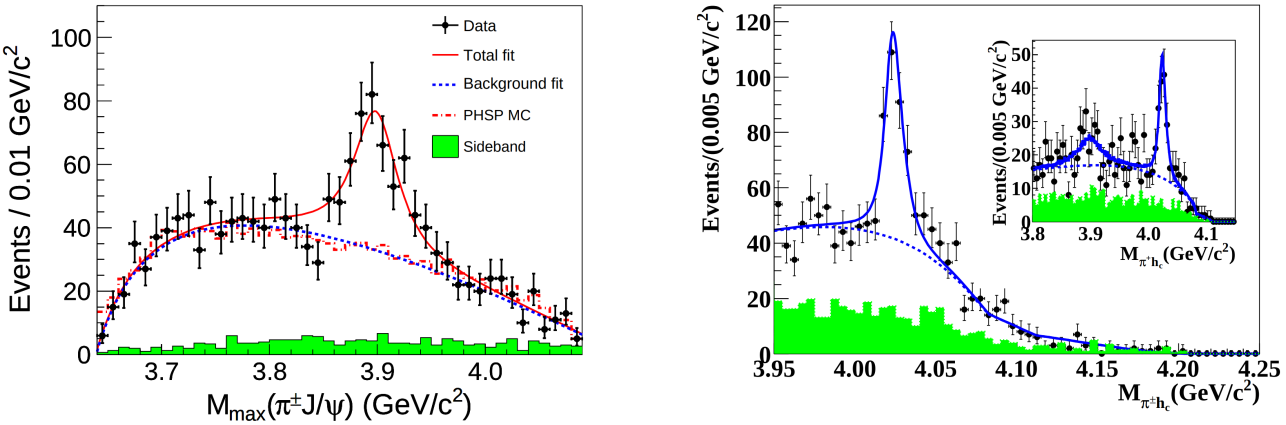

Figure 1.9: Left: First observation of the $Z_c(3900)^{\pm}$ in the inv. mass of $J/\psi\,\pi^{\pm}$ [41]. Right: First observation of the $Z_c(4020)^{\pm}$ in the inv. mass of $h_c\pi^{\pm}$ [43], both at BESIII.

The measurement of the energy dependent cross section is an excellent approach to observe new exotic states such as the $Y(4390)$ and the $Y(4500)$: in 2013, the BESIII collaboration observed the vector states $Y(4230)$[1] and $Y(4390)$ in the reaction $e^+e^- \to h_c\pi^+\pi^-$ for XYZ and R-scan data (figure 1.10, left) [45]. In 2022, the resonances of the $Y(4230)$ and the $Y(4500)$ have been reported by the BESIII collaboration in the reaction $e^+e^- \to J/\psi K^+K^-$ (right) [46].

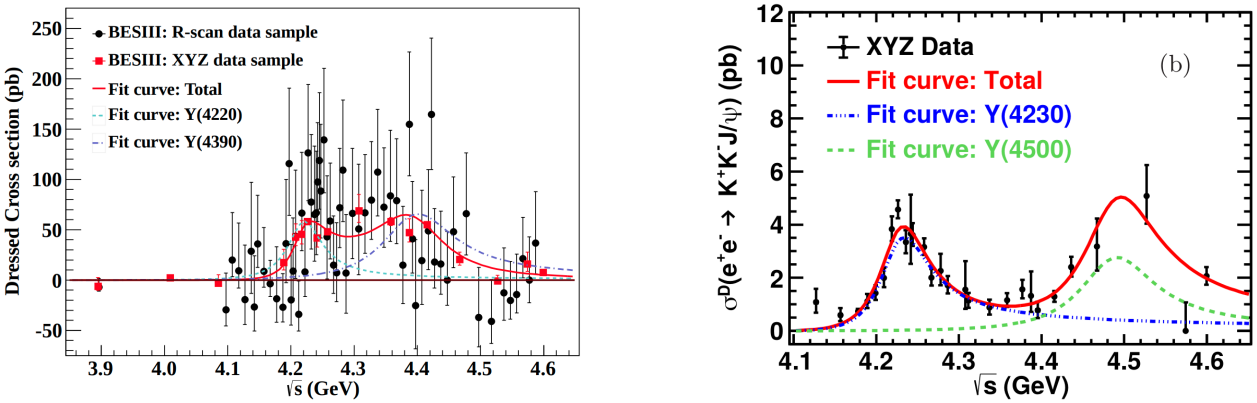

Figure 1.10: Left: Observation of the $Y(4220)$ and $Y(4390)$ [45]. Right: Observation of the $Y(4230)$ and $Y(4500)$ [46], both at BESIII. Solid curves give the total fit to the dressed cross section, the dash (dash-dot) curves show the respective contributions of each resonance.

[1] The $Y(4230)$ is the $Y(4260)$, see next section.

More than 40 years ago, the charmonium state $\psi(4415)$ had been observed in an R-scan at MARK-I (figure1.11, left) [47]. Since then, a variety of open charmed decay channels (D meson pairs) have been reported (right) [48, 49, 50].

This coupling of the $\psi(4415)$ to open charm states can be interpreted as an evidence of its nature to be a common charmonium. In addition, it can be assigned to the $\psi(4^3S_1)$ state [51]. Nevertheless, its nature is still undefined, as only sparse informations of its decays are available, its width and mass lack a precise determination, and the latter is not satisfactorily consistent with current threoretical calculations.

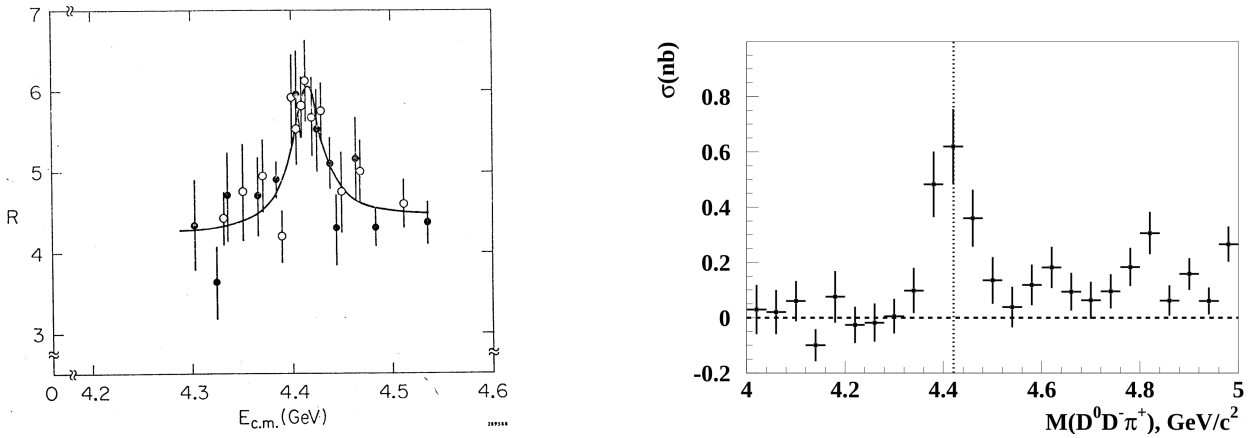

Figure 1.11: Left: The first observation in 1976 of the $\psi(4415)$ at MARK-I [47]. Right: The first observation of the $\psi(4415) \to D\bar{D}_2^*(2460) \to D^0D^-\pi^+$ decay at Belle [50].

These discoveries and still puzzling characterisics of the observed states have motivated intensive searches for further resonant structures in the charmonium region above the $D\bar{D}$ threshold. Common approaches are the measurement of the energy dependent cross section, as realised in this analysis, an R scan or a final state reconstruction.

1.5.2. The $Y(4260)$

In 2005, the $Y(4260)$ resonance was observed for the very first time in the initial state radiation reactions $e^+e^- \to \gamma_{ISR}\, J/\psi\pi^+\pi^-$ and $e^+e^- \to \gamma_{ISR}\, \psi(2S)\pi^+\pi^-$ by the BaBar collaboration [52] (figure 1.12, left) and was confirmed shortly after by the collaborations Belle and CLEO [53, 54]. Since it is produced in an ISR process, the spin-parity is $J^{PC} = 1^{--}$.

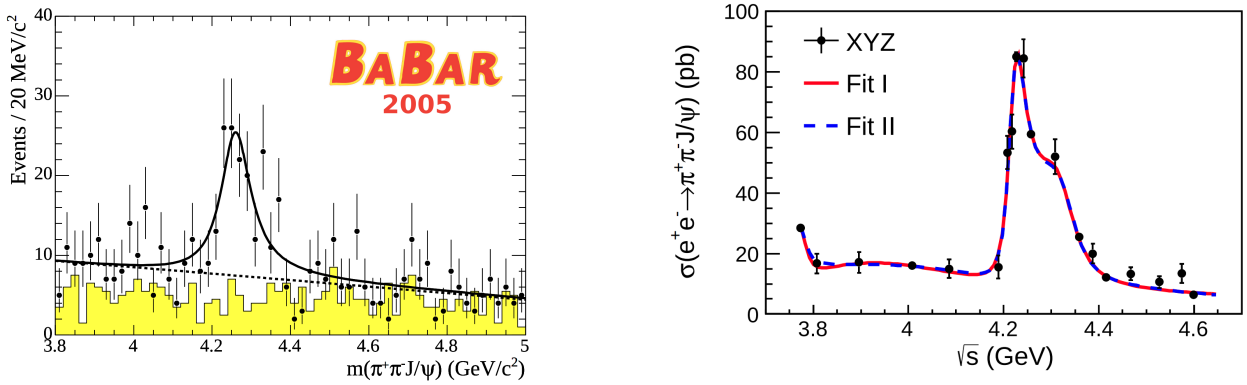

Figure 1.12: Left: The first observation of the $Y(4260)$ in the ISR process reported by BaBar [55]. Right: The energy dependent cross section of BESIII showing two resonances [56].

In 2017, the BESIII collaboration investigated the reaction $e^+e^- \to J/\psi\pi^+\pi^-$ with a high luminosity data set, dubbed XYZ data, with a time-integrated luminosity of 8.2 fb^{-1}, higher than the previous experiments (figure 1.12, right). Instead of one broad, two resonances were observed: one narrow state with a mass of $m = 4222.0 \pm 3.4\,\mathrm{MeV}/c^2$ and a width of $\Gamma = 44.1 \pm 4.7\,\mathrm{MeV}/c^2$ and a wider one with $m = 4320.0 \pm 13\,\mathrm{MeV}/c^2$ and $\Gamma = 101 \pm 27\,\mathrm{MeV}/c^2$. They have been also observed in the R-scan data set ($\mathcal{L}_{int} = 0.8\,\mathrm{fb}^{-1}$) of the BESIII collaboration with more than 80 center-of-mass energies studied (not shown). These two data samples (the XYZ and R-scan data) have been analysed via a simultaneous fit [56]. Since then, the designation of the $Y(4260)$ changed and is now referred to as $Y(4230)$ [57].

Conventionally, the $Y(4040)$, $Y(4160)$ and the $\psi(4415)$ are usually assigend to the states $\psi(3S)$, $\psi(2D)$ and $\psi(4S)$. So the $Y(4230)$ resonance of a mass near $4.26\,\mathrm{GeV}/c^2$ does not fit in this scheme. Additionally, the $Y(4230)$ has been found only once in an open charm decay channel [58] in contrast to the confirmed exited charmonia above the $D\bar{D}$ threshold.

Another puzzling aspect of the $Y(4230)$ and its decay is the dip in the R-scan performed at BESIII (figure 1.13). The R-value is the ratio of hadron to muon pair production (equation 1.1). Hence, this dip at around $4.26\,\mathrm{GeV}/c^2$ is an indication of a more comlex interplay of several resonances or no resonance at all.

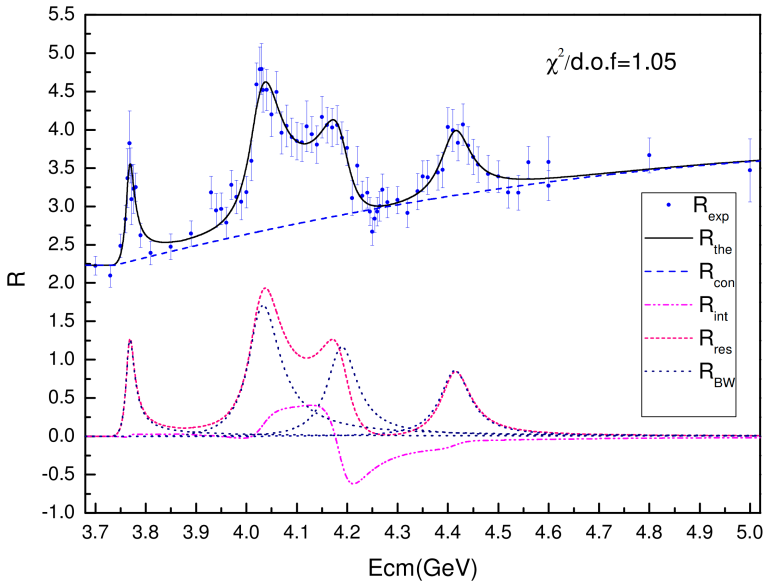

Figure 1.13: The fit to the R values for the high mass charmonia structure measured at BESIII. The best total fit is given as solid curve, dashed curves show contributions from each resonance (R_{BW}), interferences (R_{int}), the continuum background (R_{con}) and $R_{res} = R_{BW} + R_{int}$ [59].

The interplay of the $Y(4230)$ with other XYZ states as in

$$Y(4230) \to \gamma X(3872) \quad [39]$$
$$Y(4230) \to \pi^\pm Z_c(3900)^\mp \to \pi^\pm(\pi^\mp J/\psi) \quad [60]$$
$$Y(4230) \to \pi^0 D^0 \bar{D}^* \quad \text{with } Z_c(3900)^0 \text{ as resonance at } 3.9\,\mathrm{GeV}/c^2 \quad [61]$$
$$Y(4230) \to \pi^\pm Z_c(4020)^\mp \to \pi^\pm(\pi^\mp h_c) \quad [43]$$

is also exceptional as it allows the assumption that these particles share common properties and have a similar internal structure.

At present, explanations for the internal structure of the vector meson $Y(4230)$ range from a hybrid state [62, 63], a molecule [64, 65], a tetraquark [66] to even hadro-charmonium [67], as its mass and decay properties seem to be in conflict with expectations.

To some extend, the possiblity of the $Y(4230)$ being a glueball can be excluded, as glueballs are expected to decay flavour neutral, but the $Y(4230)$ decays dominately into $c\bar{c}$ final states.

The interpretation of the $Y(4230)$ being a molecule [65] of loosly bound D mesons is also almost impossible: although there are several open charm thresholds below the $Y(4230)$ (figure 1.6), only the $\bar{D}D_1(2420)$ system seems to be somehow reasonable, as its nominal threshold is only about 29 MeV above the location of the $Y(4230)$. Then again, each of the D mesons has a width of around 300 MeV/c^2, and as broad components can not produce narrow resonances, the molecule interpretation is still questionable [68].

The tetraquark interpretation of $Y(4230)$ ($\frac{1}{\sqrt{2}}(u\bar{u}+d\bar{d})c\bar{c}$) leads to an expected mass range between 4.22 to 4.37 GeV/c^2, matching its experimental mass. However, if the $Y(4230)$ would be a tetraquark, it should decay into D meson pairs, instead it shows a clear preference to hidden charm final states, such as $\pi^+\pi^- J/\psi$[52], $\pi^+\pi^-\pi^0\eta_c(1S)$ [69] and $\pi^+\pi^-\psi(2S)$ [70].

Another interpretation of the $Y(4230)$ is the "$S-D$ mixing" [71], assuming the $Y(4230)$ to be a mixture of $^3S_1$ and $^3D_1$ states. According to these non-$q\bar{q}$ interpretations, the $Y(4230)$ (and also the $Y(4360)$) is not unambiguously relateable to a spectroscopic notation like conventional charmonia (table 2), even though it is included in the spectrum of $c\bar{c}$ states (figure 1.6).

As the nature of the $Y(4230)$ is still subject of theoretical discussions even after 13 years of its discovery, it is of great interest and one of the most studied XYZ states.

name	spectroscopic notation	mass (MeV/c^2)	year of discovery	
J/ψ	1^3S_1	3096.9	1974 [15, 16]	ordinary states
$\psi(2S)$	2^3S_1	3686.1	1974 [17]	ordinary states
$\psi(3770)$	1^3D_1	3773.7	1977 [72]	in agreement with ordinary quarkonia
$\psi(4040)$	3^3S_1	4039.0	1977 [73]	in agreement with ordinary quarkonia
$Y(4230)$		4222.7	2015 [74]	exotic states
$Y(4360)$		4372	2007 [75]	exotic states
$\psi(4415)$	4^3S_1	4221	1976 [47]	in agreement with ordinary quarkonia

Table 2: Spectroscopic notation of selected charmonium and charmonium-like states.

The $Y(4360)$

The $Y(4360)$ is in a quite similar situation as the $Y(4230)$ and is also considered as a non-$q\bar{q}$ candidate. In 2007, this resonance was observed for the first time by the BaBar collaboration [76] in the initial state radiation reaction $e^+e^- \to \gamma_{ISR}\,\psi(2S)\pi^+\pi^-$ and shortly after confirmed by the Belle collaboration [77]. Just like the $Y(4230)$, its quantum numbers are $J^{PC} = 1^{--}$ and also no final conclusion about the nature has been drawn. Although the masses of $Y(4230)$ and $Y(4360)$ are considered to be incompatible with the conventional charmonia picture, [78] assigns the $Y(4230)$ and the $Y(4360)$ to the states $\psi(4S)$ and $\psi(3D)$ respectively.

1.5.3. *Y* States in Baryonic Decays

The decay of Y states (e.g. the $Y(4230)$) into baryons has not yet been observed and only upper limits have been published up to now. Even in processes including conventional baryons ,such as protons in $e^+e^- \to p\bar{p}\eta$ or $e^+e^- \to p\bar{p}\omega$ [79], no resonances above 4 GeV have been observed to date.

Predictions from QCD can be proven by two-baryonic decays of vector charmonium(-like) resonances [80]. In 2021, the BESIII collaboration published the measurement of the reaction $e^+e^- \to \Lambda\bar{\Lambda}$, showing a resonance at 3.77 GeV/c^2, that we interprete as the $\psi(3770)$ state:

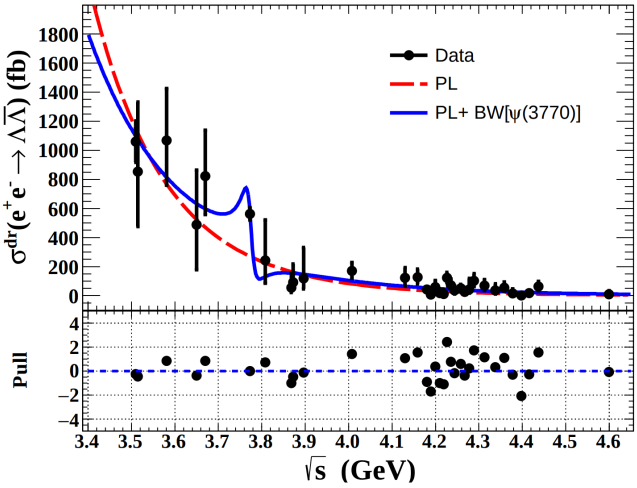

Figure 1.14: Evidence of the decay $\psi(3770) \to \Lambda\bar{\Lambda}$ at BESIII [81].

Since the $\Lambda\bar{\Lambda}$ baryons comprise strangeness ($uds/\bar{u}\bar{d}\bar{s}$), the reaction $\psi(3770) \to \Lambda\bar{\Lambda}$ represents a baryonic open strange decay. The $\psi(3770)$, $Y(4160)$ and the $Y(4230)$ have been seen in open strange decays, such as into light charged K mesons ($K^+(u\bar{s})$ and $K^-(s\bar{u})$) and occasionally with additional particles. For $Y(4360)$, neither a decay channel with a Λ baryon nor a K meson has been reported so far. In April 2022, the BESIII collaboration reported a new resonance in the reaction $e^+e^- \to K^+K^-J/\psi$ at 4.5 GeV/c^2, the $Y(4500)$, besides the confirmed $Y(4230)$ state (right figure in 1.10).

Since the exclusive reconstruction of $\Lambda\bar{\Lambda}$ in [81] is a severe limitation of baryonic channels comprising strangeness, and seems not to show any resonance in the energy regime above 4 GeV, an inclusive reconstruction of hyperon reactions seems to be promising in order to find evidence for such kind of decays, which is the subject of this thesis.

2. The BESIII Experiment

This thesis is based on experimental data taken by the BESIII operated at the BEPCII located at the Institute for High Energy Physics (IHEP) in Beijing, China. In the following sections an overview of the physics programme, the BEPCII, the BESIII and the software framework is given.

2.1. The BESIII Physics Programme

The extensive BESIII programme is ranging from light hadron physics over charmonium-, charm- and D meson physics to τ physics [82, 83]. At present, the world's largest data sets of J/ψ (more than 10 billion events), ψ' (600 million) and about 100 million events in the production energy regime of the $Y(4230)$ between 4.0 and 4.84 GeV have been recorded at IHEP. A great number of D and D_s meson decays had been acquired also. These high statistic data samples allow high precision measurements no other experiment can provide thus far [84, 85] and allow an unique search of rare new physics phenomena. The Beijing Electron-Positron Collider (BEPC), a high luminosity facility (figure 2.1) is an important contribution to the global effort in solving still unanswered questions of the SM, concerning nonperturbative effects of the QCD: glueballs, the spectrum of hadronic states and the structure of hadrons, just to name a few. Furthermore, the study of the properties of τ leptons is adressed.

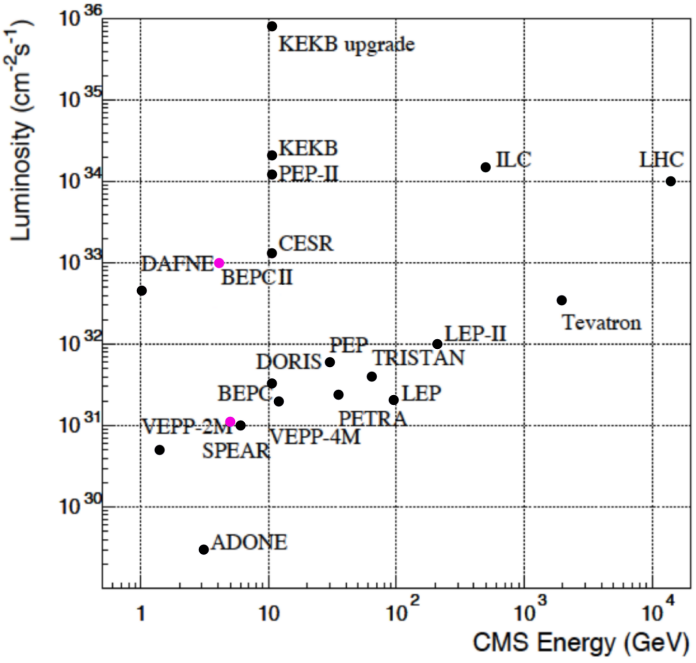

Figure 2.1: Comparison of luminosities versus center-of-mass energies of the world's colliders, status of 2013 [86] (e^+e^-, $p\bar{p}$ and pp colliders are shown). Shown in pink are the BEPC and its successor BEPCII with a designed peak luminostiy of $1 \cdot 10^{33}\,\mathrm{cm}^{-2}\,\mathrm{s}^{-2}$. BEPC (IHEP, Beijing, China), DAFNE (INFN, Frascati, Italy), PEP-II (SLAC, Stanford, California, US) and KEKB (KEK, Tsukuba, Japan) are lepton colliders.

2.1.1. Light Hadron Physics

Despite the extensive validity of the SM, confirmed by a vast number of experiments within the last five decades, some parts such as confinement are still fragmentarily conceived.

Confinement, a requirement within QCD theory, the impossibility of quark or gluon isolation, is one of the Millennium Prize Problems announced by the Clay Mathematics Institute: the quantum Yang-Mills theory exists without restriction to low energy scales [87]. At high energy or momentum transfers, or equivalently small distances, quarks behave like free (termed asymptotic freedom) and systematic calculations using the perturbation theory are feasible [88]. To fathom the behaviour of the hadronic partons within the low energy regime (large distances), well established methods like the chiral perturbation theory exist [89]. In the intermediate energy regime, at scales relevant for describing atomic nuclei, the equations of QCD remain unsolved. A non-perturbative approach which must rely either on lattice QCD or on QCD-inspired models is required. These models predict a broader spectrum of mesons, as it considers gluonic degrees of freedom (hybrids and glueballs), as introduced in section 1.4.

Therefore, the study of light hadron physics is important for achieving a better description of confinement physics. A crucial role in the search for glueballs is assigned to BESIII as the high statistics sample of the J/ψ provides a gluon rich environment via radiative decay.

2.1.2. Charmonium Physics

Charmonium spectroscopy is of great relevance for the study of the strong interaction, including the search for exotica (XYZ states), and the developement of the understanding of the strong force. The analysis of this thesis is part of charmonium physics (section 1.5.3).

A bound state of a charmed quark (c) and a charmed anti-quark ($\bar{c}$) is termed charmonium. Since the first observation of a charmonium state, the J/ψ in 1974 at SLAC [15] and BNL [16], all charmonium states below and a few above the open charm threshold ($D^0\overline{D^0}$, with a mass of approximately 3.7 GeV) have been established [90]. Both, states with masses below and above the threshold, are accessible within the BESIII energy range, so perturbative and non-perturbative QCD can be explored. Precision tests of QCD and QCD-related models are enabled by the least massive states, whereas higher mass states provide potential evidence for a huge variety of exotic configurations such as diquark-diantiquark tetraquark states, hadro-quarkonia, quark-antiquark-gluon hybrids, multi-gluon glueballs and pentaquark baryons [91]. The groundbreaking discoveries of the charged $Z_c(3900)$ [41], the first confirmation of a four quark state, and of the $Z_c(4020)$, as well as the observation of new decay modes of the $X(3872)$ were thus possible. Additionally, since there is a high statistics J/ψ sample, rare decay channels such as Cabbibo-supressed[1] decays can be studied.

2.1.3. Charm Physics

The understanding of the strong interaction can be deepend by studies of the decay of charmed hadrons (mesons ($q\overline{q}$) and baryons (qqq or anti-baryons $\overline{qqq}$)). Researches on different mechanisms like the exchange of W bosons, the weak annihilation and final state scattering are aiming at a complete description of charmed hadronic decays. BEPCII accesses energy regimes where charmed baryons can be produced near their mass threshold so the kinematics of their decay products for exclusive reconstruction are well determined.

[1] Transition of quarks within the same generation are significantly preferred, as the diagonal coefficients of the Cabibbo-Kobayashi-Maskawa (CKM) matrix are closer to 1 as the non-diagonal coefficients.

The high statistic data sample of $3.19\,\mathrm{fb}^{-1}$ at $\sqrt{s} = 4.18\,\mathrm{GeV}$ (figure 3.1) comprises a high number of $\psi(3370)$ which mainly decay into $D^0\overline{D^0}$ and D^+D^-. A good background suppression is feasible by tagging one of the D mesons resulting in high precision measurements [92]. In e^+e^- annihilations at $\sqrt{s} > 4.03\,\mathrm{GeV}$, the $D_s^+D_s^-$ threshold, strangeness comprising D_s mesons are accessible. The decay constants f_D and f_{D_s} can be determined by studying the leptonic decay of these mesons, whereas the analysis of the semi-leptonic decay allows an extraction of the CKM matrix elements V_{cs} and V_{cd} [83]. Additionally, D^0-$\overline{D^0}$ mixing, related to Charge Parity (CP) violation [93], is studied within this sector.

2.1.4. τ Physics

Another remarkable achievement of the BESIII collaboration is the world's most precise measurement of the mass of the τ lepton, three times more accurate compared to the first measurement by BES. The measurement was realised by an energy scan of the J/ψ and the $\psi(3686)$ resonance at several data points, and a scan near the τ pair production threshold, one below and four above it [83]. The τ lepton, part of the third generation of matter within the SM, is the only lepton heavy enough to decay into hadrons, giving the opportunity to study the non-perturbative regime of QCD. The study of different τ decay modes offers an estimate of the quark mixing $|V_{us}|$ (an element of the CKM matrix) and a mass determination of the strange quark (decay involves three kaons) or signs of CP violation, most promising channels are $\tau^{\mp} \to \nu_\tau K_S^0 \pi^-$ and $\tau \to \nu K^- \pi^0$ [82, 94].

2.2. The BESIII Detector at BEPCII

Since 2009 the multi bunch collider BEPCII (figure 2.2) and the spectrometer BESIII (figure 2.3), are operated at IHEP of the Chinese Academy of Sciences. They are the upgraded successors of the BEPC and BES, which were operated from 1989 to 2004.

The BEPCII, a double-ring electron-positron collider, with a design luminosity of $10^{33}\,\mathrm{cm}^{-2}\,\mathrm{s}^{-1}$ is housed in the former tunnel of the BEPC and runs in the tau-charm energy region at the centre-of-mass energy of $\sqrt{s} = (2.0 - 4.95)\,\mathrm{GeV}$ (table 3). An electron gun system provides electrons, a fraction of those are converted into positrons. Then, both species are accelerated in the LINAC of a length of 220 m and are injected in opposite directions into the ring of a circumference of 237.5 m. Opposite to the injector the BESIII detector is built around the Interaction Point (IP), where the leptonic beams collide.

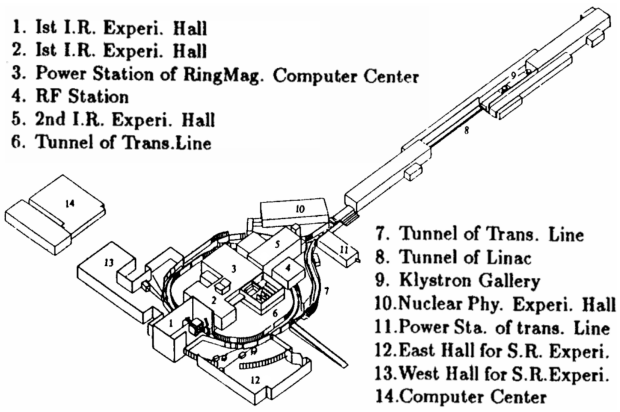

(a) Layout of the BEPC [95]

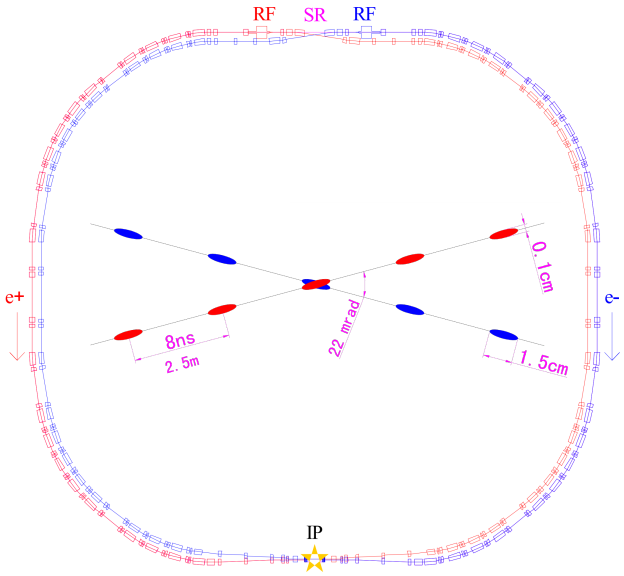

(b) Storage ring with lepton bunches [96, 97]

Figure 2.2: Left: Schematic drawing of the LINAC, the BEPCII double-ring and the experimental halls including BESIII. Right: Clockwise injected e^- are depicted in blue, e^+ in red.

LINAC length	220 m
storage ring circumference	237.53 m
designed beam energy	1.89 GeV
designed peak luminostiy at $2 \cdot 1.89\,\mathrm{GeV}$	$1 \cdot 10^{33}\,\mathrm{cm}^{-2}\,\mathrm{s}^{-2}$
center-of-mass energy $\sqrt{s}$	(2 – 4.95) GeV
beam energy	(1.0 – 2.48) GeV
designed I_{beam}	910 mA
I_{beam} at collision	650 mA e^- ring and 700 mA e^+ ring
designed I_{bunch}	9.8 mA
I_{bunch} at collision	$>$ 10 mA each ring
number of bunches	93
crossing angle at IP*	$2 \cdot 11$ mrad
Bunch spacing*	2.4 m

Table 3: Design and operation parameters of the BEPCII [97], * figure 2.2b.

From the inside out, the BESIII detector is build up from five components (figure 2.3): the Multilayer Drift Chamber (MDC), the Time-of-Flight system (TOF), the Electromagnetic Calorimeter (EMC), the Superconducting Solenoid Magnet (SSM) and the muon identifier. The interpaly of the sub-detectors, which will be introduced hereinafter, allows the identification of neutral and charged particles and their properties. The barrel of the spectrometer covers a polar angle of $|\cos(\theta)| < 0.83$ and $0.85 < |\cos(\theta)| < 0.95$ for the endcaps. The solid angle coverage is $\Delta\Omega/4\pi = 0.93$.

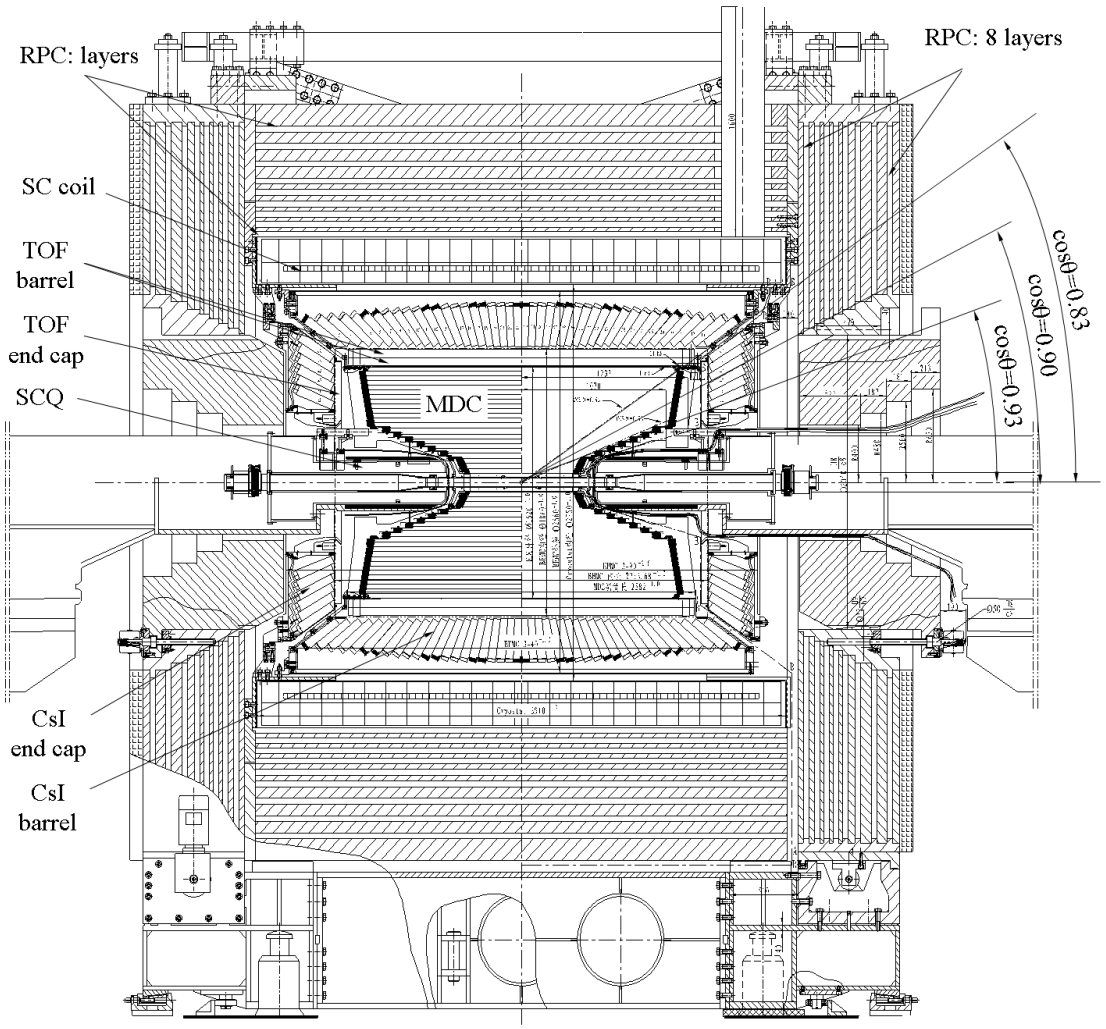

Figure 2.3: Schematic drawing of the BESIII detector and its polar angle coverage [28]. Depicted are the various components of the different sub-detectors. The RPCs are part of the muon identifier, the Superconducting Quadrupoles (SCQ) of the SSM and CsI crystals of the EMC.

2.2.1. Multilayer Drift Chamber – MDC

The MDC is the innermost sub-detector and enables a momentum (p) and specific energy loss ($\mathrm{d}E/\mathrm{d}x$) measurement of charged particles. By means of these characteristics, a reconstruction of charged tracks in 3D space and an identification of charged particles is feasible.

The MDC is subdivided into two chambers which are sharing the same gas volume, but the inner comprises of eight, the outer of 35 layers of drift cells. As the final focusing quadrupoles are located as close as possible to the IP, the end plates of the inner chamber are designed in a

conical stepped shape. The detector volume is filled with a mixture of He - C_3H_8 gas at a ratio of 60:40 in order to impede multiple scattering while keeping a good $\mathrm{d}E/\mathrm{d}x$ resolution.

Each layer can be subdivided into a smaller unit: a drift cell. A drift cell is build up from a gold plated tungsten sense wire surrounded by eight gold plated alluminum field wires.

Charged particles ionise the gas on their way through the detector volume. The resulting electrons and ions are accelerated by the electric field and an avalanche is created which is read out by the wires. A particle momentum resolution of 0.5% and 6% for $\mathrm{d}E/\mathrm{d}x$ allow a 3σ π/K separation up to 770 MeV/c in the 1 T solenoid field at 1 GeV/c. Furthermore the MDC produces signals for the level 1 triggers for event selection.

2.2.2. Time-of-Flight System – TOF

The TOF system is a further instrument for particle identification determining the mass-to-charge ratio via measuring the time-of-flight. Two layers of 88 aluminum wrapped plastic scintillator bars are mounted on the outer surface shell of the MDC, building up the barrel TOF, covering a polar angle of $|cos(\theta)| < 0.83$. Each end cap of the MDC is covered with a single layer of 48 fanshaped bars, the end cap TOF, with a coverage of $0.85 < |cos(\theta)| < 0.95$ On both end faces of every scintillator bar a fine mesh Photomultiplyer (PMT) is directly attached. This direct attachment of PMTs leads to a time resolution of $\approx$ 100 ps and hence allows a 3σ π/K separation up to momenta of 900 MeV/c at 90°.

Ionising particles excite the fluor, the fluorescent emitter (molecule), while passing the bar of a thickness of 5 cm. The emittied photon of the fluor is directed to the end faces of the bar by reflection on the surface and is read out by the PMTs.

2.2.3. Electromagnetic Calorimeter – EMC

The main purpose of the EMC is the measurement of the photon energy above 20 MeV and their hit position. The barrel and the two end caps consist of 6240 CsI(Tl) crystals ($4800 + 2{\times}720$) with a shape of a truncated pyramid ($5.2 \times 5.2\,\mathrm{cm}^2$ front face, $6.4 \times 6.4\,\mathrm{cm}^2$ rear face). The 28 cm long crystals are oriented along the polar angle (θ), aiming with the front face towards the IP. At the rear of each crystal a preamplifier is mounted onto an aluminum connecting plate. The light collection property of the crystals is ensured by an aluminum backed white wrapping. In sum the EMC presents a weight of approximately 24 tons.

The calorimeter is located outside of the TOF and has the same polar angular coverage. The position resolution of the EMC for electromagnetic showers is $0.6\,\mathrm{cm}/\sqrt{E/\mathrm{GeV}}$ and the energy resolution is $\sigma_e/E = 2.5\%$ at 1 GeV. In addition, the PID system uses the shapes of the showers produced by the particles within the EMC to distinguish between different species.

2.2.4. Superconducting Solenoid Magnet – SSM

The SSM enables along with the MDC a measurement of particle momenta as the trajectories of charged particles are bended in the presence of a magnetic field. The octagonal barrel yoke encloses the EMC and generates together with the two forward yokes a uniform axial field of 1 Tesla. Moreover the SSM serves as hadron absorber for hadron/muon separation. Hence the yokes of steel are segmented into layers, housing the Resistive Plate Chambers (RPC) of the muon identifier, discussed in the following.

With a length of 3.52 m and a radius of 1.482 m the solenoid has a weight of 15 tons.

2.2.5. Muon Identifier

The main purpose of the muon identifier is to separate muons from pions, hadrons and background as many final states of interest of the BESIII programme involve muons. The muon identifier is based on RPCs, precise gaseous time-of-flight detectors. In the interplay of the muon identifier with the MDC for track reconstruction and the EMC for energy measurement a low cut-off momentum identification is feasable. Muons create specific hit patterns while crossing the layers of the RPCs interspersed in the steel plates of the SSM. As muons are minimum ionising particles in the energy regime of the BESIII programme, their loss of energy is smaller than 0.2 MeV in the EMC.

The barrel sector has nine alternating layers of RPCs with steel plates, starting with a RPC from the inside out. In the end caps there are eight layers of RPCs, starting with a steel plate. All 978 RPCs are build up by bakelite plates backed with a resistive paint as electrodes and are filled with a gas mixture of $Ar/C_2F_4H_2/C_4H_{10}$ (50:42:8). The polar angle coverage of the muon identifier is the same as of the TOF and EMC, the RPCs cover an area up to 1272 m^2.

2.2.6. Trigger System

The trigger system selects events of interest in a high background rate environment with a maximum throughput of 4 kHz at 3.097 GeV. Besides the beam related background and Bhabha scattering events, cosmic ray interactions have to be excluded. The trigger system reduces background to a level smaller than the expected 2 kHz event rate at the J/ψ peak. As the multi-beam bunches are spaced in 8 ns gaps, a high data rate processing in real-time is crucial.

There are two trigger levels: the first (L1) is a hardware trigger and is activated by the TOF, the MDC and the EMC. Once an incoming signal is L1 accepted (6.4 μs after the collision) the event building takes place. The next level (L3) is a software trigger using an online computer farm and is ruling final storage of data.

2.3. Software Framework

This section gives a brief overview of all used software packages to analyse the data taken at BESIII and also the Monte Carlo (MC) simulations forming the basis of this thesis.

2.3.1. CERN ROOT

The ROOT software framework, based on the object-oriented programming language C++, is developed at CERN since 1994 [98] and provides a variety of classes and libraries especially designed for high energy physics experiments facing extensive amounts of data. As the framework libraries are available for most common operating systems like Windows, Linux and Mac OS it is widely used in research facilities worldwide and finds more and more scopes of other applications, e.g. data-minig. ROOT is the successor of CERN's PAW (Physics Analysis Workstation [99]), based on FORTRAN (**For**mula **Tran**slating System) [100]).

All plots and histograms of the analysis of this thesis are generated using ROOT version 6.20.

2.3.2. Geant4

Like ROOT, the software platform **Ge**ometry **an**d **t**racking (Geant4) is developed at CERN since 1998 [101], is also based on C++ and is a toolkit for "the simulation of the passage of particles through matter" [102] using MC methods. As it contains useful aspects as geometry,

tracking, detector response and run management, it is time saving for many physics simulations (low level details are already covered). Therefore it is also distributed worldwide and is applied in a variety of research fields such as high energy physics, astrophysics and space science.

For an appropriate simulation of the interaction of particles produced in the e^+e^- annihilation with the detector material as well as their change of momentum and energy due to scattering processes, Geant4 binds to GDML[1] [103], which provides the detector geometry information.

The DST files provided by the BESIII community, upon those this thesis relies, contain event reconstructions of *generic background MC simulations* using BOOST, the BESIII Object Oriented Simulation Tool, which is based on Geant4. The initial resonance produced in the e^+e^- annihilation is simulated using the KKMC event generator [104] and further decays are handled by `BesEvtGen` (figure 2.4) a particle decay simulation package developed from `EvtGen` [105].

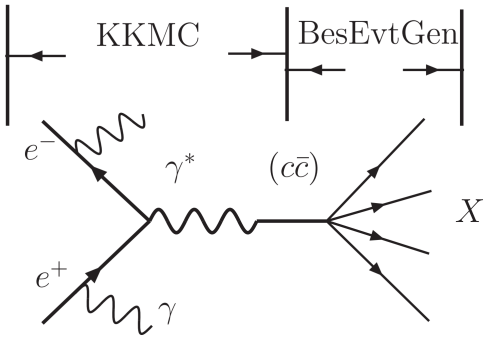

Figure 2.4: Illustration of the BESIII generator framework [82].

2.3.3. BESIII Offline Software System – BOSS

The BOSS framework, developed within the BESIII collaboration is based on C++ and SLC4[2] and is used to reconstruct, calibrate and analyse data collected with the BESIII detector. All detector sub-systems and their respective calibrations, reconstruction algorithms and tools like particle identification are covered by more than 100 libraries, written in C++ and partially based on Gaudi [106]. The Configuration Management Tool (CMT) is applied to compile these libraries. Gaudi's Event Data Service act as data manager within the framework and raw event data from the Transient Data Store (TDS) can be accessed via Event Data Service by reconstruction algorithms. While the reconstruction packages proceed data into DST files, a Kalman-filter performs the fitting for charged tracks, precursors of particle candidates. At the same time, clustering algorithms make the energy of the track (or neutral particle) available (energy deposits in the EMC, section 2.2.3), and informations of other systems are gathered, too. Finally, if they meet specific conditions, all information of all detector sub-systems are subsequently merged into a particle candidate.

Each analysis of DST files, e.g. efficiency studies using simulations or reconstruction of measured data, requires an implementation of an individual software package, which then is executed using the batch farm. The BOSS versions used in this thesis are 7.0.4 for data samples from the years 2013, 2016 and 2017 and 7.0.5 for data of the year 2019 (table 4).

[1] Geometry Description Markup Language
[2] Scientific Linux CERN

3. Analysis Overview

In the following sections, the sets of measured data and MC simulations, the applied selections and cuts, the acceptance and reconstruction efficiency determination and finally the approach of the cross-section measurement will be described.

3.1. The BESIII Dataset and Generic Monte Carlo Simulations

In this analysis 21 data samples collected with the BESIII detector operating at the BEPCII collider are studied at center-of-mass energies between 4130 and 4440 MeV (figure 3.1 and table 4) and are in the following referenced by their corresponding energies: e.g. D4440.

The samples with a total time-integrated luminosity ($\mathcal{L}_{int}$) of $14.5\,\mathrm{fb}^{-1}$ are referred to as "XYZ data" as they have been recorded to investigate the XYZ states (section 1.5). Nearly all data samples cover a time-integrated luminostiy of at least $500\,\mathrm{pb}^{-1}$ each, the only exception being the data set at D4280 with a little less than $180\,\mathrm{pb}^{-1}$. The largest data set is D4180, with $\mathcal{L}_{int} = 3189.0\,\mathrm{pb}^{-1}$, as its purpose has a second physics motivation: the analysis of D_s decays.

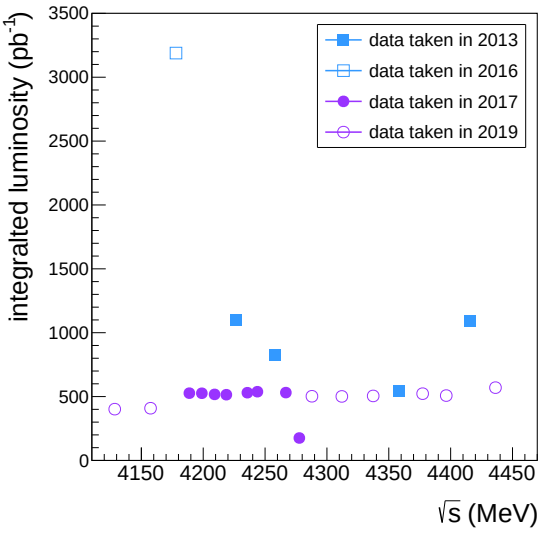

Figure 3.1: The time-integrated luminosity versus nominal center-of-mass energy of the 21 data samples used in this analysis accumulated at BESIII.

Generic background MC simulations (*generic MC*) are used to investigate the acceptance (A), the reconstruction efficiency (ε) of the detector, and to improve selection criteria. In general, the simulation consists of three parts: first KKMC generates the initial resonance [104], then `BesEvtGen` handles the further decays (based on calculations of amplitude probabilities and spin-density matrices) [105] and subsequently the interaction of particles with the detector material is simulated (using the Geant4 framework) [102]. Even though the *generic MC* is composed of all currently known reactions of e^+e^- scattering, the shape of the momentum distribution of measured data and MC differs (figure 3.2), but the observed phase space is fully covered by these simulations. The latter is the reason why *generic MC* is used for the calculation of ε and not a dedicated signal MC simulation. To adress the difference of the shape of the momentum distribution the efficiency correction and analysis is performed momentum dependent. The analysis uses reconstructed (anti-)protons, satisfying several criteria (table 5),

so they are identified as one of the two decay particles of the Λ^0 ($\bar{\Lambda}^0$). Due to lacking *generic MC* at some of the energies, efficiencies for those are interpolated (section 3.5.1). Data samples and *generic MC* simulations (table 4) of the years 2013, 2016 and 2017 are analysed within the BOSS framework version 7.0.4, data of 2019 with version 7.0.5 (section 2.3.3).

ID	$\sqrt{s}$ (MeV)	$\mathcal{L}$ (pb^{-1})	year	*gen.MC*
D4130	4128.48	401.5 ± 0.10 ± 1.00	2019	□
D4160	4157.44	408.7 ± 0.10 ± 1.00	2019	□
D4180	4178.00	3189.0 ± 0.20 ± 31.90	2016	□
D4190	4188.80	526.7 ± 0.10 ± 2.20	2017	■
D4200	4198.90	526.0 ± 0.10 ± 2.50	2017	■
D4210	4209.20	517.1 ± 0.10 ± 1.80	2017	■
D4220	4218.70	514.6 ± 0.10 ± 1.80	2017	■
D4230	4226.26	1100.9 ± 0.13 ± 7.29	2013	■
D4237	4235.70	530.3 ± 0.10 ± 2.40	2017	■
D4246	4243.80	538.1 ± 0.10 ± 2.70	2017	■
D4260	4257.97	828.4 ± 0.10 ± 5.50	2013	■
D4270	4266.80	531.1 ± 0.10 ± 3.10	2017	■
D4280	4277.70	175.7 ± 0.10 ± 1.00	2017	■
D4290	4287.88	502.4 ± 0.10 ± 1.00	2019	□
D4315	4312.05	501.2 ± 0.10 ± 1.00	2019	□
D4340	4337.39	505.0 ± 0.10 ± 1.00	2019	□
D4360	4358.26	543.9 ± 0.10 ± 3.60	2013	■
D4380	4377.37	522.7 ± 0.10 ± 1.00	2019	□
D4400	4396.45	507.8 ± 0.10 ± 1.00	2019	□
D4420	4415.58	1090.7 ± 0.13 ± 7.21	2013	■
D4440	4436.24	569.9 ± 0.10 ± 1.00	2019	□

Table 4: The luminosities of the 21 *XYZ* data samples used in this analysis and enumeration of existing (full symbols) or nonexistent (open symbols) *generic MC*.

3.2. Event Selection

The event selection reduces a large amount of data to a smaller sample with a higher rate of events of interest and consists of some of the standard BESIII selection criteria.

3.2.1. Geometrical, PID and Momentum Selection Criteria

At first, charged particle detector signals (tracks) are selected by the triggering system in conjunction with the information of the MDC. These criteria reject background tracks from sources such as cosmic radiation. Additionally the distance of the track to the IP has to fulfill geometrical conditions: $|R_{xy}| < 10\,\text{cm}$ and $|R_z| < 100\,\text{cm}$ with respect to the beam direction, tracks outside this cylindrical volume are rejected. Tracks with trajectories (flight directions) too close to the beam axis will be excluded: the cosine of the polar angle θ has to satisfy $|\cos(\theta)| < 0.9$. All tracks fulfilling these conditions are referred to as "good tracks".

Good tracks become particle candidates, if the calculated Particle Identification (PID) probability, based on the respective particle hypothesis, is larger than the others (table 5).

Additionally, a momentum cut of $p \in [0.28; 1.40]\,\text{GeV}$ is applied on (anti-)protons to improve the uncertainty of the efficiency corrected yield and will be discussed in section 3.6.

type of selection	specification
track selection	$\lvert R_{xy}\rvert < 10\,\text{cm}$ and $\lvert R_z\rvert < 100\,\text{cm}$ $\lvert\cos(\theta)\rvert < 0.9$
PID selection	for p: PID(p)>PID(x) (x $\in \{K, \text{e}, \mu, \pi\}$) for π: PID(π)>PID(x) (x $\in \{K, \text{e}, \mu, p\}$)
momentum selection	$p_p \in [0.28; 1.40]\,\text{GeV}/c$

Table 5: Summary of the applied selection criteria.

3.2.2. The Difference in Proton Momentum Spectra between Data and MC

The efficiencies and yields in this analysis are determined depending on the proton momentum in order to properly take into account the difference in the phase space between data and *generic MC* (figure 3.2). The approach of the efficiency (ε) calculation and yield (N) determination is explained in detail in section 3.5.

The difference[1] could be explained as follows: reconstructing a Λ^0 of the decay $e^+e^- \to \Lambda^0 X$ with unknown recoil system X implies two unknown quantities, the multiplicity n and the species s of the recoiling particles in the unknown system X. Depending on the species, and hence energy balance, a different fraction of the beam energy is converted into momentum. At present, *generic MC* represents the best estimate of n and s in reactions of e^+e^- scattering. To account for the mismatch of the momentum distributions, the efficiency and the yield are determined in narrower momentum ranges (hereinafter called *bins*).

Figure 3.2 shows the sideband-subtracted[2] momentum distributions for protons of Λ^0 candidates with applied angular cut for the exemplarily chosen data sample D4230.

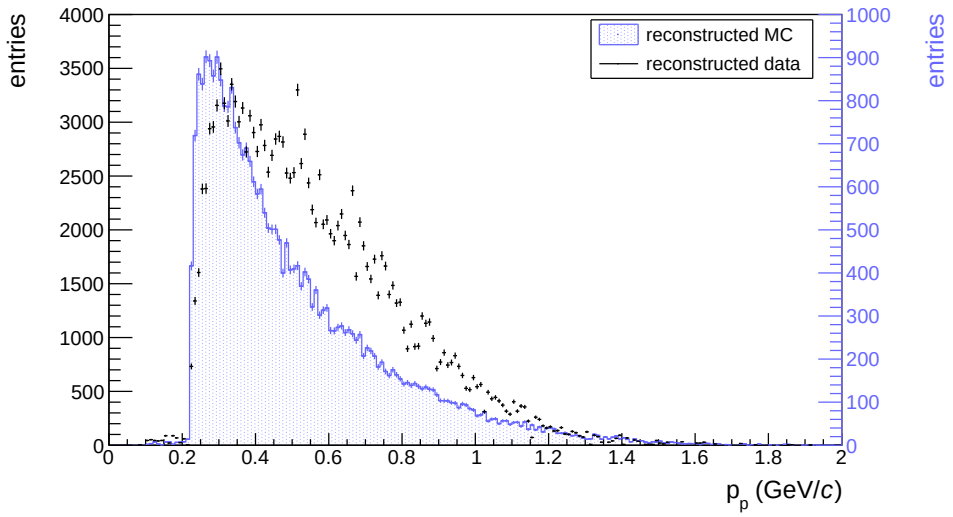

Figure 3.2: Sideband-subtracted[2] p_p spectra (Λ^0 reconstruction) of *generic MC* (blue, right scale) and of measured data (black, left scale) of D4230 with applied selections (table 5).

[1] The probability of the Kolmogotov Test is 0.00, a statistical test of compatibility in shape.
[2] The approach of the sideband subtraction is explained on page 30 and following.

3.3. The Vertex Fit Procedure

A vertex fit is a mathematical procedure to improve the angular resolution of the reconstructed particles of a decay in a magnetic field, and therefore the mass of the composite particle of their origin, and is based on the Lagrange multiplier method [107]. In general, the best estimate of the 4-momentum of a particle relies on the information of its reconstructed track. This estimate can be improved by applying so-called constraints, reflecting certain hypothesis about the reaction. Charged tracks assigned to the same decay are expected to originate from a common point in space-time. This common point of origin is used to recalculate the tracks of the charged particles within their errors. Finally, the enhancement of the tracks results in a minimal distance of both tracks to an updated common point in space.

A more detailed description of the fitting package used in BOSS can be found in [108].

Let α represent a track defined by seven parameters, a 4-momentum and a point of its evaluation: $\alpha = (p_x, p_y, p_z, E, x, y, z)$. A set of n tracks can be represented by a column vector $\boldsymbol{\alpha}$

$$\boldsymbol{\alpha} = \begin{pmatrix} \alpha_1 \\ \alpha_2 \\ \vdots \\ \alpha_n \end{pmatrix} \tag{3.1}$$

with the initial and unconstrained values $\boldsymbol{\alpha}_0$, received from a track fit for instance.

The r constraints on $\boldsymbol{\alpha}$ can be described by the function $\mathbf{H}$

$$\mathbf{H}(\boldsymbol{\alpha}) = 0, \text{ where } \mathbf{H} \equiv (H_1, H_2, \ldots, H_r) \tag{3.2}$$

The expansion of 3.2 into a Taylor series (of first two terms) around a convenient point $\boldsymbol{\alpha}_A$ results in the linearised equations

$$0 = \mathbf{H}(\boldsymbol{\alpha}_A) + \partial_{\boldsymbol{\alpha}}\mathbf{H}(\boldsymbol{\alpha}_A)(\boldsymbol{\alpha} - \boldsymbol{\alpha}_A) \tag{3.3}$$

$$\equiv \mathbf{d} + \mathbf{D}\delta\boldsymbol{\alpha} \tag{3.4}$$

with $\delta\boldsymbol{\alpha} = (\boldsymbol{\alpha} - \boldsymbol{\alpha}_A)$, $D_{ij} = \partial_{\alpha_j} H_i$ and $d_i = H_i(\boldsymbol{\alpha}_A)$; $i \in [1; r], j \in [1; n]$. The r constraints are included using the the method of Lagrange multipliers where χ^2 is a sum of two terms:

$$\chi^2 = (\boldsymbol{\alpha} - \boldsymbol{\alpha}_0)^T \mathbf{V}_{\boldsymbol{\alpha}_0}^{-1} (\boldsymbol{\alpha} - \boldsymbol{\alpha}_0) \; + \; 2\boldsymbol{\lambda}^T(\mathbf{d} + \mathbf{D}\delta\boldsymbol{\alpha}) \tag{3.5}$$

with $\boldsymbol{\lambda}$, a vector of r unknowns, the Lagrange multipliers. As the n tracks pass through a common point $\boldsymbol{x} = (x, y, z)$, the overall χ^2 condition needs to be extended to

$$\chi^2 = (\boldsymbol{\alpha} - \boldsymbol{\alpha}_0)^T \mathbf{V}_{\boldsymbol{\alpha}_0}^{-1} (\boldsymbol{\alpha} - \boldsymbol{\alpha}_0) \; + \; (\boldsymbol{x} - \boldsymbol{x}_0)^T \mathbf{V}_{\boldsymbol{x}_0}^{-1} (\boldsymbol{x} - \boldsymbol{x}_0) \; + \; 2\boldsymbol{\lambda}^T(\mathbf{d} + \mathbf{E}\delta\boldsymbol{x} + \mathbf{D}\delta\boldsymbol{\alpha}) \tag{3.6}$$

with $\delta\boldsymbol{x} = (\boldsymbol{x} - \boldsymbol{x}_A)$, the deviation of the parameters from their expansion points and the representation of the initial vertex position and its covariance matrix $\boldsymbol{x}_0$ and $\boldsymbol{V}_{\boldsymbol{x}_0}$. Conditions such as the constant solenoidal field strength or the fact that the constraints do not mix tracks (they are initially uncorrelated) simplifies equation 3.6 to

$$\chi^2 = \boldsymbol{\lambda}^T(\mathbf{d} + \mathbf{E}\delta\boldsymbol{x} + \mathbf{D}\delta\boldsymbol{\alpha}) \tag{3.7}$$

containing the covariance matrices $\boldsymbol{V}_{\boldsymbol{x}}$ and $\boldsymbol{V}_{\boldsymbol{\alpha}}$. A detailed derivation can be found in [109].

The physical meaning of the three terms can be approximately described as follows: the first term correlates the tracks with one another. The second term contains the vertex error matrix $\boldsymbol{V_x}$, which is the weighted average of its initial covariance matrix and the errors obtained from the tracks. The last one comprises the track error matrix $\boldsymbol{V_\alpha}$ which is increased by small deviations of the vertex position and is decreased by the constraints applied per track. No other constraints were applied in this analysis.

The improvement of the angular resolution by the vertex fit of the daughter particles (protons and charged pions) and hence of the invariant mass of the reconstructed particle is depicted in figure 3.3. The signal peaks in the invariant mass histograms are narrower for both species with applied vertex fit (blue for Λ^0, pink for $\bar{\Lambda}^0$) as the ones without applied fit.

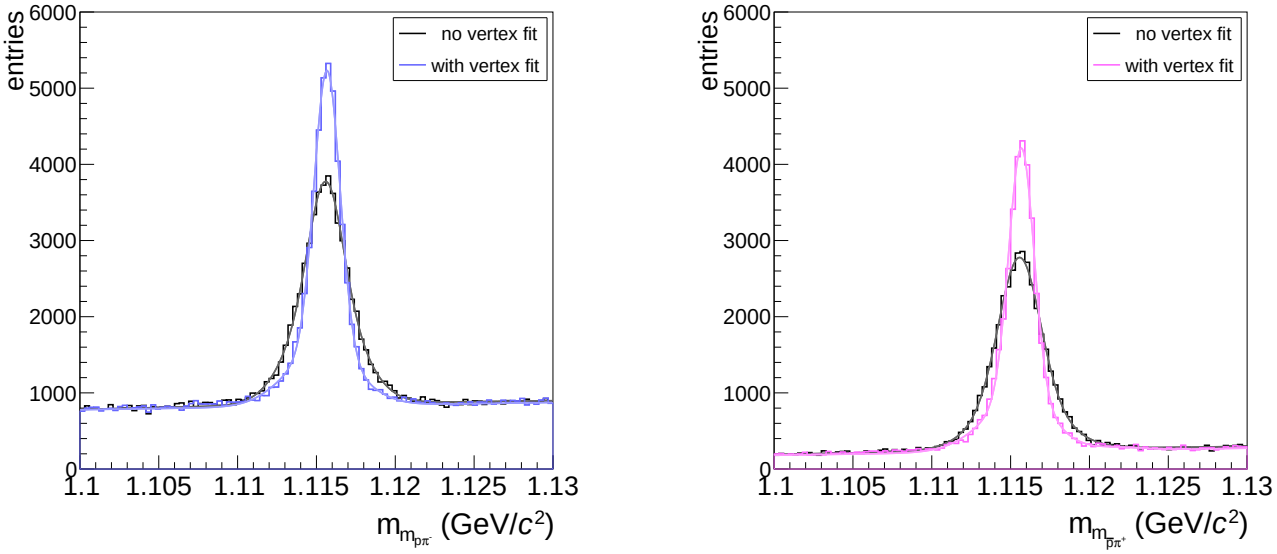

(a) Λ^0 reconstruction.

(b) $\bar{\Lambda}^0$ reconstruction.

Figure 3.3: Invariant mass spectra of Λ^0 and $\bar{\Lambda}^0$ reconstruction with (coloured) and without applied vertex fit of D4230 and applied selections (table 5).

The Full Width at Half Maximum (FWHM) for each of the signal peaks is determined by a fit function (equation 3.14). To quantify the change of the width, the ratio of the two different FWHM is given by

$$\text{ratio} = \frac{\text{FWHM}_{\text{with vertex fit}}}{\text{FWHM}_{\text{no vertex fit}}} \quad . \tag{3.8}$$

	$\text{FWHM}_{\text{no vertex fit}}$ (MeV)	$\text{FWHM}_{\text{with vertex fit}}$ (MeV)	ratio
Λ^0	4.50	2.78	0.62
$\bar{\Lambda}^0$	4.04	2.49	0.62

Table 6: FWHM of Λ^0 and $\bar{\Lambda}^0$ with and without applied vertex fit

3.4. The Invariant Mass and the Missing Mass

Since the missing mass technique led to numerous outstanding discoveries in the XYZ sector within the last two decades [110, 111, 112], a brief introduction is given in the following section. In 2012 the Belle collaboration observed for the first time an unpredicted new charmonium-like state, the $X(3940)$ produced in the process $e^+e^- \to J/\psi X(3940)$ [111].

As the objective of this work is a contribution to the understanding of the XYZ states, the initial approach had been this technique and was replaced by the one described in section 3.5.

The invariant mass m_0 calculated by the particle's energy E and its momentum $\boldsymbol{p}$ is equal to the mass in the rest frame of the particle (or *any* frame) and is invariant under Lorentz transformations:

$$m_0^2 = E^2 - ||\boldsymbol{p}||^2 \qquad \text{in natural units where } c = 1. \tag{3.9}$$

In a two-particle decay (subscript 1 and 2) the square of the invariant mass (m_0) of the previous existing particle can be calculated with:

$$m_0{}^2 = (E_1 + E_2)^2 - ||\boldsymbol{p}_1 + \boldsymbol{p}_2||^2 \tag{3.10}$$

Lets assume following reaction for a description of the missing mass (m_{miss}):

$$e^+e^- \to Y \to \Lambda^0 X \qquad \text{with: } \Lambda^0 \to p\pi^- \tag{3.11}$$

where Y is a charmonium-like state. Figure 3.4 shows the feynman diagram of this assumed process (with $X \equiv \bar{\Lambda}^0, \overline{p}\,K^+, \overline{p}\,K^+\pi^0$ e.g.).

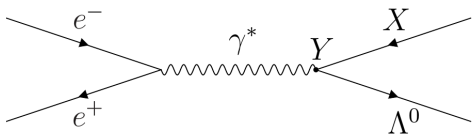

Figure 3.4: Feynman diagram of $e^+e^- \to Y \to \Lambda^0 X$.

The initial beam energy (carried by e^+e^-) is transformed by the leptonic annihilation into a virtual photon (γ^*) and then converted into a massive particle.

The mass of the produced particle equates the initial beam energy (the 4-momentum $\boldsymbol{P}_{e^+e^-}$). Therefore, the sum of the 4-momenta of its decay products is also equal to the initial beam energy. For instance, Λ^0 itself decays into a p and a π^- and its 4-momentum is reconstructed using the 4-momenta of the two daughter particles. In consideration of equation 3.9, and with known 4-momenta $\boldsymbol{P}_{e^+e^-}$ and $\boldsymbol{P}_{\Lambda^0}$, the mass of the complete recoils system (m_{miss}) can be calculated [113].

$$m_{miss}{}^2 = (\boldsymbol{P}_{e^-e^+} - \boldsymbol{P}_{\Lambda^0})^2 \qquad \text{with} \quad \boldsymbol{P} = (E, \boldsymbol{p}) \tag{3.12}$$

$$m_{miss} = \sqrt{(E_{e^-e^+} - E_{\Lambda^0})^2 - ||\boldsymbol{p}_{e^-e^+} - \boldsymbol{p}_{\Lambda^0}||^2} \tag{3.13}$$

The recoiling hadrons appear as peaks in the recoil mass distribution. Figure 3.5 shows the inclusive J/ψ reconstruction at Belle with a distinct peak at $3\,\mathrm{GeV}/c^2$, that we interprete as the η_c. Here, the recoil mass is $M_{recoil}(J/\psi) = ((E_{\sqrt{s}} - E^*_{J/\psi})^2 - p^*_{J/\psi}{}^2)^{1/2}$, where $E^*_{J/\psi}$ is the

J/ψ center-of-mass energy after the mass constraint. The center-of-mass momentum $p^*_{J/\psi}$ is required to be greater than 2.0 GeV/c to remove background events.

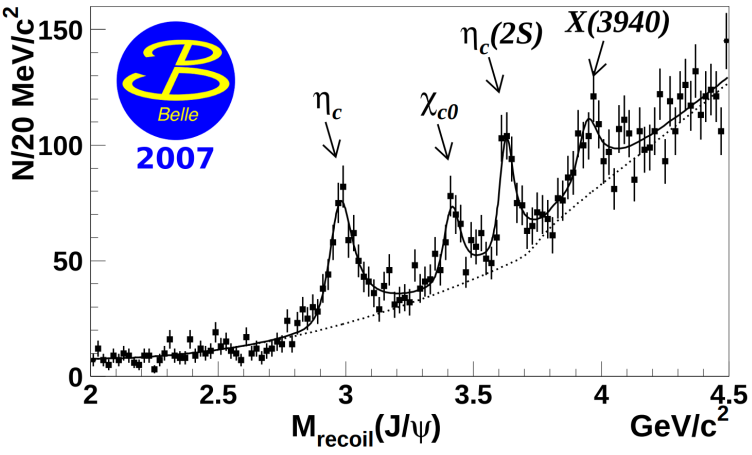

Figure 3.5: Belle collaboration: first observation of the charmonium-like state $X(3940)$. The distribution of masses recoiling against the reconstructed J/ψ in inclusive $e^+e^- \to J/\psi X$ events. The solid curve corresponds to the fit function in full, the dashed to the background part [111].

Therefore, the missing mass technique is effective for the analysis of charmonium final states (e.g. J/ψ) with a recoiling system of hadrons. As no distinct signals are observed in the missing mass (figure 3.6), other techniques are necessary to extract information. Thus, this work is focused on the measurement of the energy-dependent cross-section of the inclusive reaction $e^+e^- \to \Lambda^0 X$ (+ *c.c.*). Herefore, the proton-momentum dependent analysis has been developed (section 3.5).

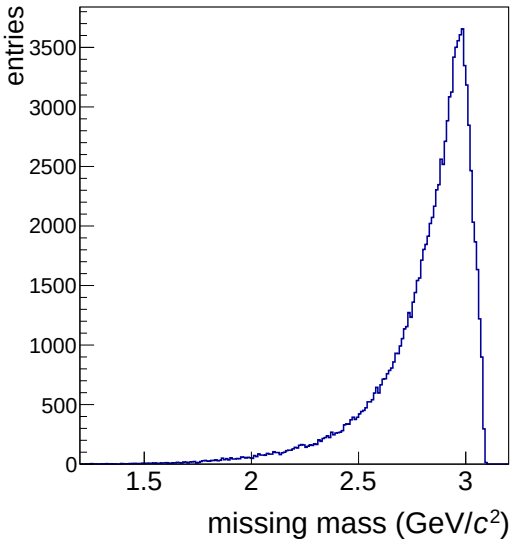

(a) Λ^0 candidates of measured data.

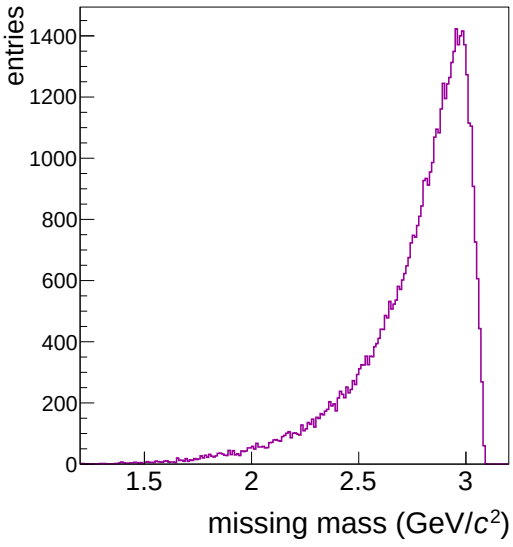

(b) $\bar{\Lambda}^0$ candidates of measured data

Figure 3.6: Missing mass spectra of D4230 with applied selections (table 5). In contrast to figure 3.5 no distinct signals appear in the missing mass distribution.

3.5. Inclusive Yield and Reconstruction Efficiency

In order to observe charmonium-like resonances such as $Y(4230)$ in e^+e^- formation reactions [114] an energy dependent cross-section $\sigma(\sqrt{s})$ needs to be determined. The cross-section is based on the number (yield) of reconstructed signal particles, the decay products of the short-lived resonances.

In this analysis, the yield measurement and the efficiency calculation are performed using sideband-subtracted momentum distributions of (anti-)protons from Λ^0 ($\bar{\Lambda}^0$) candidates. The use of momentum distributions is motivated in section 3.2.2. The sideband subtraction approach is based on invariant mass spectra of Λ^0 ($\bar{\Lambda}^0$) candidates, reconstructed by (anti-)protons and charged pions. Hereinafter shown spectra with an applied momentum selection utilise boundaries of $p_{low} = 0.28\,\mathrm{GeV}/c$ and $p_{high} = 1.40\,\mathrm{GeV}/c$, which are identified as most optimal (section 3.6.1). The selections of table 5 are applied on all following spectra.

3.5.1. The Sideband Subtraction

In order to remove the background events in the momentum spectra used afterwards for efficiency and yield calculation an identification of the signal and sideband regions is essential. The limits of the signal and the two sideband regions are determined within the invariant mass spectra of measured data and *generic MC* with and without applied momentum cut as follows: a fit function

$$f(x) = \underbrace{\frac{A_0}{\sqrt{2\,\pi}\cdot(1+A_1+A_2)}\cdot\left(g_0(x)+g_1(x)+g_2(x)\right)}_{\text{signal part: } f_{sig}} + \underbrace{p_0+p_1\,x+p_2\,x^2}_{\text{background part: } f_{bg}} \tag{3.14}$$

with $A_i, p_i \in \mathbb{R}$ and three Gaussian distributions

$$g_0(x) = \frac{1}{\sigma_0}\,e^{-\frac{1}{2}\left(\frac{x-\mu_0}{\sigma_0}\right)^2},\; g_1(x) = \frac{A_1}{\sigma_1}\,e^{-\frac{1}{2}\left(\frac{x-\mu_0-\mu_1}{\sigma_1}\right)^2} \text{ and } g_2(x) = \frac{A_2}{\sigma_2}\,e^{-\frac{1}{2}\left(\frac{x-\mu_0-\mu_2}{\sigma_2}\right)^2}.$$

is adapted to the invariant mass spectra of Λ^0 ($\bar{\Lambda}^0$) candidates. A_i are normalisation factors. The boundaries of the signal region are set to $1.1025\,\mathrm{GeV}/c^2$ and $1.1275\,\mathrm{GeV}/c^2$, meeting the specification that the selected fraction of the signal component of the fit function is at least 99.0% of the total integral for all 21 samples of measured data. The inner boundaries of the sideband regions (*sb left* and *sb right*) are set at a distance of $0.0025\,\mathrm{GeV}/c^2$ to the signal region ($1.100\,\mathrm{GeV}/c^2$ and $1.1300\,\mathrm{GeV}/c^2$). The outer boundaries of the sideband regions are chosen in a way, that the integral of the background function of both sidebands matches the integral of the background function in the signal region. This procedure is realised for each data and *generic MC* sample individually, so each set of sideband boundaries is calculated separately.

Figure 3.7 shows the invariant mass distributions of reconstructed MC particles, figure 3.8 of Λ^0 ($\bar{\Lambda}^0$) candidates of measured data. The integrals are displayed as follows: Sideband regions are hatched diagonally in light blue, the signal region is horizontally hatched in pink.

The background level of the Λ^0 reconstruction (a) is higher than the one of the $\bar{\Lambda}^0$ reconstruction (b) for both, MC particles and candidates of measured data. This leads to larger uncertainties in the respective reconstruction efficiency and yield measurement, as both are determined using sideband subtractions. This effect is reflected in figure 3.14b.

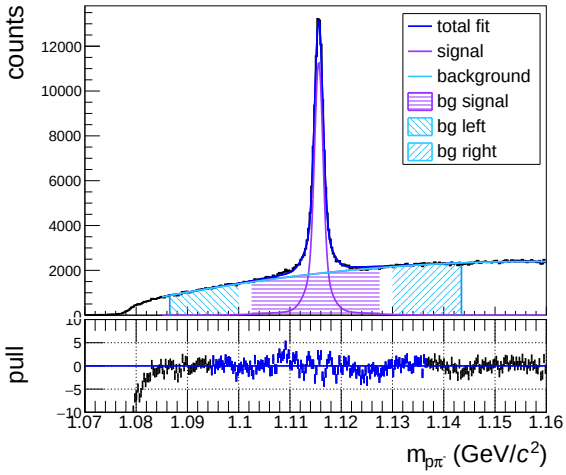

(a) Λ^0 candidates ($m_{p\,\pi-}$).

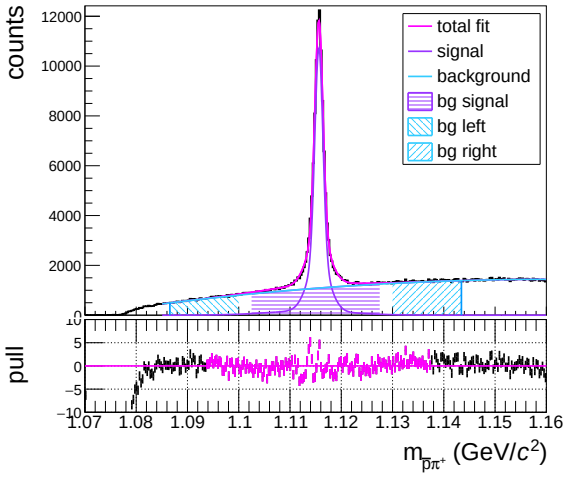

(b) $\bar{\Lambda}^0$ candidates ($m_{\bar{p}\,\pi+}$).

Figure 3.7: Invariant mass spectra of reconstructed MC particles of D4230 with applied selections (table 5).

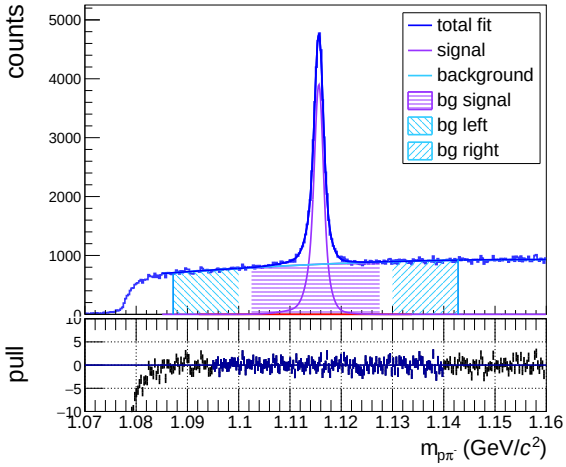

(a) Λ^0 candidates ($m_{p\,\pi-}$).

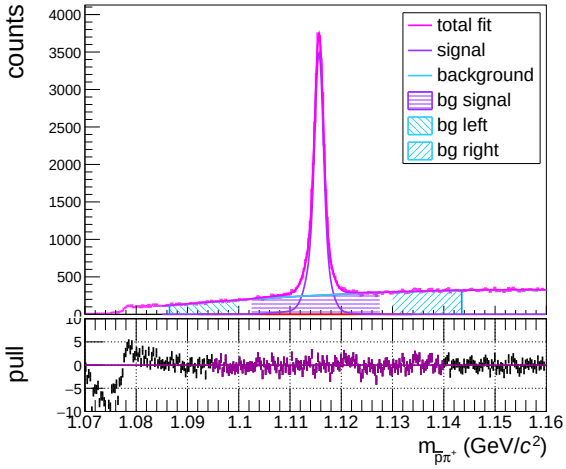

(b) $\bar{\Lambda}^0$ candidates ($m_{\bar{p}\,\pi+}$).

Figure 3.8: Invariant mass spectra of Λ^0 and $\bar{\Lambda}^0$ candidates of data (D4230) with applied selections (table 5).

The differences in the signal and the background shape between data (figure 3.8) and *generic MC* (figure 3.7) are an additional motivation for the proton momentum dependent analysis.

In the interests of completeness, it should be noted, that each proton momentum selection needs a respective estimation of the sideband boundaries. Therefore, the invariant mass spectra are generated considering the cut on the momentum of the proton used to reconstruct the Λ^0 candidate. The invariant mass spectra differ, hence the estimated sideband boundaries differ slightly, too. Subsequently, these differing sideband regions lead to slightly different bin entries within the region of interest in the efficiency-corrected yield distributions (figure 3.19).

Generally, the sideband-subtracted proton momentum spectrum results from two previous proton momentum spectra: the first is filled, if the determined invariant mass using this proton candidate is within the mass region of the signal.

The latter is filled, if the determined invariant mass using this proton candidate is within the mass regions of the sidebands. Then, these two spectra are subtracted binwise.

3.5.2. Efficiency Calculation

In general the reconstruction efficiency ε is defined as:

$$\varepsilon = \frac{\text{number of reconstructed particles}}{\text{number of generated particles}} \tag{3.15}$$

using MC simulations to have access to the number of generated particles. In this analysis, the reconstruction efficiency is calculated per momentum bin (ε_i) to adress the divergence of *generic MC* from measured data. A momentum bin has the width of 10 MeV/c.

The efficiency per bin ε_i is calculated by the ratio of the number of reconstructed particles per bin $n_{reco,i}$ to the number of generated particles per bin $n_{gen,i}$:

$$\varepsilon_i = \frac{n_{reco,i}}{n_{gen,i}} \tag{3.16}$$

In order to take into account, that the spectra providing $n_{reco,i}$ are generated by sideband (sb) subtracted momentum spectra of the signal region (sig), the efficiency error per bin ($\mathrm{d}\varepsilon_i$) is given by:

$$\mathrm{d}\varepsilon_i = \varepsilon_i \cdot \sqrt{\left(\frac{\mathrm{d}n_{reco,i}}{n_{reco,i}}\right)^2 + \left(\frac{\mathrm{d}n_{gen,i}}{n_{gen,i}}\right)^2} \qquad \text{with } \mathrm{d}n_{gen,i} = \sqrt{n_{gen,i}} \quad \text{and} \tag{3.17}$$

$$n_{reco,i} = n_{sig,i} - n_{sb_i},\ \mathrm{d}n_{reco} = \sqrt{\mathrm{d}{n_{sig,i}}^2 + \mathrm{d}{n_{sb_i}}^2},\ \ \mathrm{d}n_{sig,i} = \sqrt{n_{sig,i}}\ ,\ \ \mathrm{d}n_{sb_i} = \sqrt{n_{sb_i}} \quad \text{follows}$$

$$\mathrm{d}\varepsilon_i = \varepsilon_i \cdot \sqrt{\frac{n_{sig,i} + n_{sb_i}}{\left(n_{sig,i} - n_{sb_i}\right)^2} + \frac{1}{n_{gen}}} \tag{3.18}$$

The spectra of the 12 *generic MC* samples in figure 3.9 are the momentum distributions of generated MC protons, providing $n_{gen,i}$ in equation 3.16.

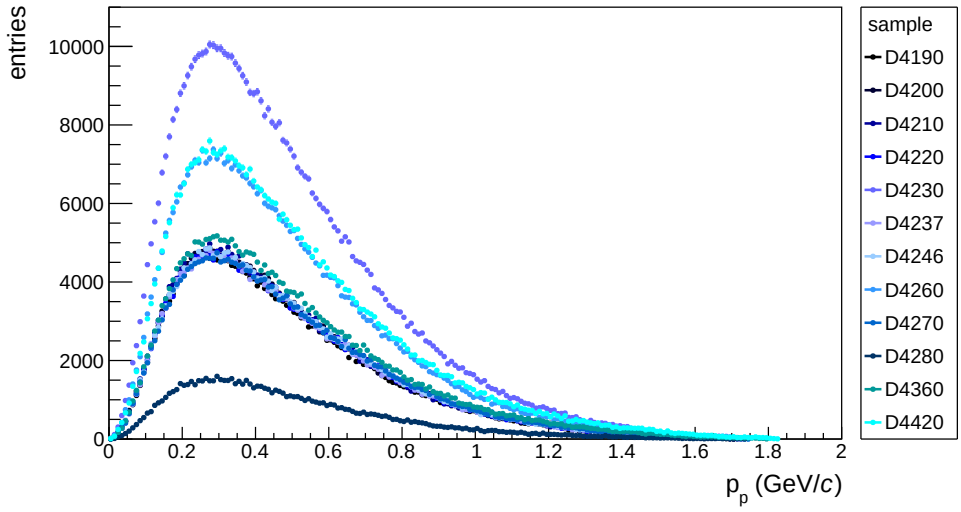

Figure 3.9: *Generic MC*: Momentum spectra of MC generator protons.

The following steps of the analysis are explained by means of protons from Λ^0 candidates to provide a better overview. The details for $\bar{\Lambda}^0$ candidates can be found in the appendix.

The momentum dependent efficiency $\varepsilon(p)$ (figure 3.11) is given by the bin-wise ratio of the distribution of reconstructed protons (figure 3.10) and the corresponding distribution of the generated proton momenta (figure 3.9). Removing momenta with large relative uncertainties in the efficiency improves the precision of the yield measurement.

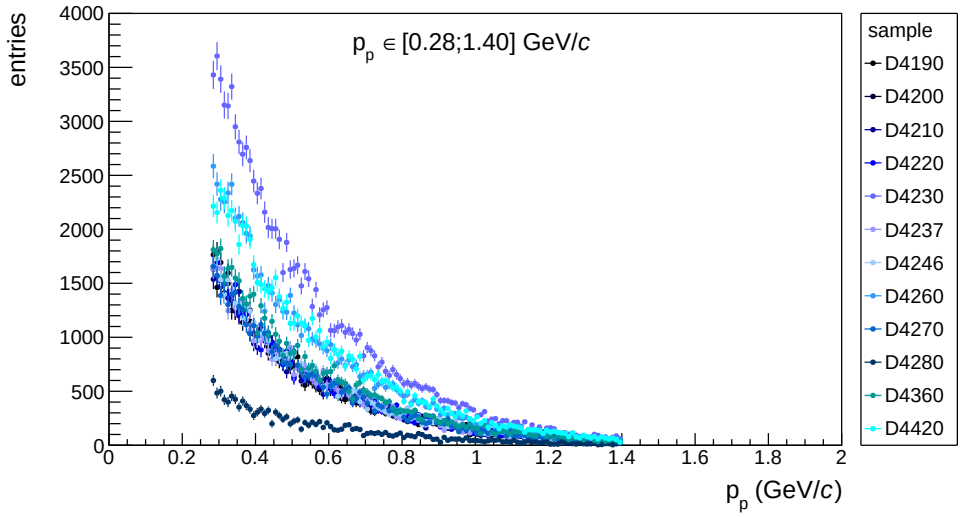

Figure 3.10: Sideband-subtracted momentum spectra of reconstructed MC protons with applied selections (table 5).

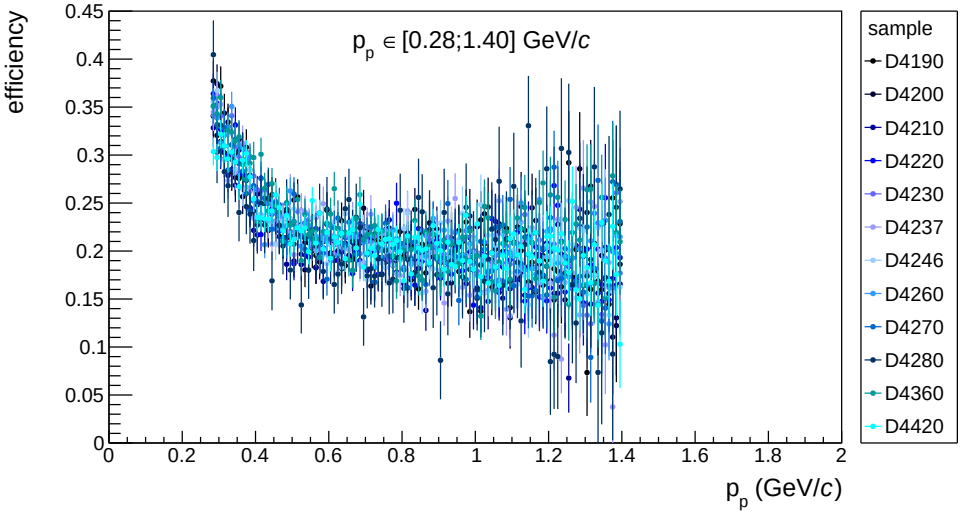

Figure 3.11: Distributions of reconstruction efficiency per proton momentum bin with applied selections (table 5).

3.5.3. Yield Measurement

In order to determine the yield per bin (n_i), and subsequently the efficiency-corrected yield (N/ε), sideband-subtracted momentum distributions of protons from Λ^0 candidates of measured data (figure 3.12) are generated. Protons with momenta smaller than $0.2\,\mathrm{GeV}/c$ are scarcly reconstructed, as like for MC protons (figure 3.10). The efficiency-corrected momentum dependent yield (figure 3.13) is given by the bin-wise ratio of the distribution of protons from Λ^0 candidates $n(p)$ (figure 3.12) and the corresponding efficiency distribution $\varepsilon(p)$ (figure 3.11). The sum of n_i/ε_i per p_p bin within the range of the momentum selction gives N/ε, the efficiency-corrected yield of Λ^0, the basis of the following cross-section calculation. For better clarity, the n_i/ε_i values outside the momentum selection are omitted in figure 3.13.

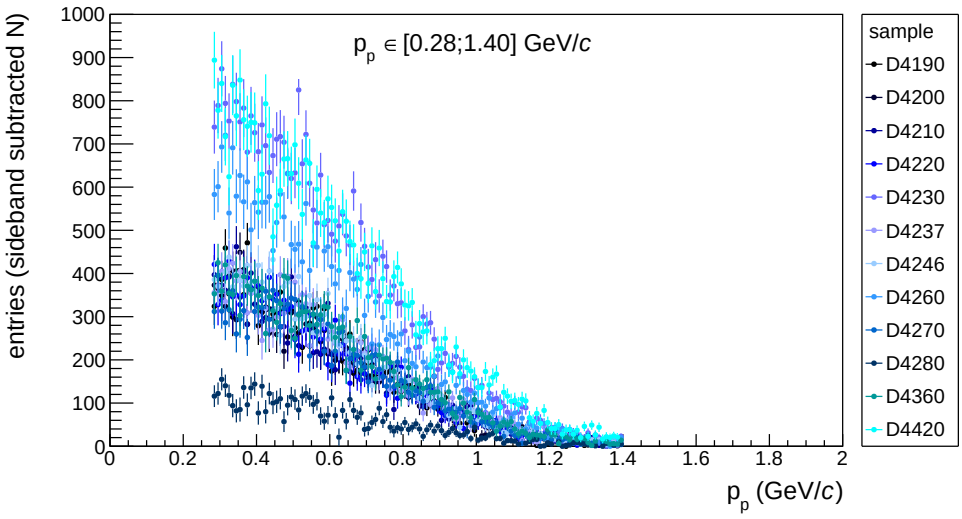

Figure 3.12: Sideband subtracted momentum spectra of reconstructed protons from Λ^0 candidates of measured data with applied selections (table 5).

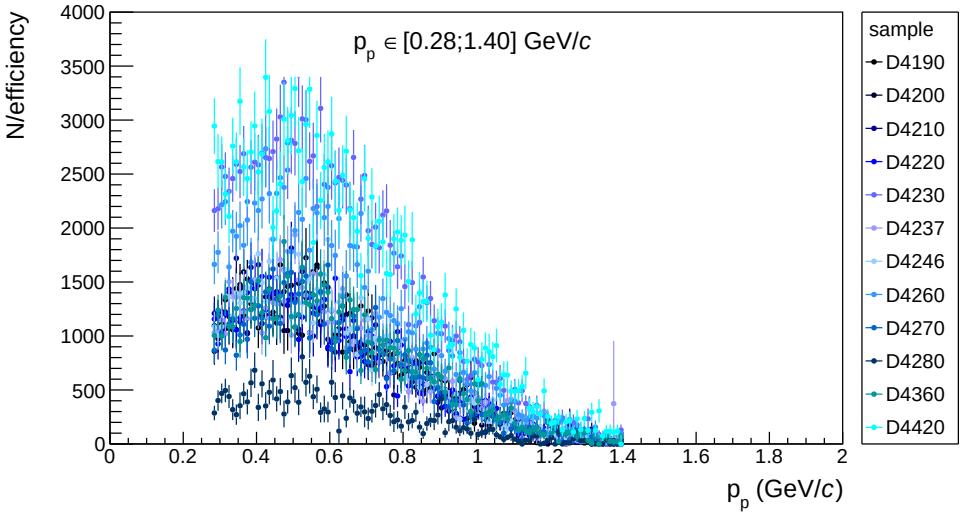

Figure 3.13: Sideband-subtracted momentum distribution of reconstructed protons from Λ^0 candidates divided by the reconstruction efficiency with applied selections (table 5).

3.5.4. Efficiency Calculation: Adressing Data Samples of Lacking Generic MC

For data samples without corresponding *generic MC*, the efficiency correction is estimated from the other *generic MC* datasets. Basically, each of the 12 existing efficiency distributions is averaged to one efficiency value per center-of mass energy $\hat{\varepsilon}(\sqrt{s})$. Then, an interpolation along the center-of-mass energy gives the required $\hat{\varepsilon}_{calc}$.

Beginning with the condition that must be fulfilled

$$\sum \frac{n_i}{\varepsilon_i} \stackrel{!}{=} \frac{\sum n_i}{\hat{\varepsilon}} \tag{3.19}$$

where i is running from p_{low} to p_{high}, $\sum n_i/\varepsilon_i$ is the efficiency corrected yield $N/\varepsilon = N^*$ and $\sum n_i$ is the yield N. From this follows

$$\hat{\varepsilon} = \frac{N}{\sum \frac{n_i}{\varepsilon_i}} \quad \text{with the error } \mathrm{d}\hat{\varepsilon} = \frac{1}{N^* \cdot N} \cdot \sqrt{\sum \left(N^* - \frac{N}{\varepsilon_i}\right)^2 \cdot \mathrm{d}n_i^2 + N^2 \cdot \sum \frac{n_i}{\varepsilon_i^2} \cdot \mathrm{d}\varepsilon_i^2} \tag{3.20}$$

where $\mathrm{d}n = \sqrt{n}$ is the error of the yield per bin and the error of the efficiency per bin is $\mathrm{d}\varepsilon_i$, given by equation 3.17. Therefore, the distribution of protons from Λ^0 candidates $n(p)$ is divided bin-wise by the efficiency distribution $\varepsilon(p)$, and is then summed up and used as divisor of the yield. The efficiency $\hat{\varepsilon}(\sqrt{s})$ is plotted versus the center-of-mass energy (figure 3.14) and a linear fit is applied

$$f_{\hat{\varepsilon}}(\sqrt{s}) = p_0 + p_1 \cdot \sqrt{s} \quad . \tag{3.21}$$

For the distribution without momentum cut, shown left, a constant fit function is used, due to the pronounced variation of the values of $\hat{\varepsilon}$. The respective efficiencies $\hat{\varepsilon}_{calc}$ for data samples without existing *generic MC* are calculated based on $f_{\hat{\varepsilon}}(\sqrt{s})$.

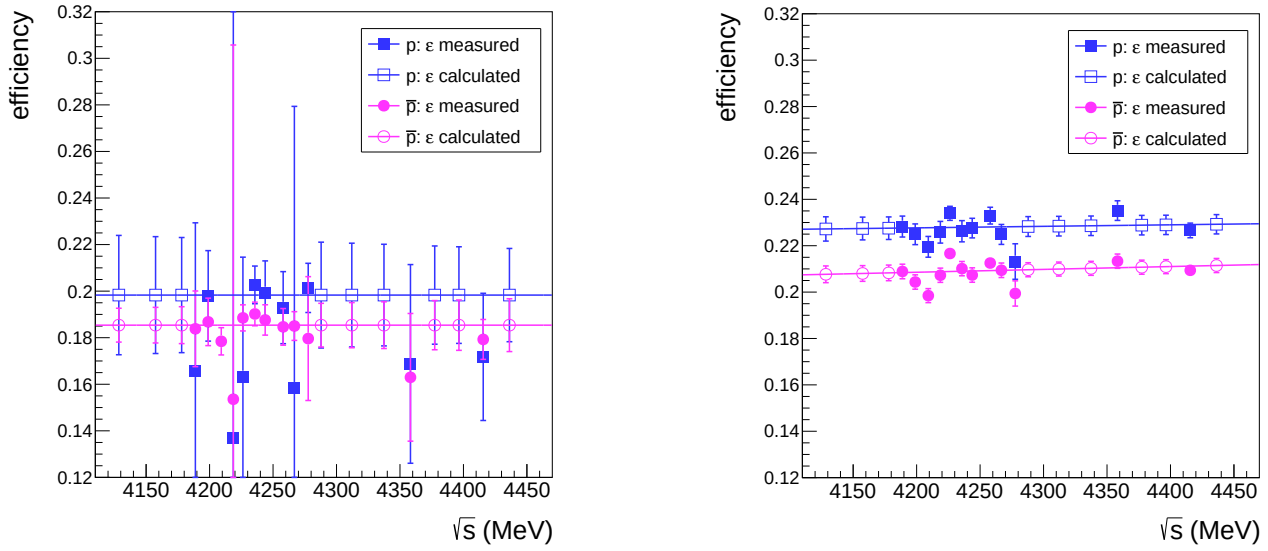

(a) No p_p cut applied.

(b) With applied p_p cut.

Figure 3.14: Efficiency as a function of the center-of-mass energy.

The reconstruction efficiency of protons (p) and antiprotons ($\overline{p}$) with applied cut is almost constant across the center-of-mass energy. Because of the rejection of the low momentum bins (momenta below around $0.2\,\mathrm{GeV}/c$) with low ε_i, the cut increases $\hat{\varepsilon}$. The efficiency ε_i is low in this range due to the detector acceptance (compare figure 3.9 with figure 3.10). This shifting effect on the efficiency is adressed by the detection acceptance (section 3.7).

The error $\mathrm{d}\hat{\varepsilon}_{calc}$ consists of two errors: $\mathrm{d}\hat{\varepsilon}_{calc,1}$ and $\mathrm{d}\hat{\varepsilon}_{calc,2}$. The first error includes the uncertainty of the fit function $f_{\hat{\varepsilon}}(\sqrt{s})$, using its errors of the parameters ($\mathrm{d}p_0$ and $\mathrm{d}p_1$) and the non-diagonal entry of its covariance matrix (c_{01}) and is given by

$$\mathrm{d}\varepsilon_{calc,1} = \sqrt{dp_0^2 + (\sqrt{s}\cdot dp_1)^2 + 2\cdot(\sqrt{s}\cdot c_{01})} \quad . \tag{3.22}$$

The second error is determined analogously like $\hat{\varepsilon}_{calc}$: at first, the errors of the efficiencies $\mathrm{d}\hat{\varepsilon}$ of data samples with *generic MC* are plotted versus the $\sqrt{s}$ of the corresponding data sets (figure 3.15) and a linear fit is applied $f_{\mathrm{d}\hat{\varepsilon}}(\sqrt{s}) = q_0 + q_1\cdot\sqrt{s}$. Since the values of $\mathrm{d}\hat{\varepsilon}$ show a distinct variation, left figure, a constant fit function is used. The respective errors $\mathrm{d}\hat{\varepsilon}_{calc}$ for data samples without existing *generic MC* are calculated based on $f_{\mathrm{d}\hat{\varepsilon}}(\sqrt{s})$. Subsequently, $\mathrm{d}\hat{\varepsilon}_{calc}$ is the squared sum of both errors given by

$$\mathrm{d}\hat{\varepsilon}_{calc} = \sqrt{\mathrm{d}\hat{\varepsilon}_{calc,1}{}^2 + \mathrm{d}\hat{\varepsilon}_{calc,2}{}^2} \tag{3.23}$$

and is used as error of the interpolated efficiencies in figure 3.14.

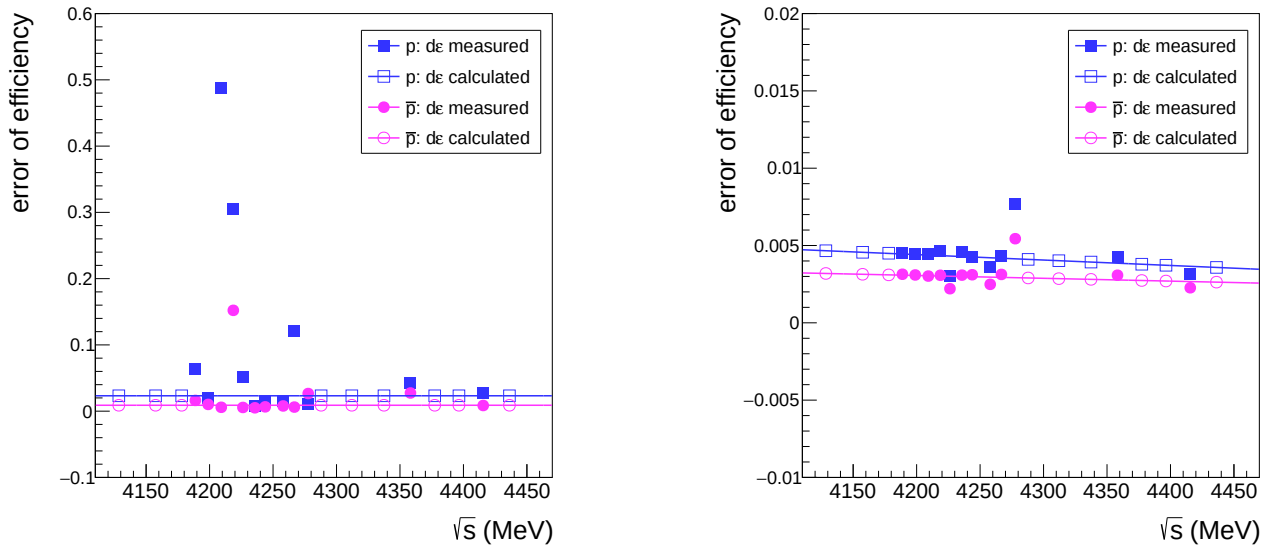

(a) No p_p cut applied.

(b) With applied p_p cut.

Figure 3.15: Error of the efficiency as a function of the center-of-mass energy.

3.5.5. The Efficiency-Corrected Yield

The efficiency-corrected yield $N/\varepsilon(\sqrt{s})$ for data samples with existing *generic MC* is the sum of the bin contents of the n/ε distribution (figure 3.13). For data samples lacking *generic MC*, the yield is obtained using a sideband-subtracted momentum spectrum of protons from Λ^0 candidates, like in figure 3.12. The sum of this distribution within the range of the momentum selection gives $N(\sqrt{s})$. Dividing $N(\sqrt{s})$ by $\hat{\varepsilon}_{calc}(\sqrt{s})$ (equation 3.20) gives $N/\hat{\varepsilon}(\sqrt{s})$, open symbols in figure 3.16.

The values of $N/\varepsilon(\sqrt{s})$ in figure 3.16 diverge widely among the data samples and must be divided by their respective time-integrated luminosities, inter alia, in order to identify enhancements in the energy-dependent cross-section $\sigma(\sqrt{s})$.

Most prominent value is D4180, with a time-integrated luminositiy ($\mathcal{L}_{int}$) of 3189.0 pb^{-1}, as the duration of data accumulation had been more than five months due to a second physics motivation. The duration of data accumulation for samples taken in 2019 are comparable in size, therefore the $N/\varepsilon(\sqrt{s})$ are more similar (table 4).

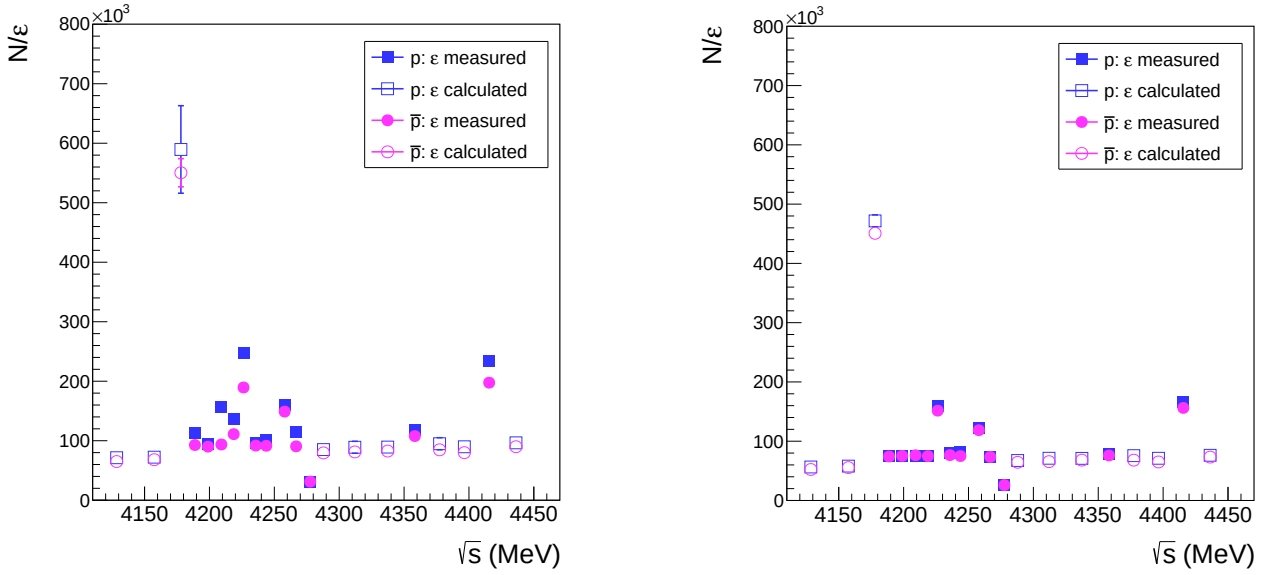

(a) No p_p cut applied.

(b) With applied p_p cut.

Figure 3.16: Efficiency-corrected yield of p (blue squares) and $\overline{p}$ (pink circles) of Λ^0 and $\bar{\Lambda}^0$ candidates plotted versus $\sqrt{s}$. Open symbols represent yields based upon ε_{calc} values.

Figure 3.16 shows the efficiency-corrected yield (N/ε) since this value is calculated at once for the 12 data samples with *generic* MC. For the nine data samples without *generic* MC, the reconstruction efficiency and the yield are determined independently.

3.6. The Proton Momentum Cut

The proton momentum cut is applied in order to reduce the error of the efficiency-corrected yield (N/ε) and therefore of the cross-section σ_{Λ^0}. The improvement of the data quality by applying a momentum cut is apparent, comparing the findings of figure 3.16a (no cut applied) with those of figure 3.16b. First, the errors are significantly smaller. Secondly the efficiency-corrected yields of both species are much more consistent. This consistency is a benefit for a simultaneous fit of the energy-dependent cross sections $\sigma(\sqrt{s})$ (section 5.1).

The bin content of the sideband-subtracted spectrum ($n_{reco}(p)$) after the simulation of the particle propagation and passing the reconstruction procedure is divided by the bin content of the spectrum obtained directly from the generator ($n_{gen}(p)$), giving the reconstruction efficiency distribution $\varepsilon(p)$ (equation 3.16). The reconstruction efficiency distribution $\varepsilon(p)$ shows large uncertainties for momenta higher than 1.2 GeV/c (figure 3.18). Therefore a momentum cut (p_{high}) is required. Then again, bins with very low occupancy of the reconstructed spectrum, either for measured data (figure 3.12) or for *generic MC* (figure 3.17), cause large uncertainties in the efficiency-corrected yield distribution for momenta smaller than 0.2 GeV/c (black distribution in figure 3.19). Thus, an appropriate lower momentum cut (p_{low}) must be determined.

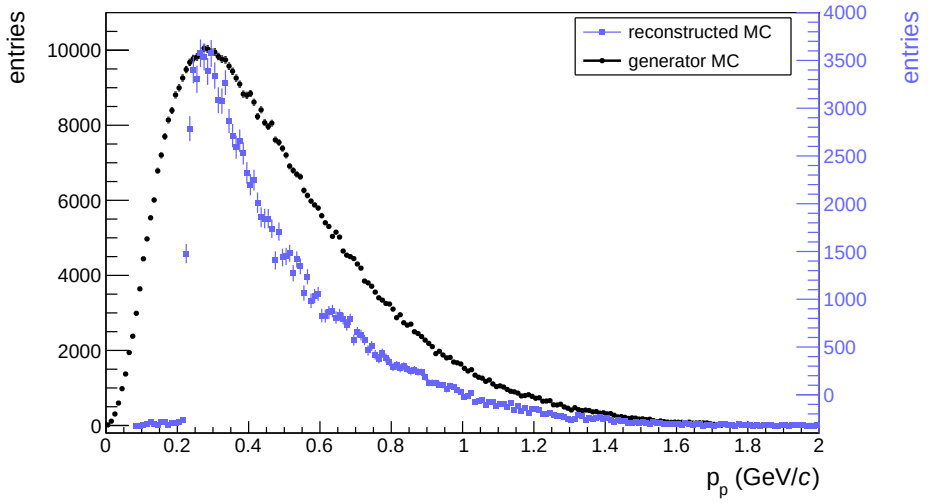

Figure 3.17: *Generic MC* of D4230: Momentum spectra of protons from Λ^0 candidates before (black, left scale) and after (blue, right scale) the reconstruction procedure.

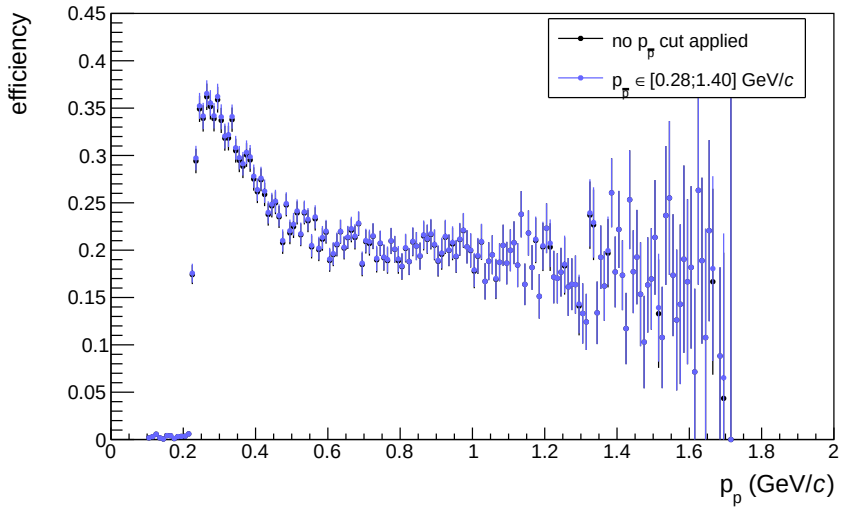

Figure 3.18: Reconstruction efficiency distributions of protons from Λ^0 candidates of D4230 with and without applied momentum cut.

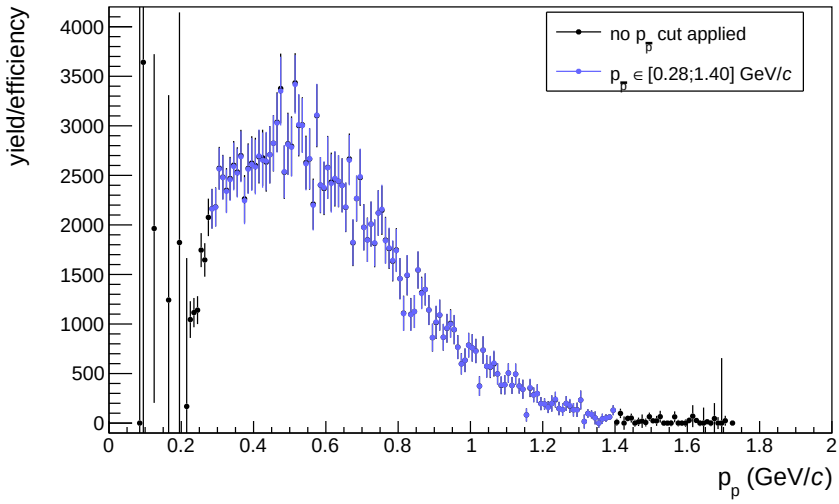

Figure 3.19: Efficiency-corrected yield distributions of protons from Λ^0 candidates of D4230 with and without applied momentum cut.

Bins outiside the momentum selection are omitted for better clarity for the distribution with applied cut (figure 3.19). The minor deviations within the selected momentum range of the distributions with (blue) and without (black) applied momentum cut (figures 3.18 and 3.19) are caused by slightly different sideband boundaries for the sideband subtraction (section 3.5.1).

3.6.1. Cut Optimisation

The momentum cut on (anti-)protons has to fulfill two conditions: improvement of the consistency of the cross-sections between particle and antiparticle (σ_{Λ^0} and $\sigma_{\bar{\Lambda}^0}$) and reduction of the uncertainty of the efficiency-corrected yield. Connecting both, the optimal cut can be identified.

First Figure of Merit: Deviation of the Cross-Sections

The energy dependent cross-section $\sigma(\sqrt{s})$ will be discussed in detail in section 3.8. Briefly introduced: $\sigma_{\Lambda^0}(\sqrt{s})$ is the efficiency-corrected yield N/ε of Λ^0 candidates divided by the time-integrated luminosity $\mathcal{L}_{int}$ and further quantities, which are approximately constant along $\sqrt{s}$.

A greater consistency of the energy dependent cross-sections between particle and antiparticle ($\sigma_{\Lambda^0}(\sqrt{s})$ and $\sigma_{\bar{\Lambda}^0}(\sqrt{s})$) allows a simultaneous fit on both distributions (section 5.2.1). Therefore a minimum in the distribution of the averaged divergence per cut leads to a justified momentum cut (cross-sections based on interpolated efficiencies ε_{calc} are excluded):

$$\Delta\sigma_i = \left(1 - \frac{\sigma_{\bar{\Lambda}^0}}{\sigma_{\Lambda^0}}\right)_i \qquad \text{divergence per } \sqrt{s}_i \quad . \tag{3.24}$$

The mean of the divergence per center-of-mass energy is

$$\langle\Delta\sigma\rangle = \frac{1}{12}\sum_{i=1}^{12}|\Delta\sigma_i| \qquad \text{with } \sqrt{s}_1 = 4190,\ \sqrt{s}_2 = 4200,\ \ldots\ \sqrt{s}_{12} = 4420 \text{ in MeV}. \tag{3.25}$$

Figure 3.20 shows the divergences of the cross-sections with and without applied proton momentum selection. Besides the two outliers of D4210 and D4280, the divergences are greater

in total for the approach without momentum selection. For better comparability, the scales of the y-axes of the figures 3.20a and 3.20b are the same, even though the value of D4210 is out of range ($\Delta\sigma_3 = 2.1$). The smaller the mean of the divergence $\langle\Delta\sigma\rangle$, the more convergent are the cross-sections of Λ^0 and $\bar{\Lambda}^0$ for all center-of-mass energies.

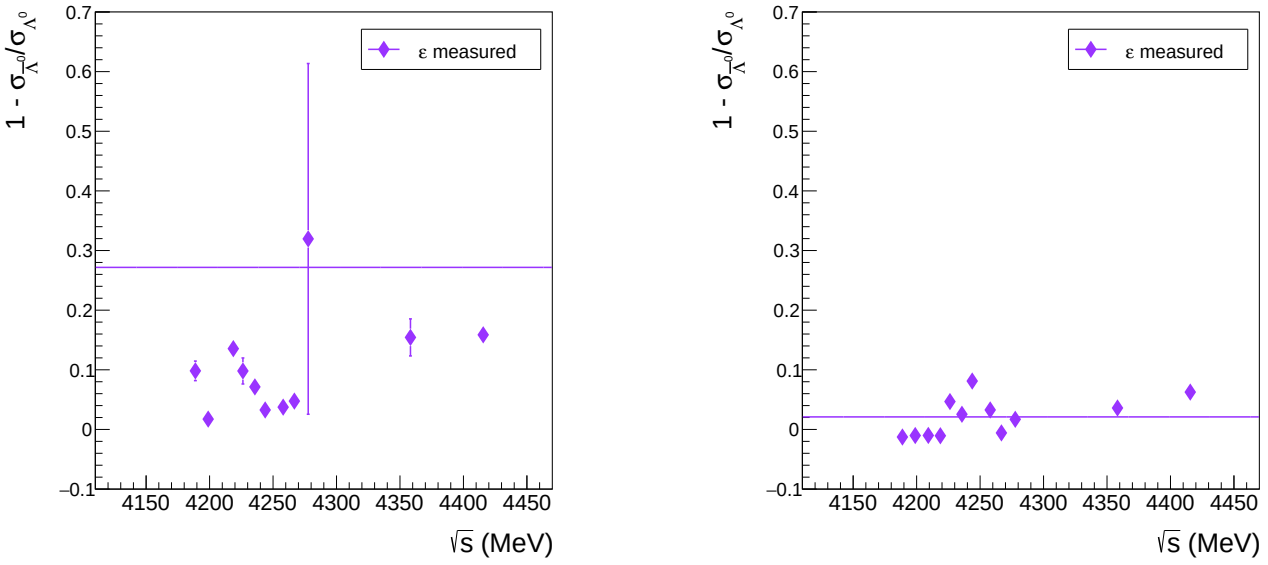

(a) No p_p cut applied.

(b) With applied p_p cut.

Figure 3.20: Divergence of the cross-sections of Λ^0 and $\bar{\Lambda}^0$ plotted against the center-of-mass energy $\sqrt{s}$. A solid line depicts the mean of the deviation. Left figure: The divergence of the data sample D4210 with a value of 2.4 is located outside the range.

Considering figures 3.11 and 3.19, a lower (p_{low}) and a higher (p_{high}) momentum boundary is required. The sensitivity of $\langle\Delta\sigma\rangle$ is more pronounced on the lower than on higher boundary due to the steep slope of the momentum distribution of reconstructed protons at around $0.2\,\mathrm{GeV}/c$. Therefore a momentum range of $[0.0; 0.5]\,\mathrm{GeV}/c$ is scanned in 14 steps to determine the optimal lower cut-off value p_{low}. This scan is performed for three different values of the higher momentum boundary ($p_{high} \in \{1.35, 1.40, 1.45\}\,\mathrm{GeV}/c$). For each combination of a lower and a higher boundary (14×3 scan points) the mean of the divergences of the cross-sections $\langle\Delta\sigma\rangle$ is calculated. Then, the means of the scan points are plottet against p_{low} (figure 3.21).

Even though the distributions of the three higher momentum boundaries are hardly distinguishable, their repective errors are different: the error of the distribution of $p_{high} = 1.35\,\mathrm{GeV}/c$ is the smallest. The minimum of the three distributions is at around $p_{low} = 0.28\,\mathrm{GeV}c$.

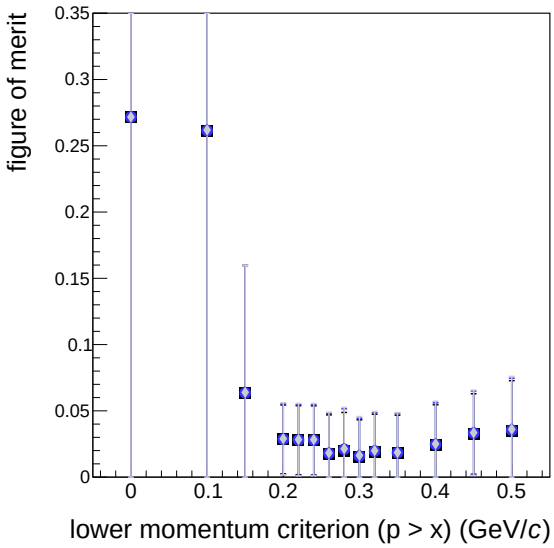

Figure 3.21: The three $\langle \Delta\sigma \rangle$ distributions as functions of the lower momentum cut.

Second Figure of Merit: Minimum Relative Error

The second requirement in the determination of a justified momentum cut is the inverse of the relative error of the yield, also called statistical significance. Again, values based on calculated efficiencies ε_{calc} are excluded.

The procedure is the same as for the $\langle \Delta\sigma \rangle$ calculation: first, the ratio $y/\mathrm{d}y$ is calculated for each center-of-mass energy for the respective set of proton momentum boundaries (p_{low}, p_{high}):

$$(y/\mathrm{d}y)_i = \left(\frac{N/\varepsilon}{\mathrm{d}(N/\varepsilon)} \right)_i \qquad \text{ratio per } \sqrt{s}_i \tag{3.26}$$

Then, the average of the ratios of each boundary setting is determined by

$$\langle y/\mathrm{d}y \rangle = \frac{1}{12} \sum_{i=1}^{12} (y/\mathrm{d}y)_i \qquad \text{with } \sqrt{s}_1 = 4190,\ \sqrt{s}_2 = 4200,\ \ldots \sqrt{s}_{12} = 4420 \text{ in MeV} \tag{3.27}$$

and is depicted as a solid line in figure 3.22, showing the ratios $y/\mathrm{d}y$ versus $\sqrt{s}$ with and without applied proton momentum selection. The momentum cut leads to higher ratios (figure 3.22b), synonymous with smaller relative errors.

For better comparability, the ranges of the y-axes (with or without applied cut) cover different ranges, but are of the same scale (100 units). When applying the cut, the influence of the size of the data sample on $y/\mathrm{d}y$ becomes apparent: the smaller the size, the worse the yield to error ratio, e.g. $175.7\,\mathrm{pb}^{-1}$ for D4280. Data samples of comparable size (luminosity $\mathcal{L}_{int}$) have similar relative errors, e.g. the relative errors of the data samples D4190, D4200, D4210 and D4220 are similar, as their integrated luminosity is $\mathcal{L} \approx 520\,\mathrm{pb}^{-1}$.

Then, equally as for $\langle \Delta\sigma \rangle$, a momentum range of $[0.0; 0.5]\,\mathrm{GeV}/c$ is scanned using $\langle y/\mathrm{d}y \rangle$ to determine the optimal lower cut-off value p_{low} (figure 3.23). The scan is performed using the same three values of the higher momentum boundary ($p_{high} \in \{1.35, 1.40, 1.45\}\,\mathrm{GeV}/c$). The respective maxima of the three $\langle y/\mathrm{d}y \rangle$ distributions are identified by a fit function, given by:

$$f(x) = (p_0 + p_1\,x + p_2\,x^2) \cdot e^{-\,p_3\,x} + p_4 \qquad \text{with } p_i \in \mathbb{R} \tag{3.28}$$

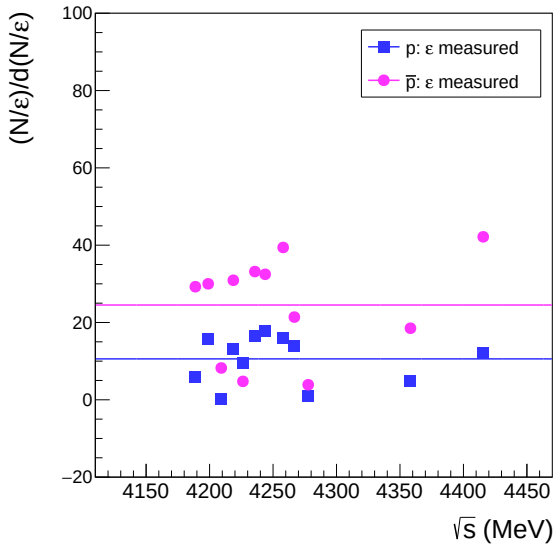

(a) No p_p cut applied.

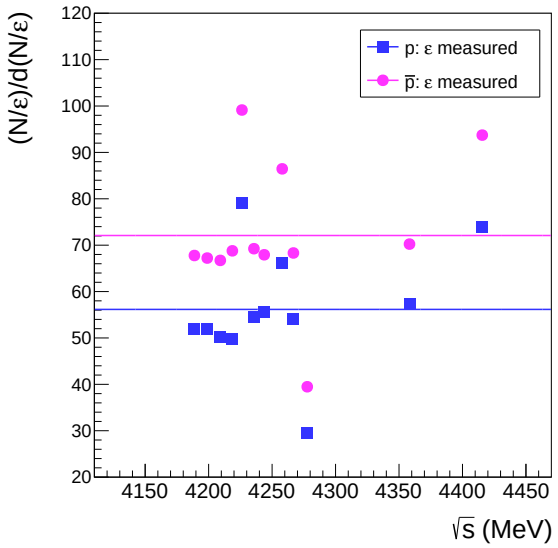

(b) With applied p_p cut.

Figure 3.22: Inverse of the relative error $(y/\mathrm{d}y)$ plotted against $\sqrt{s}$. Attention should be paid to the different scales of the y-axis. A solid line depicts the average of the ratios.

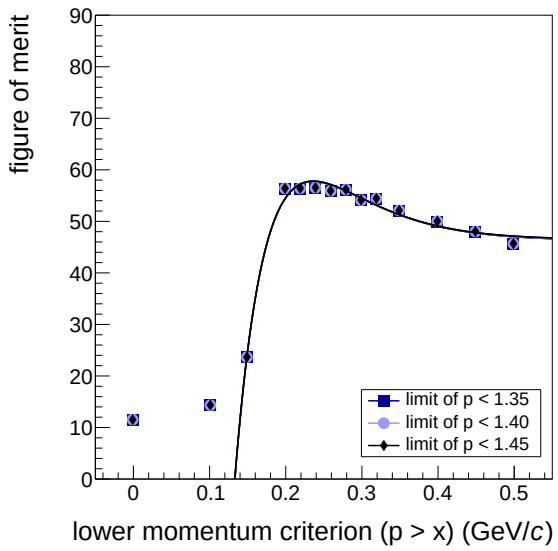

(a) Λ^0 reconstruction mode

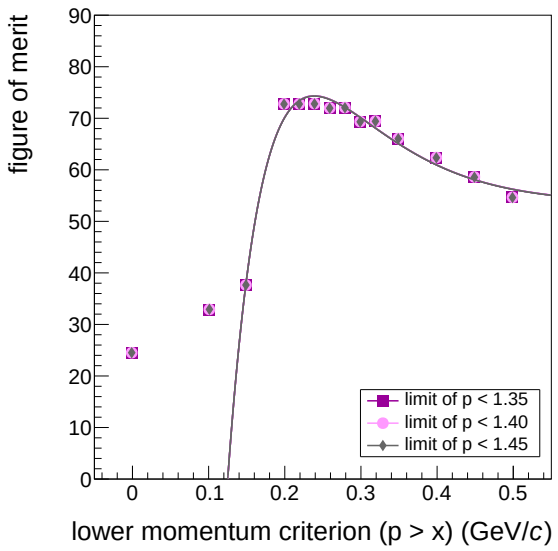

(b) $\bar{\Lambda}^0$ reconstruction mode

Figure 3.23: The three $\langle y/\mathrm{d}y \rangle$ distributions as functions of the lower momentum cut

The x-position of the maximum of the distribution is the momentum cut with the smallest relative error $\mathrm{d}y/y$. Both $\langle y/\mathrm{d}y \rangle$ distributions in figure 3.23 are of compareable shape, but the one for Λ^0 candidates is located below the one for $\bar{\Lambda}^0$ candidates ($\sim$ 15 units). This is synonymous to a higher relative error for the Λ^0 reconstruction, and can be linked to the different backround levels of the invariant mass spectra of the Λ^0 and $\bar{\Lambda}^0$ candidates (figure 3.8). A higher background level leads to a higher relative error.

Combination of Both Figures of Merit: $\mathcal{C}$

The combination of the discussed figures of merit ($\langle\Delta\sigma\rangle$ and $\langle y/\mathrm{d}y\rangle$) gives $\mathcal{C}$:

$$\mathcal{C}_{l,h} = \frac{\langle y/\mathrm{d}y\rangle_{l,h}}{\langle\Delta\sigma\rangle_{l,h}} \qquad \text{with } l \equiv \text{lower, } h \equiv \text{higher cut-off value} \tag{3.29}$$

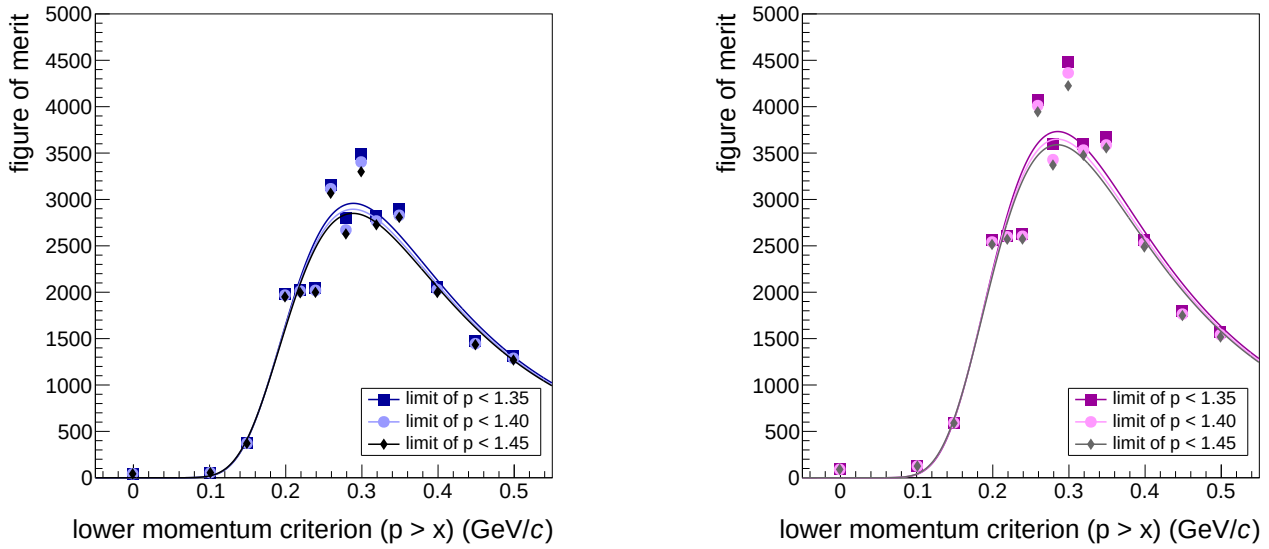

(a) Λ^0 reconstruction mode (b) $\bar{\Lambda}^0$ reconstruction mode

Figure 3.24: The three significance distributions $\mathcal{C}$ as functions of the lower momentum cut.

The x-position of the maximum of each distribution of $\mathcal{C}_{l,h}$ ($\mathcal{C}_{l,1.35}$, $\mathcal{C}_{l,1.40}$ and $\mathcal{C}_{l,1.40}$) results in the best momentum cut-off boundary (figure 3.24). The maxima of the distributions are determined by a landau fit function [115], the equivalent to the complex form:

$$p(x) = \frac{1}{\xi}\frac{1}{\pi}\int_0^\infty e^{-(\lambda+\log t)\cdot t}\sin(\pi t)\,\mathrm{d}t \qquad \text{with } \lambda = \frac{(x-x_0)}{\xi} \quad , \tag{3.30}$$

ξ the width parameter and x_0 is the location parameter, which corresponds to the most probable value and log refers to the natural logarithm. The fit results for the three variations of the higher selection criterion are summarised in table 7:

set values:	determined by the fit (equation 3.30):	
higher boundary of p_x	lower boundary of p_p	lower boundary of $p_{\overline{p}}$
1.35	0.29	0.29
1.40	0.29	0.28
1.45	0.29	0.28

Table 7: The three p_p and $p_{\overline{p}}$ cut pairs resulting from the fit.

The pair (0.28,1.40) GeV/c is identified to be the best: since the significance of the $\bar{\Lambda}^0$ reconstruction is higher (figure 3.23b), the results listed in the third column of table 7 are the initial selection. The mean of these three values is $0.28\overline{3}$, hence the lower boundary value of 0.28 gives the closer selection of 1.40 or 1.45 for the higher boundary (second and third row).

The value of 1.40 is chosen as higher boundary, because the cross-section deviation distribution of the 1.40 boundary shows smaller errors than the one of the 1.45 boundary (figure 3.21), apart from the similarity of their courses. This is based on the increasing error of the reconstruction efficiency per momentum bin (figure 3.18) above approximately 1.40 GeV/c. In addition to the increasing error, the divergence among the efficiency values per bin grows.

3.7. Acceptance Correction

The acceptance correction is necessary besides the efficiency calculation as the angular and momentum cut causes a loss, which is not addressed by the efficiency correction and is determined by counting generator particles of *generator MC* with and without applied cuts. The number of particles with applied momentum and angular cuts is divided by the number of particles without cuts. Additionally the following three *MC truth* criteria must be met simultaneously:

1. one decay product has to be a(n) (anti-)proton
2. the other decay product has to be a charged pion of opposite sign
3. their common particle of origin has to be a neutral Λ ($\bar{\Lambda}$).

The loss caused by the angular cut is presented figure 3.25a, the loss of both in figure 3.25b.

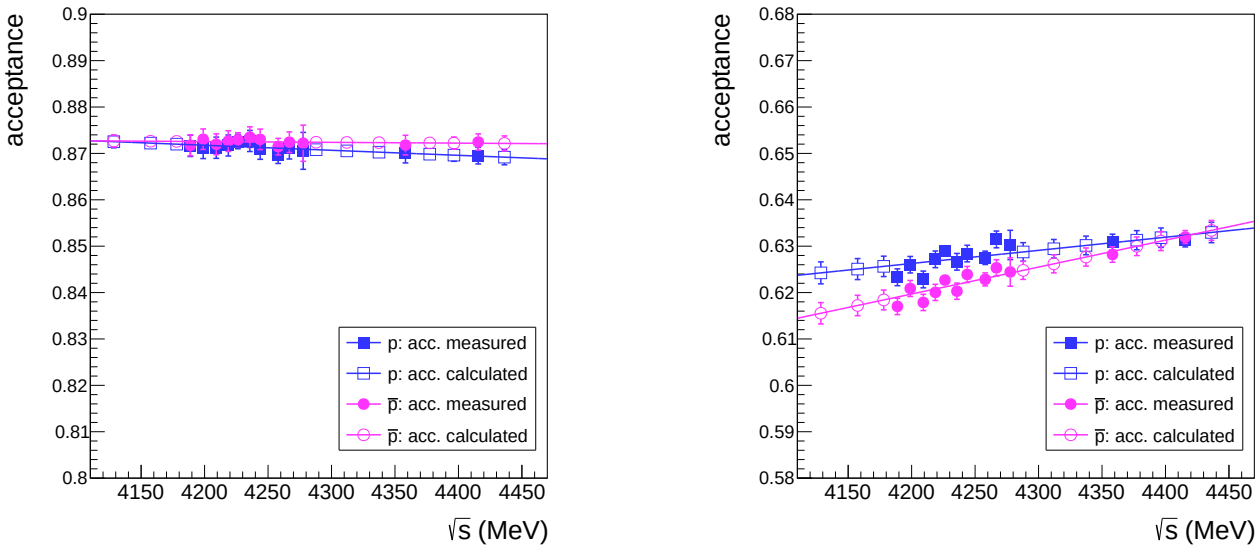

(a) No p_p, but $|\cos(\theta_p)|$ cut applied.

(b) With applied p_p cut.

Figure 3.25: Detector acceptance as a function of the center-of-mass energy $\sqrt{s}$. The y-axes have different scales, but both cover a range of 10% to illustrate the difference in the slopes.

Comparing figure 3.25a with figure 3.25b a dependency on $\sqrt{s}$ is introduced by the momentum cut. Considering figures C.1 and C.2, the choice of the boundary of the lower momentum cut has the more pronounced influence. By increasing the center-of-mass energy, more energy is available for the decay system, so the decay particles can occupy a larger phase space, meaning their momentum distribution is shifted toward higher values. As for higher energies the mean of this distribution is less close to the cut boundary, the amount of rejected particles decreases, hence, the acceptance is higher. The calculation of the acceptance and its error for data samples without existing *generic MC* is realised as for the efficiency. The respective acceptance values

are calculated by the parameters of the linear fit function (as like equation 3.21). The error of the calculated acceptance is determined in same way as described by equation 3.23 and is considered in figure 3.25.

3.8. The Energy Dependent Cross-Section and Resonance

In high energy physics the term *cross-section* means the probability that two particles will collide and react in a specific way. The higher the cross-section, the more likely the specific reaction.

Here, the collision of two leptons (e^+e^-) is analysed. Measuring the center-of-mass energy dependent cross-section might reveal intermediate resonances, appearing as enhancements (bumps/peaks) in the spectrum. Resonances occure at center-of-mass energies at and beyond their specific production threshold. They are considered to have a constant mass and defined quantum numbers such as angular momentum [116]. The short lifetime of a resonance inhibits a direct measurement as they decay before reaching the detector. In contrast to the calculation of the invariant mass, where all decay particles of a short-lived particle must be reconstructed, the measurement of the energy dependent cross-section $\sigma(\sqrt{s})$ has the benefit, that not all decay particles must be known. Measuring $\sigma(\sqrt{s})$ of one decay particle of a specific decay channel in a so-called inclusive measurement allows to determine if a resonance contributes to this channel.

By determining the position of the maximum (E_0) and the width at half maximum (Γ) of the peak, described e.g. by a Breit-Wigner fit function, the mass[1] ($M = E_0$) and the lifetime ($\tau = 1/\Gamma$) of the resonance can be accessed (figure 3.26).

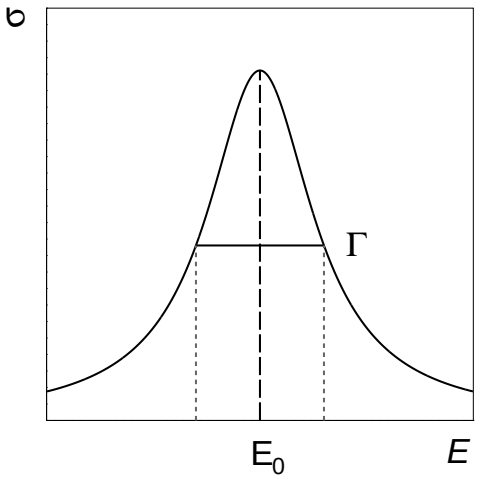

Figure 3.26: A resonance described by a Breit-Wigner function as an illustration.

The shorter the lifetime τ, the broader the peak of a resonance (larger Γ). Under the condition that the lifetime of the resonance is not too short ($\Gamma \ll E_0$), the cross-section of the reaction of two particles close to the resonance energy E_0 can described by the Breit-Wigner formula [116]:

[1] Basically, the position of the peak is not the pole mass, an approximation of the intuitive physical mass of a particle, and can be shifted due to interferences.

$$\sigma(E) = \frac{\pi\lambda^2(2J+1)}{(2s_a+1)(2s_b+1)} \cdot \frac{\Gamma^2}{(E-E_0)^2+\Gamma^2/4} \tag{3.31}$$

with the reduced wave length λ in the center-of-mass system. In an inelastic scattering, such as the annihilation reaction of a leptonic pair e^+e^-, the cross-section depends on the the initial Γ_i and the final Γ_f width of the in- and outcoming channel and also of the sum of all partial widths of all possible outcoming channels Γ_{total}:

$$\sigma(E) = \frac{3\pi\lambda^2}{4} \cdot \frac{\Gamma_i\Gamma_f}{(E-E_0)^2+{\Gamma_{total}}^2/4} \tag{3.32}$$

simplified with the spins of the leptons are $s_a = s_b = 1/2$ and $J = 1$ for the virtual photon. By applying a Breit-Wigner fit function to a measured $\sigma(\sqrt{s})$ distribution, the mass and the lifetime of a resonance become accessible.

3.8.1. Experimental Cross-Section

In high energy physics experiments, such as the BESIII, data is accumulated over a long period of time (e.g. months) for the purpose of a good significance for rare events. An event is one particular decay of interest (section 3.2). The total number of events N of a specific reaction is proportional to the time-integrated luminosity $\mathcal{L}_{int}$. The observed cross-section σ^{obs} is given by

$$\sigma^{obs}(E) = \frac{N}{\mathcal{L}_{int} \cdot \varepsilon \cdot \mathrm{A} \cdot \mathcal{B}_i} \tag{3.33}$$

with the previously discussed reconstruction efficiency (ε), the acceptance (A) and the respective branching ratio(s) ($\mathcal{B}_i$) of the analysed decay channel(s). The time integral of the luminosity $\mathcal{L}_{int}$ depends on the beam properties of the accelerator and is given by:

$$\mathcal{L}_{int} = \int \mathrm{d}t\, \mathcal{L} \qquad \text{with } \mathcal{L} = \frac{N_1 N_2 f}{4\pi\sigma_x\sigma_y} \tag{3.34}$$

with the numbers of particles per bunch N_1, N_2, the frequency f of bunch collisions of the accelerator and the spatial dimensions σ_x and σ_y of the bunch.

Considering the ISR correction factor $(1+\delta_{ISR})$ (section 3.8.2), the Born cross-section σ^{Born} can be derived from the observed cross-section. The determination of $(1+\delta_{ISR})$ uses the relation of the observed cross-section to the Born cross-section via the integral[1] [117]:

$$\sigma^{obs}(E) = \int_0^{1-m_{min}^2/E} W(E,x) \cdot \sigma^{Born}(E) \cdot (E(1-x))\,\mathrm{dx} \tag{3.35}$$

where $E = 4E_0^2$, with the beam energy E_0, x is an effective fraction of E_0 carried by photons emitted from the initial state and m_{min} is the minimal possible invariant mass of the final hadrons. The radiator function $W(E,x)$ (figure 3.27) considers higher-order QED contributions.

[1] Unlike in [117] the detection efficiency $\varepsilon(E,x)$ has been omitted for a better overview.

Equation 3.35 can be simplified to

$$\sigma^{obs}(E) = \sigma^{Born}(E) \cdot (1 - \delta(E)) \qquad \rightarrow \qquad \sigma^{Born}(E) = \frac{\sigma^{obs}(E)}{(1 - \delta(E))} \tag{3.36}$$

where $(1 - \delta(E))$ is the radiative correction factor.

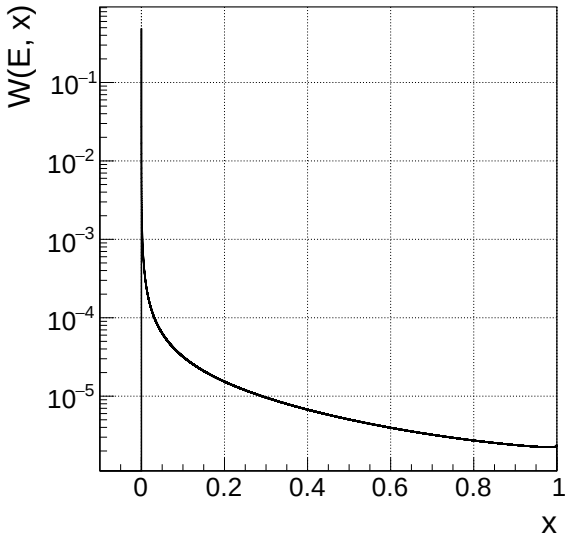

Figure 3.27: Radiator function at $E = 4260\,\text{MeV}$. The course of the curve does not alter significantly for different center-of-mass energies.

It is necessary to know the energy dependence of the Born cross-section from $E(1 - x_0)$, in other words from the point of measurement at the energy E until the radiator function reaches $x = 1$ towards lower center-of-mass energies. Consequently, measured bare cross-sections at a given center-of-mass energy are (without ISR correction) an admixture of cross-sections also at smaller energies. The Born cross-section is given by

$$\sigma^{Born}(E) = \frac{N}{\mathcal{L}_{int} \cdot \varepsilon \cdot \mathrm{A} \cdot (1 + \delta_{ISR}) \cdot \mathcal{B}_i} \,. \tag{3.37}$$

Additionally, the vacuum polarisation correction factor $(1/|1-\Pi(s)|^2)$ [118] has to be considered. Vacuum polarisation means the production of virtual e^+e^- pairs by a background electromagnetic field. These charged pairs act as an electric dipole and counteract other present electric fields partially, e.g., the electromagnetic field around an electron, and hence this field will be weaker than expected if the vacuum were completely empty. Considering this correction, the dressed cross-section σ^{dress} is given by

$$\sigma^{dress}(E) = \frac{N}{\mathcal{L}_{int} \cdot \varepsilon \cdot \mathrm{A} \cdot (1 + \delta_{ISR}) \cdot \frac{1}{|1-\Pi(s)|^2} \cdot \mathcal{B}_i} \,. \tag{3.38}$$

Table 8 lists the $1/|1 - \Pi(s)|^2$ values used in this analysis, based on values given in [119].

$\sqrt{s}$ (MeV)	$\frac{1}{\lvert 1-\Pi(s)\rvert^2}$	$\sqrt{s}$ (MeV)	$\frac{1}{\lvert 1-\Pi(s)\rvert^2}$	$\sqrt{s}$ (MeV)	$\frac{1}{\lvert 1-\Pi(s)\rvert^2}$
4130	1.052	4230	1.056	4315	1.052
4160	1.053	4237	1.056	4340	1.051
4180	1.054	4246	1.056	4360	1.051
4190	1.056	4260	1.054	4380	1.051
4200	1.056	4270	1.053	4400	1.051
4210	1.057	4280	1.053	4420	1.052
4220	1.056	4290	1.053	4440	1.054

Table 8: The vacuum polarisation correction factors used in this analysis [119].

3.8.2. Initial State Radiation (ISR)

Initial State Radiation (ISR) arises in e^+e^- annihilations and causes an energy loss as a photon might be emitted by one or both of the leptons before the collision. This energy loss effectively leads to a lower center-of-mass energy. The correction factors $(1+\delta_{ISR})$ for each of the 21 center-of-mass energies of the analysed data samples are computed in an iterative procedure as discussed in [120]. Convergence is assumed when the change of the correction factor reaches a minimum.

Initially, the measured cross-section[1] (equation 5.1) for each data set is taken as an input (figure 3.28), and the application of the final correction factor on the measured cross-section gives the dressed cross-section (equations 3.38). The center-of-mass energy range of the calculation of σ^{calc} begins at 2.23 GeV, as this energy corresponds to the production threshold of a $\Lambda^0\bar{\Lambda}^0$ pair, the system of least mass including a Λ^0.

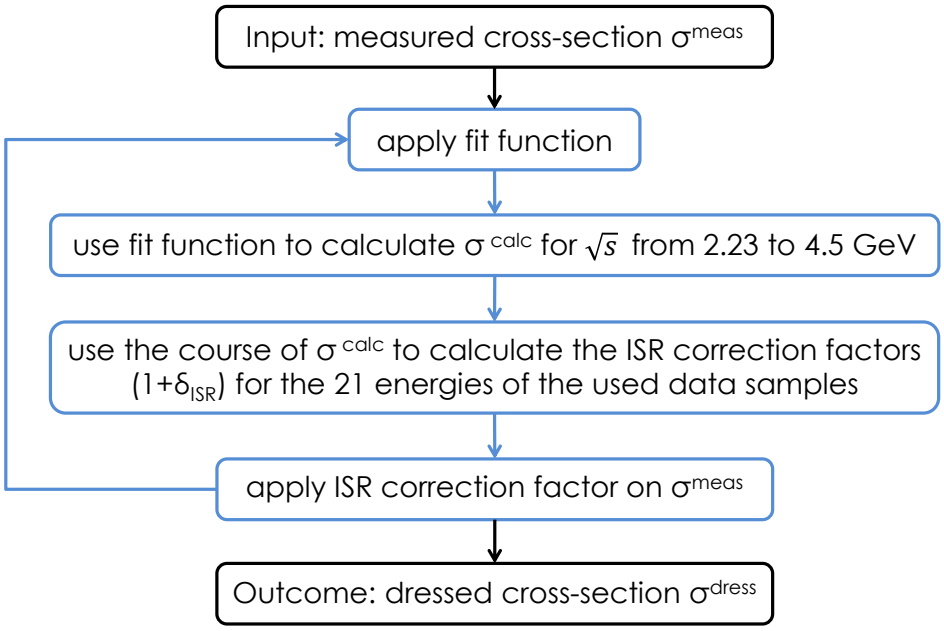

Figure 3.28: Scheme of the ISR correction factor determination.

[1]The measured cross-section is the observed cross-section with applied vacuum polarisation correction factor.

4. Systematic Uncertainties

The contributing systematic uncertainties to the measured and to the dressed cross-section (section 5.1 and 5.2) are discussed in this section.

4.1. Luminosity Measurement Uncertainty

The time-integrated luminosity is measured by analysing events produced by the large-angle Bhabha scattering process ($e^+e^- \to e^+e^-$) [121]. At all center-of-mass energy points between 3.81 and 4.6 GeV the statistical accuracy is better than 0.1%. The total systematic uncertainty is determined to be less than 1% for all data samples and had been cross-checked with di-gamma events.

4.2. Tracking and PID Uncertainty

The systematic uncertainties and efficiencies of the tracking and the PID are essential in this inclusive analysis since the event selection is based only on three criteria: PID, the momentum and the angular cuts; the latter two are affected by tracking errors.

The estimation of the systematic uncertainties in this analysis is based on a detailed study within the BESIII collaboration in 2020 [122, 123], with regard to the initial study in 2016 [124]. This study presents the systematic uncertainties of tracking and PID through the decay $J/\psi \to p\bar{p}\pi^+\pi^-$ by two quantities: the (transverse) momentum and the $cos(\theta)$ of the (anti-)protons and charged pions. About 10 billion J/ψ events, accumulated in 2009, 2012, 2018 and 2019 respectively, have been analysed. The systematic uncertainty of each particle species $(p, \overline{p}, \pi^+, \pi^-)$ of each year is presented as a two-dimensional look-up table: transverse momentum (p_t) versus $cos(\theta)$ for the tracking uncertainty and momentum (p) versus $cos(\theta)$ for the PID uncertainty. Some uncertainty values for high momenta are not given in these tables due to "low statistic and poor fitting" [122], so errors for momenta higher than 1.0 GeV/c for (anti-)protons and 0.7 GeV/c for pions have to be extrapolated.

The systematic uncertainty of the Λ^0 ($\bar{\Lambda}^0$) reconstruction in this analysis is calculated using look-up tables (figure 4.1) which are extractions of the two-dimensional tables of the study. Extraction means: among the four data samples (2009−2019) of the study the largest error per $(\cos(\theta), p)$ bin is selected in each case.

Uncertainty values for (anti-)protons with momenta higher than 1 GeV/c (0.7 GeV/c for pions) are determined as follows: the largest error is selected among the last three momentum bins before the boundary. For example in figure 4.1, at $\cos(\theta_p) \in [0.0; 0.2]$, the largest error is 0.28 among the last three entries of 0.28, 0.24 and 0.20 before the boundary at 1 GeV/c.

Therefore 0.28 is chosen as systematic tracking uncertainty for (anti-)protons with momenta higher than 1 GeV/c.

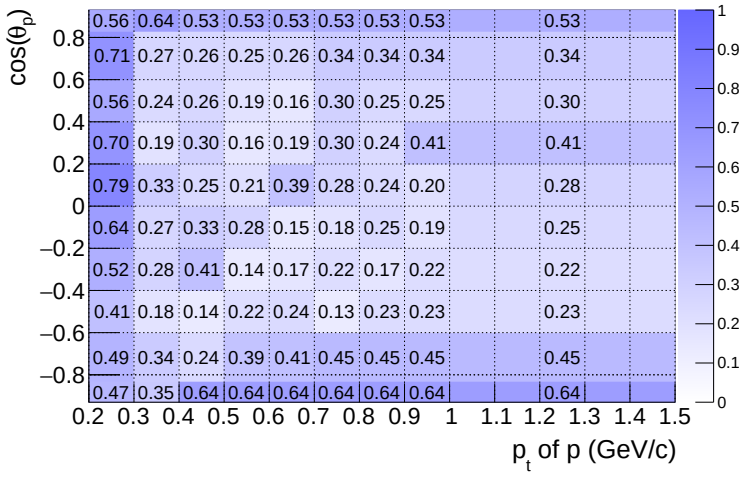

Figure 4.1: Tracking uncertainty[1] (δ_i) of p (in %) per $(\cos(\theta_p), p_t)$ bin.

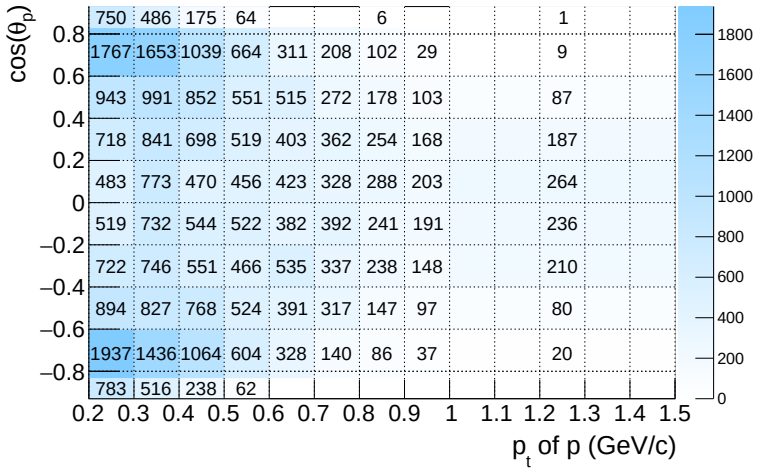

Figure 4.2: Sideband-subtracted multiplicity of reconstructed p of D4230 with applied selections (table 5) and $N_{total} = 8016$.

Figure 4.2 shows the sideband-subtracted distribution in polar angle and transverse momentum of reconstructed protons of Λ^0 candidates. A sideband subtraction reduces background events. Possible negative values appearing at the margins of the distribution are ignored for the calculation. The multiplicity distribution is used to determine the tracking uncertainty δ_{track} per center-of-mass energy: the tracking uncertainty per bin δ_i (figure 4.1) is weighted by the multiplicity per bin N_i (figure 4.2), using:

$$\delta_{track}(\sqrt{s}) = \frac{1}{N_{total}} \sum\nolimits_i \delta_i \cdot N_i \quad \text{with } N_{total} = \sum\nolimits_i N_i \tag{4.1}$$

Therefore, the contribution to $\delta_{track}(\sqrt{s})$ is more pronounced for bins with high multiplicities. The tracking uncertainty for the other decay products and also the PID uncertainty is received in the same way. The individual uncertainties of all four species are depicted in section D.

[1]The corresponding histograms for the PID uncertainty and for the other analysed particles $\overline{p}, \pi^-$ and π^+ can be found on page 77 and following.

The total tracking and PID error (δ_{total,Λ^0}) for the reconstruction of a Λ^0 (or the charged conjugated reconstruction of $\bar{\Lambda}^0$) is the combination of the tracking and PID uncertainties for p and π^- following equation 4.2.

$$\delta_{total,\Lambda^0}(\sqrt{s}) = \sqrt{(\delta_{track,p} + \delta_{track,\pi^-})^2 + (\delta_{PID,p} + \delta_{PID,\pi^-})^2} \tag{4.2}$$

Correlated errors are added linearly, not correlated errors by their squares. With regard to the center-of-mass energy the combined error is constant to some extent for both reconstruction modes as shown in figure 4.3.

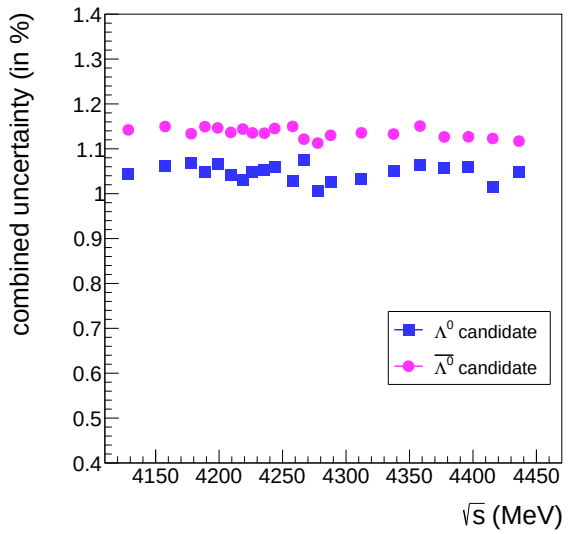

Figure 4.3: Combined uncertainty in tracking and PID for Λ^0 and $\bar{\Lambda}^0$ candidates.

4.3. ISR Correction Uncertainty

The systematic uncertainty of the ISR correction factor is based on the unknown shape of the continuum of the measured inclusive cross-section. Since no appropriate[1] data samples for center-of-mass energies lower than 4 GeV had been available at the time of this work, the shape of the continuum in the analysed energy range is approximated at a very basic level with a linear function (figure 5.2). This applied fit function on the measured cross-section is used to calculate the ISR correction factor in an iterative procedure (section 3.8.2). The energy dependent magnitude of the continuum affects the measured cross-section, since the initial state radiation can be described by a radiator function, an ascending power law (figure 3.27). In other words, the measured bare cross-section at a given center-of-mass energy is an admixture of cross-sections also at lower energies.

To determine the impact of the shape of the continuum on the ISR corretion factor, the iterative procedure is performed twice, once with a constant (the continuum is assumed to be a plateau) and then again with a continuum having a slope. The relative difference of the final correction factors of both iterations is determined as the systematic uncertainty resulting from the unknown shape of the phase space.

[1] The time-integrated luminosity has to be higher than 100 pb^{-1} for a sufficient significance.

4.4. The Applied Systemtic Uncertainties

The respective systematic uncertainties introduced above are listed in table 9 with the total systematic uncertainty $\delta_{total} = \sqrt{\delta_{trk}^2 + \delta_{PID}^2 + \delta_{\mathcal{L}}^2 + \delta_{ISR}^2}$.

The uncertainty of the measurement of the luminosity $\delta_{\mathcal{L}}$ has been neglected in the fit of the energy dependent cross-section, since $\delta_{\mathcal{L}}$ is totally correlated for all data sets. It would result in a common shift of all data points, and thus should not contribute to the χ^2 of the fit.

The reduced systematic uncertainty $\delta_m = \sqrt{\delta_{trk}^2 + \delta_{PID}^2}$ is applied to the measured cross-section, and $\delta_d = \sqrt{\delta_{trk}^2 + \delta_{PID}^2 + \delta_{ISR}^2}$ to the dressed cross-section.

	$e^+e^- \to \Lambda^0 X$							$e^+e^- \to \bar{\Lambda}^0 X$						
$\sqrt{s}$ (MeV)	δ_{trk} (%)	δ_{PID} (%)	$\delta_{\mathcal{L}}$ (%)	δ_{ISR} (%)	δ_{total} (%)	δ_m (%)	δ_d (%)	δ_{trk} (%)	δ_{PID} (%)	$\delta_{\mathcal{L}}$ (%)	δ_{ISR} (%)	δ_{total} (%)	δ_m (%)	δ_d (%)
4128.48	0.80	0.67	1	0.11	1.45	1.04	1.05	0.91	0.69	1	1.73	2.30	1.14	2.07
4157.44	0.80	0.70	1	0.10	1.46	1.06	1.07	0.92	0.69	1	1.74	2.31	1.15	2.08
4178.00	0.79	0.68	1	0.11	1.45	1.05	1.05	0.91	0.67	1	1.80	2.35	1.13	2.12
4188.80	0.80	0.71	1	0.10	1.47	1.07	1.07	0.92	0.69	1	1.86	2.41	1.15	2.19
4198.90	0.79	0.68	1	0.11	1.45	1.04	1.05	0.92	0.69	1	1.95	2.48	1.15	2.26
4209.20	0.78	0.67	1	0.10	1.44	1.03	1.04	0.92	0.67	1	1.73	2.30	1.14	2.07
4218.70	0.78	0.70	1	0.11	1.45	1.05	1.05	0.92	0.68	1	1.73	2.31	1.14	2.08
4226.26	0.79	0.69	1	0.09	1.46	1.05	1.06	0.91	0.68	1	1.73	2.30	1.14	2.07
4235.70	0.79	0.71	1	0.10	1.46	1.06	1.07	0.91	0.67	1	1.73	2.30	1.13	2.07
4243.80	0.78	0.67	1	0.10	1.44	1.03	1.03	0.92	0.69	1	1.74	2.31	1.15	2.08
4257.97	0.80	0.72	1	0.11	1.47	1.07	1.08	0.91	0.70	1	1.76	2.32	1.15	2.10
4266.80	0.78	0.64	1	0.11	1.42	1.01	1.01	0.91	0.65	1	1.83	2.37	1.12	2.15
4277.70	0.79	0.66	1	0.10	1.44	1.03	1.03	0.90	0.65	1	1.87	2.40	1.11	2.18
4287.88	0.78	0.67	1	0.11	1.44	1.03	1.04	0.91	0.67	1	1.78	2.33	1.13	2.11
4312.05	0.79	0.70	1	0.12	1.46	1.05	1.06	0.92	0.67	1	1.75	2.32	1.14	2.09
4337.39	0.79	0.71	1	0.09	1.46	1.06	1.07	0.91	0.67	1	1.91	2.43	1.13	2.22
4358.26	0.79	0.70	1	0.08	1.46	1.06	1.06	0.91	0.70	1	1.97	2.49	1.15	2.28
4377.37	0.80	0.70	1	0.11	1.46	1.06	1.06	0.91	0.66	1	1.93	2.45	1.13	2.24
4396.45	0.77	0.66	1	0.09	1.43	1.02	1.02	0.91	0.66	1	2.04	2.54	1.13	2.33
4415.58	0.78	0.70	1	0.12	1.45	1.05	1.05	0.90	0.67	1	2.06	2.55	1.12	2.35
4436.24	0.79	0.72	1	0.15	1.47	1.07	1.08	0.91	0.65	1	2.24	2.69	1.12	2.50

Table 9: Systematic uncertainty of tracking, PID, luminosity and of the ISR correction. δ^m is the systematic uncertainty of the mesaured cross-section σ^m, and δ^d is the systematic uncertainty of the dressed cross-section σ^d.

5. Analysis Results

5.1. The Measured Energy-Dependent Cross-Section

The measured energy-dependent cross-section $\sigma^m(\sqrt{s})$ is calculated by

$$\sigma^m(\sqrt{s}) = \frac{N_{sig}}{\mathcal{L}_{int} \cdot \varepsilon \cdot \mathrm{A} \cdot \frac{1}{|1-\Pi(s)|^2} \cdot \mathcal{B}(\Lambda^0 \to p\pi^-)} \tag{5.1}$$

with the time-integrated luminosity $\mathcal{L}_{int}$, the branching ratio $\mathcal{B}(\Lambda^0 \to p\pi^-) = 0.639 \pm 0.005$, the detection acceptance A and the vacuum polarisation correction factor $1/|1 - \Pi\,(s)\,|^2$. The cross-section distributions of the inclusive Λ^0 and $\bar{\Lambda}^0$ reconstructions are shown in the figures 5.1 and 5.2. Their respective values and the other quantities of equation 5.1 are listed in table 10, except for the vacuum polarisation correction factor (table 8).

The radiative correction factor $(1 + \delta_{ISR})$ has been omitted in equation 5.1 in comparison to the dressed cross-section (equation 3.38). To calculate $(1 + \delta_{ISR})$ (section 3.8.1), it is necessary to know the energy dependence of the cross-section. Since the shape of the continuum towards lower energies until the $\Lambda\bar{\Lambda}$ threshold at 2.23 GeV is unknown, the calculation of the radiation correction factors is associated with an uncertainty depending on the fit model of the phase space shape. To disentangle this uncertainty, the measured cross-section is discussed at first and then the dressed cross-section.

5.1.1. The Individual and the Simultaneuos Fit of the Measured Cross-Sections

Initially, an individual fit function is applied on each cross-section distribution, $\sigma^m_{\Lambda^0}(\sqrt{s})$ and $\sigma^m_{\bar{\Lambda}^0}(\sqrt{s})$, given by

$$f(\sqrt{s}) = BW_1(\sqrt{s}) + BW_2(\sqrt{s}) + BW_3(\sqrt{s}) + p_0 + p_1 \cdot \sqrt{s} \tag{5.2}$$

with $p_i \in \mathbb{R}$ and three incoherent non-relativistic Breit-Wigner functions BW_i

$$BW_i(s; m_i, \Gamma_i, I_i) = \frac{I_i \cdot \Gamma_i^2}{4 \cdot (\sqrt{s} - m_i)^2 + \Gamma_i^2} \tag{5.3}$$

where I_i, m_i and Γ_i are the intensity, the position and the width of the i-th resonance, and $\sqrt{s}$ is the center-of-mass energy. The intensity is independent from the width by the normalisation of the $BW_i(\sqrt{s})$. The first Breit-Wigner function $BW_1(\sqrt{s})$ represents the resonance at around 4230 MeV, $BW_2(\sqrt{s})$ represents the second resonance at 4360 MeV and $BW_3(\sqrt{s})$ represents the third resonance at 4415 MeV. A polynom of first order is used as an estimate of the shape of the continuum in this energy range.

Secondly, a simultaneous fit is applied on both cross-section distributions (figure 5.2) to increase the number of measurements in relation to the number of parameters of the fit function, especially for the second and third resonance. The resonance parameters (I_i, m_i and Γ_i) are common for both spectra, while the slopes and intensities of each continuum distribution are independent.

The statitistical significance Z (section 5.3) of the three observed resonances ($\mathcal{R}_1$, $\mathcal{R}_2$ and $\mathcal{R}_3$) is determined using the simultaneous fit function, and $Z > 5\sigma$ for all three (table 15).

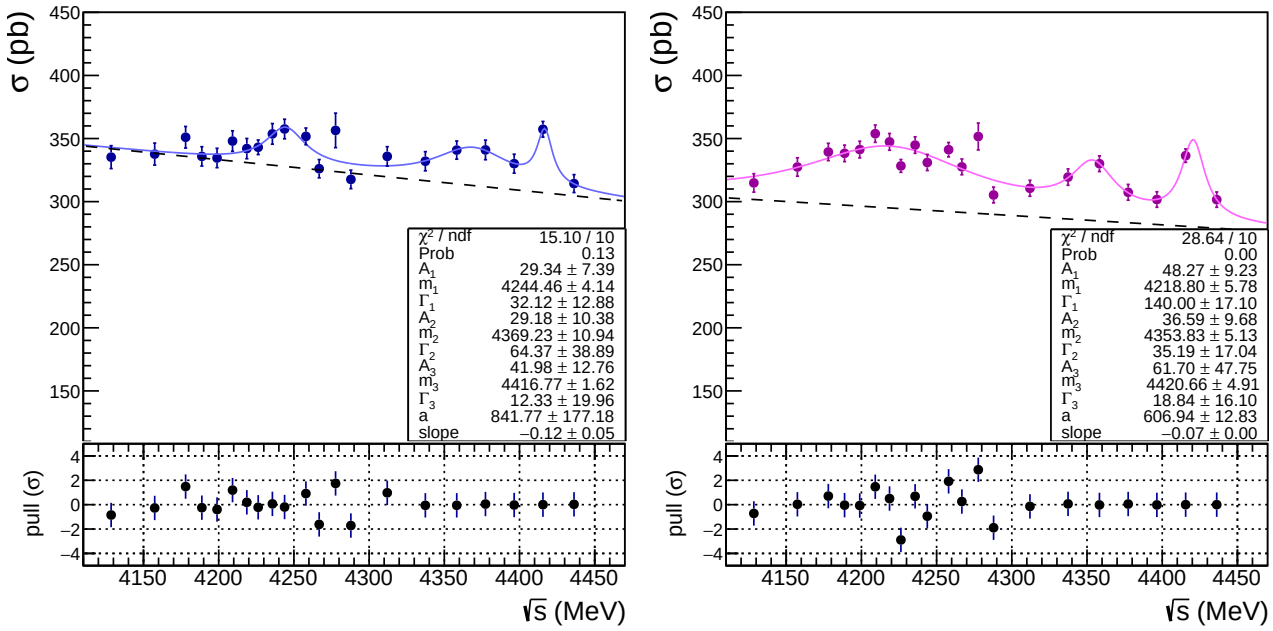

Figure 5.1: The measured inclusive cross-sections $\sigma^m_{\Lambda^0}[\sigma(e^+e^- \to \Lambda^0 X)]$ (left, blue) and $\sigma^m_{\bar{\Lambda}^0}[\sigma(e^+e^- \to \bar{\Lambda}^0 X)]$ with individual fit functions, shown as solid lines. The dashed gray lines correspond to the continuum distributions, respectively.

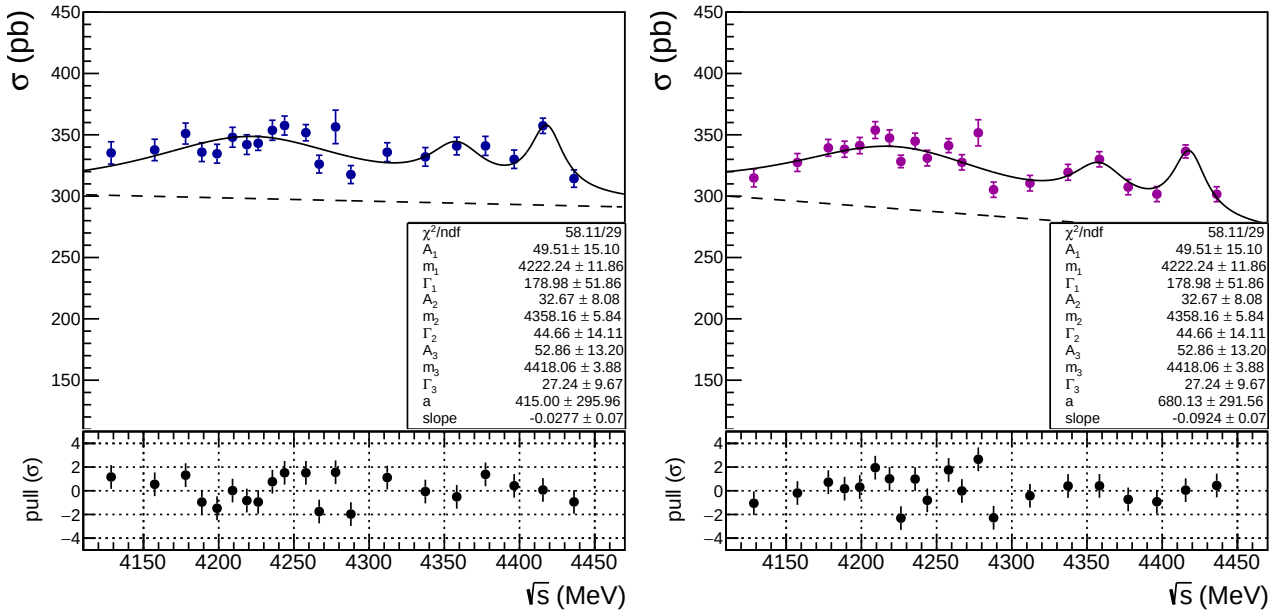

Figure 5.2: The measured inclusive cross-section $\sigma^m_{\Lambda^0}$ $[\sigma(e^+e^- \to \Lambda^0 X)]$ (left, blue) and $\sigma^m_{\bar{\Lambda}^0}$ $[\sigma(e^+e^- \to \bar{\Lambda}^0 X)]$ with simultaneous fit function, shown as solid line. The dashed gray lines correspond to the continuum distributions, respectively.

$\sqrt{s}$ (MeV)	$\mathcal{L}_{int}$ (pb^{-1})	N_{sig}	ε (%)	A (%)	$\sigma^m_{\Lambda^0} \pm \delta_{stat} \pm \delta_{sys}$ (pb)
4128.48	401.5 ± 0.10 ± 1.00	13657 ± 284.1	□22.72 ± 0.52	62.42 ± 0.11	335.26 ± 8.37 ± 3.50
4157.44	408.7 ± 0.10 ± 1.00	14035 ± 256.6	□22.74 ± 0.49	62.50 ± 0.09	337.66 ± 7.96 ± 3.58
4178.00	3189.0 ± 0.20 ± 31.90	113933 ± 758.4	□22.76 ± 0.49	62.56 ± 0.08	351.01 ± 7.68 ± 3.75
4188.80	526.7 ± 0.10 ± 2.20	17897 ± 297.1	22.83 ± 0.45	62.33 ± 0.18	335.86 ± 6.79 ± 3.52
4198.90	526.0 ± 0.10 ± 2.50	17846 ± 298.3	22.49 ± 0.45	62.60 ± 0.18	334.59 ± 6.79 ± 3.57
4209.20	517.1 ± 0.10 ± 1.80	17533 ± 306.8	21.95 ± 0.45	62.28 ± 0.18	348.00 ± 7.26 ± 3.62
4218.70	514.6 ± 0.10 ± 1.80	17919 ± 319.7	22.58 ± 0.47	62.71 ± 0.18	342.02 ± 7.20 ± 3.52
4226.26	1100.9 ± 0.13 ± 7.29	39398 ± 434.2	23.40 ± 0.30	62.90 ± 0.12	343.08 ± 4.51 ± 3.59
4235.70	530.3 ± 0.10 ± 2.40	18947 ± 300.3	22.62 ± 0.46	62.66 ± 0.18	353.69 ± 7.27 ± 3.73
4243.80	538.1 ± 0.10 ± 2.70	19752 ± 304.5	22.76 ± 0.42	62.84 ± 0.18	357.55 ± 6.77 ± 3.79
4257.97	828.4 ± 0.10 ± 5.50	30284 ± 403.4	23.30 ± 0.36	62.74 ± 0.14	351.71 ± 5.54 ± 3.62
4266.80	531.1 ± 0.10 ± 3.10	17482 ± 281.7	22.49 ± 0.43	63.14 ± 0.18	326.10 ± 6.33 ± 3.50
4277.70	175.7 ± 0.10 ± 1.00	5941 ± 174.2	21.32 ± 0.77	63.02 ± 0.32	356.45 ± 13.18 ± 3.59
4287.88	502.4 ± 0.10 ± 1.00	16341 ± 296.8	□22.83 ± 0.43	62.87 ± 0.05	317.60 ± 6.56 ± 3.26
4312.05	501.2 ± 0.10 ± 1.00	17167 ± 301.9	□22.84 ± 0.42	62.94 ± 0.06	335.85 ± 6.85 ± 3.47
4337.39	505.0 ± 0.10 ± 1.00	17089 ± 280.8	□22.86 ± 0.42	63.01 ± 0.07	332.01 ± 6.73 ± 3.49
4358.26	543.9 ± 0.10 ± 3.60	19487 ± 299.1	23.51 ± 0.42	63.08 ± 0.17	340.85 ± 6.23 ± 3.63
4377.37	522.7 ± 0.10 ± 1.00	18276 ± 292.2	□22.89 ± 0.42	63.12 ± 0.09	340.98 ± 6.88 ± 3.60
4396.45	507.8 ± 0.10 ± 1.00	17384 ± 299.4	□22.90 ± 0.42	63.18 ± 0.11	330.09 ± 6.64 ± 3.50
4415.58	1090.7 ± 0.13 ± 7.21	39488 ± 457.7	22.66 ± 0.32	63.12 ± 0.14	357.34 ± 5.05 ± 3.63
4436.24	569.9 ± 0.10 ± 1.00	18564 ± 303.2	□22.92 ± 0.42	63.29 ± 0.13	314.31 ± 6.28 ± 3.29

(a) The measured inclusive cross-section $\sigma^m_{\Lambda^0}$ $[\sigma(e^+e^- \to \Lambda^0 X)]$.

$\sqrt{s}$ (MeV)	$\mathcal{L}_{int}$ (pb^{-1})	N_{sig}	ε (%)	A (%)	$\sigma^m_{\bar{\Lambda}^0} \pm \delta_{stat} \pm \delta_{sys}$ (pb)
4128.48	401.5 ± 0.10 ± 1.00	11291 ± 160.8	□20.77 ± 0.36	61.55 ± 0.10	314.83 ± 6.35 ± 3.60
4157.44	408.7 ± 0.10 ± 1.00	12070 ± 163.5	□20.80 ± 0.34	61.72 ± 0.09	327.44 ± 6.25 ± 3.76
4178.00	3189.0 ± 0.20 ± 31.90	97722 ± 466.5	□20.83 ± 0.34	61.84 ± 0.07	339.36 ± 5.72 ± 3.85
4188.80	526.7 ± 0.10 ± 2.20	16202 ± 188.7	20.89 ± 0.31	62.09 ± 0.17	338.25 ± 5.27 ± 3.89
4198.90	526.0 ± 0.10 ± 2.50	15960 ± 189.4	20.43 ± 0.31	61.79 ± 0.18	341.25 ± 5.36 ± 3.91
4209.20	517.1 ± 0.10 ± 1.80	15714 ± 186.8	19.85 ± 0.30	62.00 ± 0.17	353.84 ± 5.58 ± 4.02
4218.70	514.6 ± 0.10 ± 1.80	16189 ± 186.6	20.73 ± 0.31	62.27 ± 0.12	347.36 ± 5.34 ± 3.97
4226.26	1100.9 ± 0.13 ± 7.29	34055 ± 279.1	21.66 ± 0.22	62.03 ± 0.17	328.30 ± 3.46 ± 3.73
4235.70	530.3 ± 0.10 ± 2.40	16699 ± 189.8	21.01 ± 0.31	62.39 ± 0.17	344.82 ± 5.26 ± 3.91
4243.80	538.1 ± 0.10 ± 2.70	16173 ± 190.3	20.74 ± 0.31	62.28 ± 0.14	331.01 ± 5.15 ± 3.79
4257.97	828.4 ± 0.10 ± 5.50	26154 ± 241.1	21.25 ± 0.25	62.53 ± 0.18	341.17 ± 4.13 ± 3.92
4266.80	531.1 ± 0.10 ± 3.10	16002 ± 188.5	20.94 ± 0.31	62.44 ± 0.31	327.56 ± 5.06 ± 3.67
4277.70	175.7 ± 0.10 ± 1.00	5389 ± 106.6	19.94 ± 0.54	62.48 ± 0.05	351.62 ± 9.93 ± 3.91
4287.88	502.4 ± 0.10 ± 1.00	13980 ± 178.3	□20.96 ± 0.30	62.62 ± 0.06	305.26 ± 5.22 ± 3.45
4312.05	501.2 ± 0.10 ± 1.00	14329 ± 178.9	□20.99 ± 0.30	62.77 ± 0.07	310.58 ± 5.28 ± 3.53
4337.39	505.0 ± 0.10 ± 1.00	14746 ± 180.4	□21.02 ± 0.30	62.82 ± 0.17	319.43 ± 5.39 ± 3.62
4358.26	543.9 ± 0.10 ± 3.60	16789 ± 194.8	21.33 ± 0.31	63.00 ± 0.09	330.05 ± 4.93 ± 3.80
4377.37	522.7 ± 0.10 ± 1.00	14921 ± 184.9	□21.07 ± 0.30	63.11 ± 0.10	307.38 ± 5.21 ± 3.46
4396.45	507.8 ± 0.10 ± 1.00	14241 ± 178.9	□21.10 ± 0.30	63.20 ± 0.14	301.68 ± 5.12 ± 3.40
4415.58	1090.7 ± 0.13 ± 7.21	33842 ± 279.2	20.94 ± 0.23	63.34 ± 0.13	336.43 ± 3.77 ± 3.78
4436.24	569.9 ± 0.10 ± 1.00	16021 ± 191.1	□21.15 ± 0.30	61.70 ± 0.18	301.58 ± 5.07 ± 3.37

(b) The measured inclusive cross-section $\sigma^m_{\bar{\Lambda}^0}$ $[\sigma(e^+e^- \to \bar{\Lambda}^0 X)]$.

Table 10: The measured inclusive cross-sections of the 21 XYZ data samples of BESIII with statistic and systematic uncertainties. With the center-of-mass energy $\sqrt{s}$, the time-integrated luminosity $\mathcal{L}_{int}$, the number of signal events N_{sig}, the detection efficiency ε and the detection acceptance A. Efficiencies characterised with an open square are based on interpolations (section 3.5.4). The vacuum polarisation correction factors are to be found in table 8.

5.1.2. Parameters of the Measured Resonances

The parameters of the three resonances, determined by the individual and the simultaneous fits, are summarised in table 11. Along the row of the three fit variants, the mass m_2 and the width Γ_2 of the second resonance $\mathcal{R}_2$ at 4360 MeV are in agreement within their uncertainties. This also applies for the third resonance at 4415 MeV. For the first resonance at 4230 MeV, there are good agreements in mass and width of the simultaneous fit with the individual fit applied on the cross-section distribution of the inclusive $\bar{\Lambda}^0$ reconstruction.

Comparing the widths and masses of $\mathcal{R}_1$, $\mathcal{R}_2$ and $\mathcal{R}_3$ with the given values for the states $Y(4230)$, $Y(4360)$ and $\psi(4415)$ in the Particle Data Group (PDG) [125], eight out of the eighteen parameters are in agreement within their uncertainties with the given values. These PDG values are weighted averages from several experiments and are partially not creating a statistical consensus, e.g. the width of the $Y(4230)$. Comparing the remaining widths and masses of the resonances with the spread of these experimental measurements, all but one (m_1 of the individual fit of $\sigma^d_{\Lambda^0}$) are in agreement within this spread. The measurement of [70] with a determined mass $m_{Y(4230)} = 4234.4 \pm 3.2 \pm 0.2$ is the top bound of the spread, thus m_1 is 2.52 MeV away from the spread within the uncertainties. Regarding the widths and masses determined by the simultaneous fit, all masses are in agreement with the PDG values, all widths are in agreement with the spread.

	individual fit of $\sigma^m_{\Lambda^0}$		individual fit of $\sigma^m_{\bar{\Lambda}^0}$		simultaneous fit	
χ^2/ndf	1.51		2.86		2.00	
	parameter	uncertainty	parameter	uncertainty	parameter	uncertainty
I_1	29.34	7.39	48.27	9.23	49.51	15.10
m_1	4244.46	4.14	4218.80	5.78	4222.24	11.86
Γ_1	32.12	12.88	140.00	17.10	178.98	51.86
I_2	29.18	10.38	36.59	9.68	32.67	8.08
m_2	4369.23	10.49	4353.83	5.13	4358.16	5.84
Γ_2	64.37	38.89	35.19	17.04	44.66	14.11
I_3	41.98	12.76	61.70	47.75	52.86	13.20
m_3	4416.77	1.62	4420.66	4.91	4418.06	3.88
Γ_3	12.33	19.96	18.84	16.10	27.24	9.67
a_{Λ^0}	887.97	45.47			415.00	295.96
$slope_{\Lambda^0}$	-0.0121	0.0466			-0.0277	0.0683
$a_{\bar{\Lambda}^0}$			606.94	12.83	680.13	291.56
$slope_{\bar{\Lambda}^0}$			-0.0739	0.0021	-0.0924	0.0673

Table 11: Mass m_i, width Γ_i (both in MeV) and intensity I_i of the three measured resonances. The paramters a_X and $slope_X$ are describing the shape of the continuum ($X \in \{\Lambda^0, \bar{\Lambda}^0\}$).

5.2. The Dressed Energy-Dependent Cross-Section

The dressed cross-section $\sigma^d(\sqrt{s})$ is the ISR corrected measured cross-section (equation 5.1) or the vacuum polarisation corrected Born cross-section (equation 3.37) and is given by

$$\sigma^d(\sqrt{s}) = \frac{N}{\mathcal{L}_{int} \cdot \varepsilon \cdot \mathrm{A} \cdot (1+\delta) \cdot \frac{1}{|1-\Pi(s)|^2} \cdot \mathcal{B}(\Lambda^0 \to p\pi^-)} \tag{5.4}$$

with the time-integrated luminosity $\mathcal{L}_{int}$, the branching ratio $\mathcal{B}(\Lambda^0 \to p\pi^-) = 0.639 \pm 0.005$, the detection acceptance A, the reconstruction efficiency ε and the correction factors of the vacuum polarisation $1/|1-\Pi(s)|^2$ and ISR $(1+\delta_{ISR})$. The iterative procedure of the calculation of the ISR correction factor is described in section 4.3. The values of $\mathcal{L}_{int}$, A, ε and of $1/|1-\Pi(s)|^2$ are the same as for the measured cross-section discussed above; the ISR correction factors $(1+\delta_{ISR})$ and the dressed cross-section values of the inclusive reconstruction ($\sigma^d_{\Lambda^0}$ and $\sigma^d_{\bar{\Lambda}^0}$) are listed in table 13.

5.2.1. The Individual and the Simultaneous Fit of the Dressed Cross-Sections

Like for the measured cross-section, two individual fit functions (equation 5.2) are applied on each distribution of the two dressed cross-sections at first (figure 5.3). Then again, a simultaneous fit is applied on both distributions ($\sigma^d_{\Lambda^0}(\sqrt{s})$ and $\sigma^d_{\bar{\Lambda}^0}(\sqrt{s})$) to increase the number of measurements in relation to the number of parameters of the fit function. The statistical sigificance Z of the three measured resonances $\mathcal{R}_1, \mathcal{R}_2$ and $\mathcal{R}_3$ is determined using the simultaneous fit function (equation 5.2) and $Z > 5\sigma$ for all three resonances (table 15).

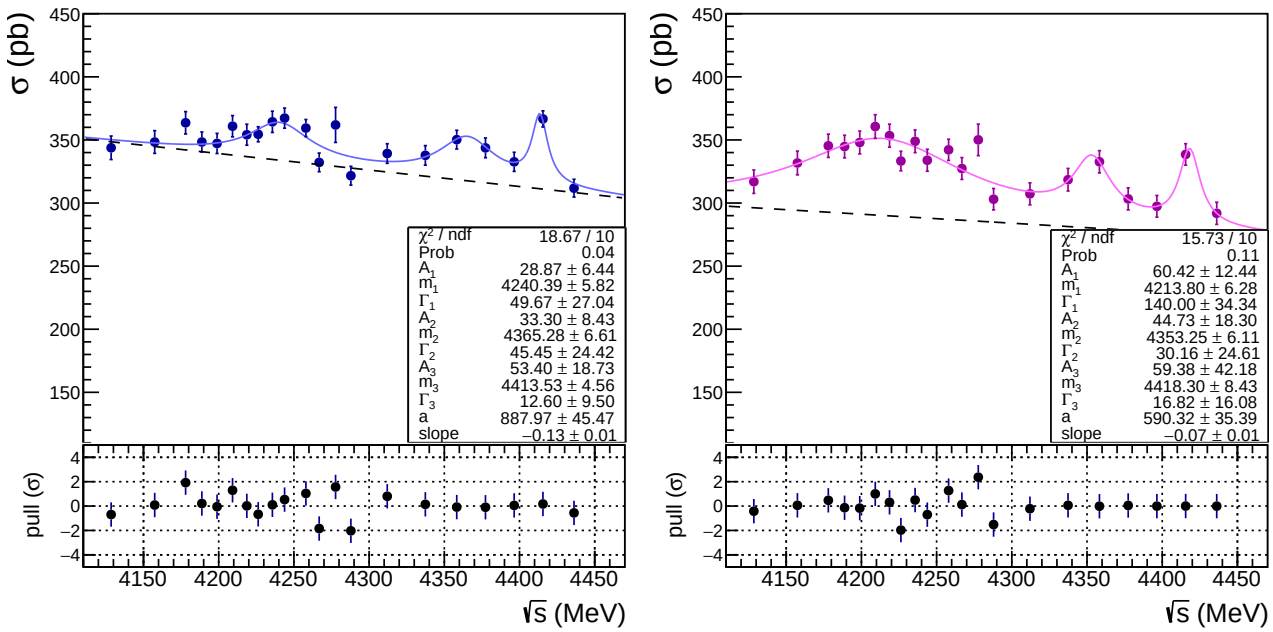

Figure 5.3: The dressed inclusive cross-sections $\sigma^d_{\Lambda^0}[\sigma(e^+e^- \to \Lambda^0 X)]$ (left, blue) and $\sigma^m_{\bar{\Lambda}^0}[\sigma(e^+e^- \to \bar{\Lambda}^0 X)]$ with individual fit functions, shown as solid lines. The dashed gray lines correspond to the continuum distributions, respectively.

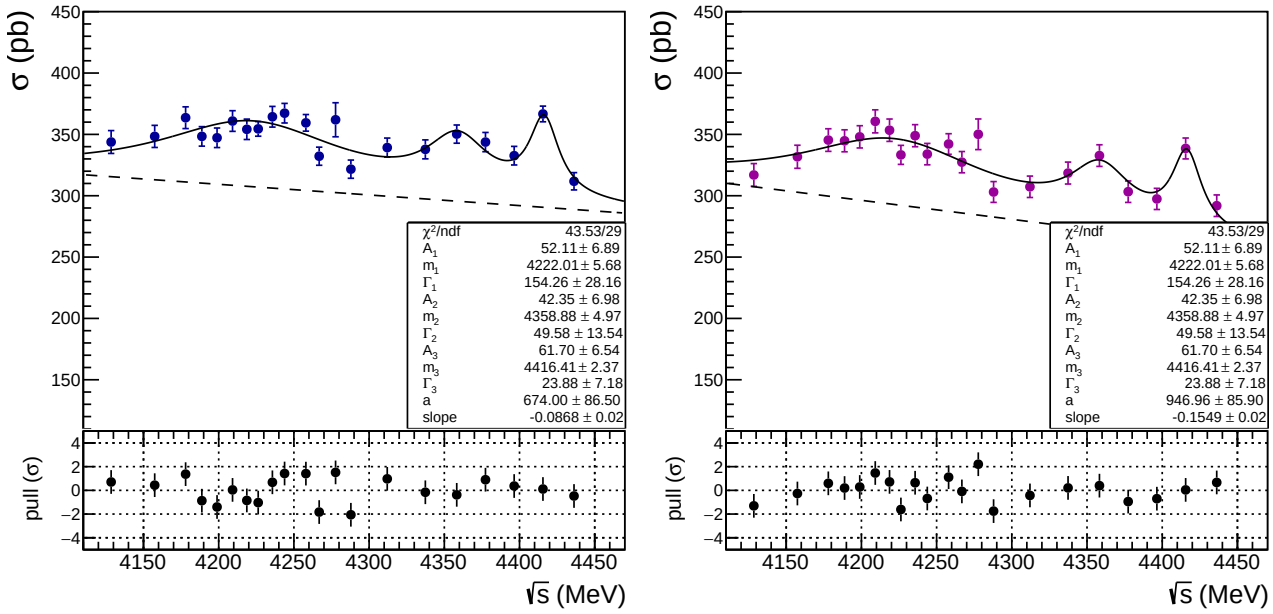

Figure 5.4: The dressed inclusive cross-section $\sigma^d_{\Lambda^0}$ $[\sigma(e^+e^- \to \Lambda^0 X)]$ (left, blue) and $\sigma^m_{\bar{\Lambda}^0}$ $[\sigma(e^+e^- \to \bar{\Lambda}^0 X)]$ with simultaneous fit function, shown as solid line. The dashed gray lines correspond to the continuum distributions, respectively.

5.2.2. Parameters of the Measured Resonances

Like for the measured cross-section (table 11), the parameters of the three resonances determined by the individual and the simultaneous fits are summarised in table **??**. Again, along the row of the three fit variants, the masses (m_2, m_3) and the widths (Γ_2, Γ_3) of the second and the third resonance at 4360 MeV and at 4415 MeV are in agreement within their uncertainties. As previously, the paramters of the simultaneous fit are in agrrement with the paramaters of the individual fit applied on the cross-section distribution of the inclusive $\bar{\Lambda}^0$ reconstruction for the first resonance at 4230 MeV.

	individual fit of $\sigma^d_{\Lambda^0}$		individual fit of $\sigma^d_{\bar{\Lambda}^0}$		simultaneous fit	
χ^2/ndf	1.87		1.57		1.50	
	parameter	uncertainty	parameter	uncertainty	parameter	uncertainty
I_1	28.87	6.44	60.42	12.44	52.11	6.89
m_1	4240.39	5.82	4213.80	6.28	4222.01	5.68
Γ_1	49.67	27.04	140.00	34.34	154.26	28.16
I_2	33.30	8.43	44.73	18.30	42.35	6.98
m_2	4365.28	6.61	4353.25	6.11	4358.88	4.97
Γ_2	45.45	24.42	30.16	24.61	49.58	13.54
I_3	53.40	18.73	59.38	42.18	61.70	6.54
m_3	4413.53	4.56	4418.30	8.43	4416.41	2.37
Γ_3	12.60	9.50	16.82	16.08	23.88	7.18
a_{Λ^0}	887.97	45.47			670.00	86.50
$slope_{\Lambda^0}$	-0.0131	0.0118			-0.0868	0.0211
$a_{\bar{\Lambda}^0}$			590.32	35.39	946.96	58.90
$slope_{\bar{\Lambda}^0}$			-0.0712	0.0079	-0.1549	0.0210

Table 12: Mass m_i, width Γ_i (both in MeV) and intensity I_i of the three measured resonances. The paramters a_X and $slope_X$ are describing the shape of the continuum $(X \in \{\Lambda^0, \bar{\Lambda}^0\})$.

Comparing the widths and masses of $\mathcal{R}_1$, $\mathcal{R}_2$ and $\mathcal{R}_3$ with the PDG values, seven out of the eighteen parameters are in agreement within their uncertainties with the given values for the states $Y(4230)$, $Y(4260)$ and $\psi(4415)$. The remaining parameters of the widths and masses are in agreement with the spread of the experimental measurements, exept for Γ_3 of the individual fit of $\sigma^d_{\Lambda^0}(\sqrt{s})$. The measurement of [47] with a determined width of $\Gamma_{\psi(4415)} = 33 \pm 10$ is the lower bound of the spread, thus Γ_3 is 0.9 MeV away from the spread within the uncertainties. Like for the measured cross-section, the simultaneous fit on the dressed cross-section results in masses in agreement with the PDG values and in widths in agreement with the spread.

	$e^+e^- \to \Lambda^0 X$		$e^+e^- \to \bar{\Lambda}^0 X$	
$\sqrt{s}$ (MeV)	$(1+\delta_{ISR})$	$\sigma^d_{\Lambda^0} \pm \delta_{stat} \pm \delta_{sys}$ (pb)	$(1+\delta_{ISR})$	$\sigma^d_{\bar{\Lambda}^0} \pm \delta_{stat} \pm \delta_{sys}$ (pb)
4128.48	0.9752	343.78 ± 8.58 ± 3.61	0.9934	316.92 ± 6.40 ± 6.71
4157.44	0.9693	348.35 ± 8.21 ± 3.72	0.9870	331.75 ± 6.33 ± 6.95
4178.00	0.9654	363.59 ± 7.95 ± 3.91	0.9826	345.37 ± 5.82 ± 7.14
4188.80	0.9641	348.37 ± 7.05 ± 3.67	0.9811	344.77 ± 5.38 ± 7.17
4198.90	0.9636	347.23 ± 7.04 ± 3.72	0.9806	348.00 ± 5.46 ± 7.23
4209.20	0.9643	360.89 ± 7.53 ± 3.77	0.9812	360.62 ± 5.68 ± 7.47
4218.70	0.9658	354.13 ± 7.46 ± 3.67	0.9829	353.40 ± 5.43 ± 7.33
4226.26	0.9678	354.49 ± 4.66 ± 3.73	0.9850	333.30 ± 3.51 ± 6.91
4235.70	0.9707	364.37 ± 7.49 ± 3.86	0.9882	348.93 ± 5.32 ± 7.25
4243.80	0.9735	367.28 ± 6.95 ± 3.92	0.9913	333.92 ± 5.19 ± 7.00
4257.97	0.9786	359.41 ± 5.66 ± 3.72	0.9971	342.16 ± 4.14 ± 7.29
4266.80	0.9816	332.21 ± 6.45 ± 3.59	1.0006	327.36 ± 5.06 ± 7.02
4277.70	0.9849	361.91 ± 13.38 ± 3.66	1.0044	350.08 ± 9.89 ± 7.62
4287.88	0.9874	321.65 ± 6.64 ± 3.32	1.0073	303.04 ± 5.18 ± 6.72
4312.05	0.9900	339.25 ± 6.91 ± 3.51	1.0107	307.29 ± 5.22 ± 6.98
4337.39	0.9829	337.79 ± 6.85 ± 3.57	1.0030	318.48 ± 5.38 ± 7.14
4358.26	0.9732	350.23 ± 6.40 ± 3.75	0.9920	332.71 ± 4.97 ± 7.29
4377.37	0.9920	343.73 ± 6.93 ± 3.64	1.0135	303.29 ± 5.14 ± 7.07
4396.45	0.9923	332.65 ± 6.69 ± 3.55	1.0144	297.39 ± 5.05 ± 6.98
4415.58	0.9746	366.65 ± 5.18 ± 3.75	0.9938	338.53 ± 3.79 ± 7.62
4436.24	1.0081	311.78 ± 6.23 ± 3.30	1.0333	291.86 ± 4.91 ± 7.29

Table 13: The dressed inclusive cross-sections of the 21 XYZ data samples of BESIII with statistic and systematic uncertainties. With the center-of-mass energy $\sqrt{s}$ and the ISR correction factor $(1+\delta_{ISR})$. The omitted paramters of equation 5.4 are listed in the tables 8 and 10.

5.3. The Statistical Significance of a Measured Resonance

The statistical significance Z of the resonances in the energy-dependent cross-section is estimated as in [56], using the comparison of Δndf to $\Delta\chi^2$, based on the analogy between the likelihood L and the chi-square χ^2. The number of degrees of freedom (ndf) is given by $N-K$, for N independent measurements and K fit parameters.

A chi-squared test [126] is a statistical hypothesis test, which determines the probability of a hypothesis, where the parameters $\boldsymbol{\theta}$ are estimated such, that the log-likelihood function

$$\chi^2(\boldsymbol{\theta}) = -2\ln L(\boldsymbol{\theta}) + \text{constant} = \sum_{i=1}^{N} \frac{(y_i - \mu_i(x_i;\boldsymbol{\theta}))^2}{\sigma_i^2} \tag{5.5}$$

is minimised, analogous to the maximisation of the likelihood L. The N independent measurements y_i at x_i points are assumed to be a gaussian distributed with mean $\mu_i(x_i;\boldsymbol{\theta})$ and known

variance σ_i^2. The change of chi-square is $\Delta\chi^2 = \Delta(-2\ln L)$.

In general, a specific χ_i^2 of a probabilty distribtion $\mathrm{P}(\chi^2)$ for a given ndf can be transformed into a statistical significance $Z(\chi_i^2)$ in units of Gaussian standard deviations. The probability p_i of χ_i^2 is connected to the probability density $\phi_{\mu,\sigma^2}(x)$ by

$$p = 1 - \int_{-Z}^{+Z} \phi_{\mu,\sigma^2}(x)\,\mathrm{d}x \qquad \text{with} \quad \phi_{\mu,\sigma^2}(x) = \frac{1}{\sigma\sqrt{2\pi}} \cdot e^{-\frac{1}{2}(x-\mu)^2} \tag{5.6}$$

synonymous with: the shaded areas of $\phi_{\mu,\sigma^2}(x)$ (figure 5.5, right), are of same size as the shaded area of $P(\chi^2)$ (figure 5.5, left).

In this analysis, the probability p is determined using the difference of the χ^2 of the hypothesis H_0 (there is no resonance) and of the hypothesis H_1 (there is a resonance) in comparison to the difference of the ndf. In the aftermath of the initial fit (equation 5.2) on the cross-section, two more fits are applied, where the parameters not concerning the probed resonance are fixed to the values of the resulting parameters of the initial fit. First, the fit is applied with a free parameter for the intensity I of the resonance, giving $\chi^2(H_1)$. Then again the intensity is set to zero ($I = 0$), giving $\chi^2(H_0)$. Subsequently $\Delta\chi^2 = \chi^2(H_1) - \chi^2(H_0)$ and $\Delta\mathrm{ndf} = 1$ (intensity fixed/non-fixed) allow to determine the probability p, and then again Z.

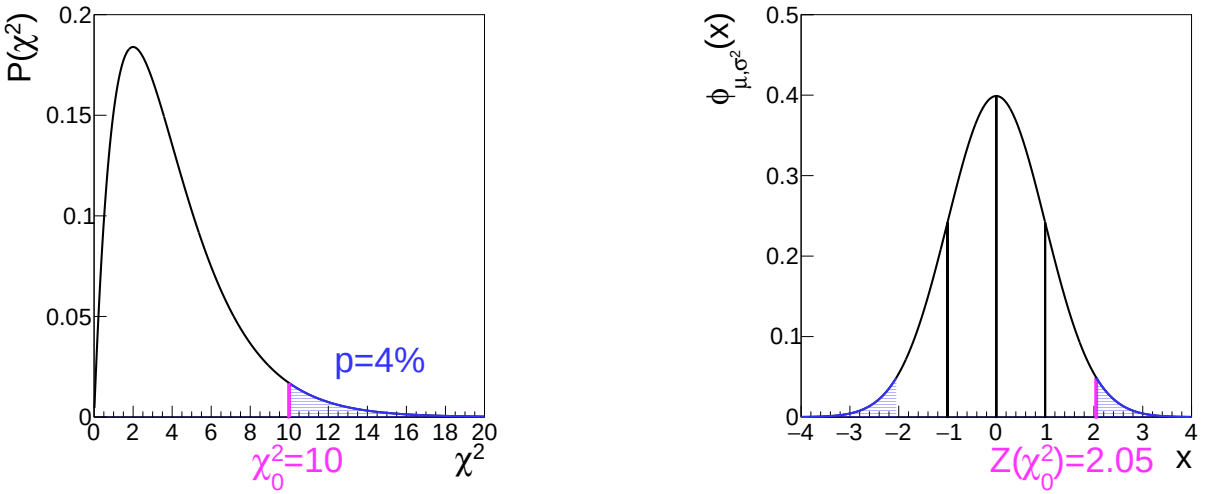

Figure 5.5: Left: The χ^2 distribution for 10 ndf. The shaded area to the right of $\chi_0^2 = 10$ represents the probability of 4%. Right: The probability densitiy distribution with $\mu = 0$ and $\sigma = 1$. The statitical significance Z is the value in σ at the edge of the integrals, $Z = 2.05\,\sigma$.

5.4. The Measured Resonances: Comparison of both Approaches

The resonance parameters of the simultaneous fit of the measured and of the dressed cross-section are listed both in table 14. The relative difference $\Delta\mathrm{p}_i$ of the respective resonance parameters (p_i^m and p_i^d) determined by the two cross-sections is given by

$$\Delta p_i = \left|1 - \frac{p_i^m}{p_i^d}\right| \cdot 100 \tag{5.7}$$

and is listed in the last column. The relative difference of the masses of all three resonances is less than 0.05%; their widths show a greater relative difference, but are in agreement within

their uncertainties. For the second and the third resonance, the parameters of the intensity are significantly greater for the fit function applied on the dressed cross-section than compared to the ones determined by the measured cross-section. This is reflected by the increase of the statistical sgnificance Z (table 15) and also by the increse of the signal height in the contiuunum subtracted cross-section (figure 5.6). The statitsical significance of the first resonance $\mathcal{R}_1$ is not enlarged, since the intensity determined by the measured cross-section covers the intensity determined by the dressed cross-section within its uncertainty. All three resonances have a statistical significance $Z > 5\sigma$ in both simultaneous fits on the respective cross-section distributions, measured and dressed. In general, $Z > 5\sigma$ is termed an observation.

	simultaneous fit σ^m		simultaneous fit σ^d		Δp_i (%)	PDG values	
χ^2/ndf	2.00		1.50				
	parameter	uncertainty	parameter	uncertainty		value	uncertainty
I_1	49.51	15.10	52.11	6.89	4.99		
m_1	4222.24	11.86	4222.01	5.68	0.01	4222.7	2.6
Γ_1	178.98	51.86	154.26	28.16	16.02	49	8
I_2	32.67	8.08	42.35	6.98	22.86		
m_2	4358.16	5.84	4358.88	4.97	0.02	4372	9
Γ_2	44.66	14.11	49.58	13.54	9.92	115	13
I_3	52.86	13.20	61.70	6.54	14.33		
m_3	4418.06	3.88	4416.41	2.37	0.04	4421	4
Γ_3	27.24	9.67	23.88	7.18	14.07	62	20

Table 14: Comparison of the resonance parameters, determined by σ^m and σ^d.

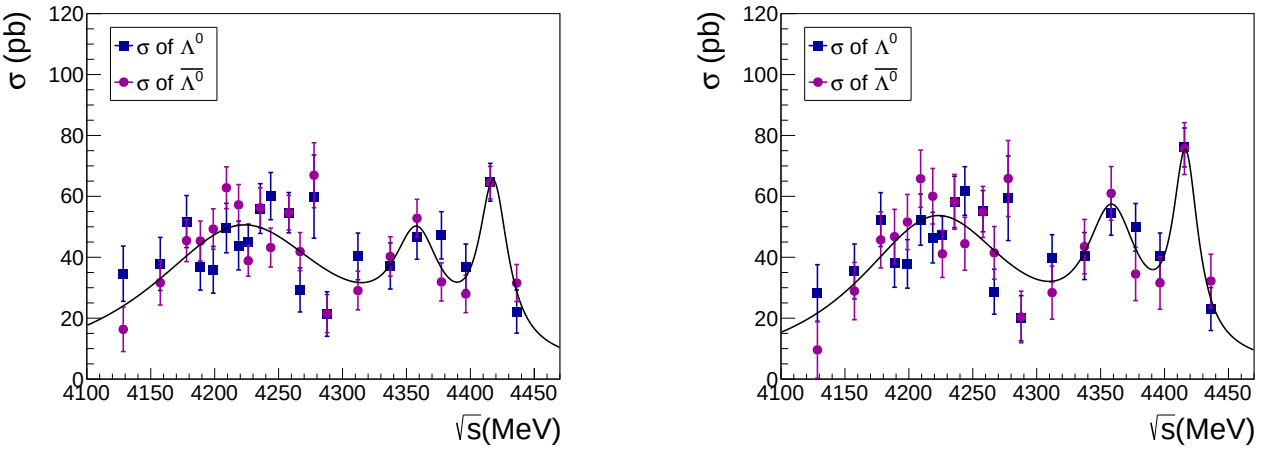

Figure 5.6: Continuum subtracted cross-sections of Λ^0 and $\bar{\Lambda}^0$ with the singnal part of the respective simultaneous fit functions (solid lines). Left: $\sigma^m(\sqrt{s})$. Right: $\sigma^d(\sqrt{s})$.

σ^m

	$\chi^2(H_0)$	$\chi^2(H_1)$	$\Delta\chi^2$	$Z(\sigma)$
$\mathcal{R}_1$	114.30	57.69	56.61	7.52
$\mathcal{R}_2$	89.06	57.64	31.64	5.61
$\mathcal{R}_3$	120.57	57.69	62.88	7.93

σ^d

	$\chi^2(H_0)$	$\chi^2(H_1)$	$\Delta\chi^2$	$Z(\sigma)$
$\mathcal{R}_1$	98.56	43.40	55.16	7.42
$\mathcal{R}_2$	78.64	43.46	35.18	5.93
$\mathcal{R}_3$	109.76	43.38	66.38	8.15

Table 15: Statistical significance $Z(\sigma)$ of the three measured resonances. The left table shows the results by the measured cross-section, the right table the ones by the dressed cross-section.

6. Summary and Outlook

For several decades, the search for exotic states beyond the quark model, predicted by QCD (Quantum Chromodynamics), had been of great interest. The observation of the XYZ states, especially of the charged Z states, can be considered as a proof of their existence. Nevertheless, the nature of these states are not fully explained to date.

The supernumerary and unpredicted $Y(4230)$, formally known as $Y(4260)$, is a state of great interest. The search for new decay channels of exotic candidates and further measurements of their properties is a significant contribution to the identification of their inner structure.

This analysis, determining the efficiency corrected yield, is based on the proton momentum to adress the momentum discrepancies between *generic MC* and measured data. The proton is a decay product of Λ^0 and can be used as a representative. By this technique, the energy-dependent cross-section for the inclusive reaction channels $e^+e^- \to \Lambda^0 X$ and $e^+e^- \to \bar{\Lambda}^0 X$ has been determined at 21 energy points. Three resonant structures appeared in the energy-dependent cross-section: the first can be interpreted as the $Y(4230)$, the second as the $Y(4360)$ and the third as the $\psi(4415)$, all three with a statistical significance $Z > 5\sigma$. It seems this is the first time of an observation of a strange baryonic decay of Y states.

The momentum-dependent analysis shows a great potential for inclusive reconstructions. However, the background reduction has to be improved by a further developement of the *generic MC*. Additional data samples within and beyond the analysed energy regime with sufficiently high integrated luminosities might be useful to adress the shape of the continuum in the subsequent cross-section and to improve the fit model.

7. Zusammenfassung

7.1. Theoretischer Hintergrund

Das Standardmodell der Elementarteilchenphysik (SM) beschreibt Elementarteilchen und ihre Interaktionen, wie den Quarks und den Leptonen, und ist im Allgemeinen als die grundlegende Theorie der Elementarteilchenphysik anerkannt, da seit 50 Jahren Experimente seine Gültigkeit bestätigen. Sämtliche sichtbare Materie des Universums besteht aus Quarks und Leptonen: Protonen und Neutronen, Bausteine der Atomkerne, werden durch jeweils drei Quarks gebildet. Elektronen, die leichtesten Leptonen, umgeben den Atomkern und bilden die Atomhülle. Weiterhin können drei der vier fundamentalen Wechselwirkungen durch das SM beschrieben werden.

Dennoch gibt es bis heute ungeklärte Sachverhalte, wie beispielsweise das Phänomen des "Confinements" und die Entdeckung der überzähligen XYZ Zustände. Die XYZ Zustände mit Massen im Charmoniumbereich werden auch als charmoniumähnlilch bezeichnet, da sie wie jeder Charmonium-Zustand ein $c\bar{c}$ Paar enthalten; jedoch können ihre Eigenschaften bis heute nicht umfassend erklärt werden.

7.2. Das BESIII Experiment

Das BESIII Experiment (Beijing Spectrometer III) und der BEPCII (Beijing Electron-Positron Collider II) werden seit 2008 am IHEP (Institute for High Energy Physics) in Peking, VR China, betrieben. Mehr als 72 beteiligte Forschungsinstitute aus 15 Ländern arbeiten bei BESIII. Die im mehr als 200 Meter langen LINAC (Linear Accelerator) vorbeschleunigten Leptonen (e^+e^-) werden im Speicherring mit einem Umfang von knapp 240 Metern zur Kollision gebracht. Hierbei werden Schwerpunktsenergien zwischen 2.0 und 4.95 GeV erreicht und decken somit den Massebereich von XYZ Zuständen ab. Das Spektrometer, mit einer Gesamtlänge von sechs und einem Umfang von sieben Metern, ist um den Kollisionspunkt herum aufgebaut und besteht aus mehreren Detektoren unterschiedlicher Funktion: der Driftkammer zur Rekonstruktion der Flugbahn geladener Teilchen, dem Flugzeitdetektor zur Identifikation der Teilchenmasse, dem elektromagentischen Kalorimeter zur Messung der Photonenenergie und dem Myonendetektor zur Unterscheidung von Myonen von Hadronen und insbesondere Pionen.

Mittels des BESIII Detektors wurden die bisher größten Datensätze der Produktionsreaktionen von J/ψ, $\psi(2S)$ und $\psi(3770)$ aufgenommen und erlauben die Untersuchung seltener Prozesse. Daher umfasst das Feld der BESIII Forschungsgruppen einen weites Spektrum: Die Spektroskopie von charm-Quarkonia und leichter Hadronen, Studien zu elektroschwacher und starker Wecheselwirkung, die Untersuchung des τ Leptons und Physik jenseits des SM. Dies beinhaltet die Untersuchung exotischer Zustände, um deren Eigenschaften besser zu verstehen.

7.3. Die XYZ Zustände

Innerhalb des SM können konventionelle charm-Quarkonia wie das J/ψ und das $\psi(2S)$ gut mittels des Potentialmodells beschrieben werden. Seit mehr als 20 Jahren werden überzählige und unkonventionelle Zustände u.a. an den Experimenten BESIII, Belle und BaBar entdeckt, die dieses Modell nicht umfasst. Diese nach dem Potentialmodell unkonventionellen Zustände können möglicherweise als exotische, innerhalb der QCD (Quanten Chromo Dynamic) erlaubte und vorhergesagte Zustände interpretiert werden. Diese Interpretationen sind Tetra- und Pen-

taquarks, hadronische Moleküle, hybride Zustände aus Quarks und Gluonen oder Objekte ausschließlich aus Gluonen bestehend.

Analog der Atomspektroskopie können konventionelle charm-Quarkonia im Rahmen eines Termschemas dargestellt werden. Zustände unterhalb der $D\bar{D}$ Masse stimmen mit der spektroskopischen Beschreibung überein, wohingegen oberhalb dieses Grenzwertes viele Zustände dieser Beschreibung nicht folgen.

Die bekanntesten exotischen Zustände sind die folgenden vier neutralen $X(3872)$, $Y(4230)$, $Y(4360)$ und $Y(4660)$ und die vier geladenen $Z_c(3900)^{\pm}$, $Z_c(4020)^{\pm}$, $Z_c(4200)^{\pm}$, $Z_c(4430)^{\pm}$). Die Entdeckung des $Y(4230)$ und des $Y(4360)$ sind miteinander verknüpft. Der von BaBar entdeckte Zustand $Y(4260)$ (2005, 2007 durch Belle bestätigt) wurde am BESIII Experiment erneut anhand eines Datensatzes höherer Luminosität untersucht und es zeigten sich zwei Resonanzen anstelle einer. Für das $Y(4230)$ und das $Y(4360)$ liegen verschiedene Interpretationen vor; eine davon ist, dass es sich um einen Überlagerungszustand handelt (sog. $S-D$-mixing). Ungewöhnlicherweise zerfällt das $Y(4230)$ bevorzugt in $c\bar{c}$ Zustände ("hidden charm decay") wie das J/ψ oder das h_c, und nicht in D Mesonen Paare ("open charm decay"), obwohl es mit seiner Masse oberhalb des Schwellenwertes liegt.

7.4. Motivation der Arbeit

In dieser Arbeit wurde die Reaktion $e^+e^- \to \Lambda^0 X$ $(+\,c.c.)$ rekonstruiert. Die verwendeten 21 Datensätze, mit einer totalen integrierten Luminosität von $14.5\,\mathrm{fb}^{-1}$, wurden in den Jahren 2012, 2016, 2017 und 2019 durch BESIII aufgenommen. Sie werden als XYZ Datensätze bezeichnet, da sie den Massebereich von charmoniumähnlichen Zuständen abdecken.

Zunächst wurde die "missing mass" der inklusiven Rekonstruktion untersucht, da diese Analysemethode in verschiedenen Experimenten in den letzten beiden Jahrzehnten erfolgreich Verwendung fand. Jedoch zeigten sich keine ausgeprägten Signale, sodass keine weiteren am Zerfallsprozess beteiligten Teilchen identifiziert werden konnten.

Die Motivation der Messung der energieabhägigen Wirkungsquerschnitte $\sigma_{\Lambda^0 X}(\sqrt{s})$ und $\sigma_{\bar{\Lambda}^0 X}(\sqrt{s})$ begründet sich durch zwei am BESIII durchgeführte Messungen: Die exklusive Rekonstruktion der Reaktion $e^+e^- \to \Lambda\bar{\Lambda}$, 2021 veröffentlicht, die eine Resonanz bei $\sqrt{s} = 3.77\,\mathrm{GeV}$ zeigte, die als das $\psi(3770)$ intepretiert wird, und die exklusive Rekonstruktion der Reaktion $e^+e^- \to K^+K^- J/\psi$, 2022 veröffentlicht. Letztere zeigte eine bekannte Resonanz bei $\sqrt{s} = 4.23\,\mathrm{GeV}$, die als $Y(4230)$ interpretiert wird, und eine bei $\sqrt{s} = 4.5\,\mathrm{GeV}$, die als neuer Zustand interpretiert wird, dem $Y(4500)$.

Die zweite Messung zeigt einen "open strange" Zerfall des $Y(4230)$ in K Mesonen. Demnach kann vermutet werden, dass es weitere strange Quark beinhaltende Zerfallkanäle des $Y(4230)$ gibt. Die erste Publikation ist auf das $\Lambda\bar{\Lambda}$ System als Endzustand beschränkt und zeigte keine Resonanzen im Massebereich $\sqrt{s} > 4\,\mathrm{GeV}$. Um sämtliche mögliche baryonische Zerfallskanäle mit Strangeness (sogenannte Hyperonen) berücksichtigen zu können, wurde eine inklusive Rekonstruktion in dieser Analyse durchgeführt.

7.5. Methode und Ergebnis der Arbeit

Zur Effizienz- und Akzeptanzbestimmung werden sogenannte "generische MC-Simulationsereignisse" verwendet, da sie den verfügbaren Phasenraum durch einen Mix aus bekannten Reaktionskanälen in akzeptabler Weise ausfüllen. Aufgrund des Unterschieds der Form der Protonenimpulsverteilung von der experimentell gemessenen Verteilung, wurde die impulsab-

hängige Analysemethode verwendet: Teilchenausbeute (N) und Effizienz (ε) werden in Abhängigkeit des Protonenimpulses bestimmt, d.h. die weitere Analyse erfolgte unter Verwendung des Tochterteilchens, des Protons, als Repräsentant des Λ^0.

Die Korrekturfaktoren der Vakuumspolarisation wurden der oben genannten 2022 veröffentlichen Messung durch BESIII entnommen. Zur Reduktion des statistischen Fehlers auf die effizienzgewichtete Ausbeute ist eine Selektion des untersuchten Protonenimpulsbereiches notwendig. Nach einer Optimierung der Selektion wurden neben den individuellen Fits auch ein simultaner Fit auf die resultierenden energieabhängigen Wirkungsquerschnittverteilungen $\sigma_{\Lambda^0 X}(\sqrt{s})$ und $\sigma_{\bar{\Lambda}^0 X}(\sqrt{s})$ durchgeführt.

Unter Verwendung der simultanen Fitfunktion erfolgte iterativ die Berechnung der ISR (Initial State Radiation) Korrekturfaktoren. Diese Strahlungskorrektur wurde auf den Eingangszustand angewendet, zur Emittlung des sogenannten "Dressed"-Wirkungsquerschnittes. Im Anschluss wurden wieder individuelle und simultane Fits durchgeführt.

Es wurden drei Resonanzen[1] in dem energieabhängigen Wirkungsquerschnitt beobachtet: Die erste mit einer Masse von $(4222.01 \pm 5.68)\,\text{MeV}$ und einer Breite von $(154.26 \pm 28.16)\,\text{MeV}$, die zweite mit einer Masse von $(4358.88 \pm 4.97)\,\text{MeV}$ und einer Breite von $(49.58 \pm 13.54)\,\text{MeV}$ und eine dritte mit einer Masse von $(4416.41 \pm 2.37)\,\text{MeV}$ und einer Breite von $(23.88 \pm 7.18)\,\text{MeV}$.

7.6. Schlussfolgerung

Die beobachteten Resonanzen können als die Zustände $Y(4230)$, $Y(4360)$ und $\psi(4415)$ interpretiert werden und weisen jeweils eine statistische Signifikanz $Z > 5\sigma$ auf. Unter der betrachteten Hypothese ist dies der erste Nachweis baryonischer bzw. hyperonischer Zerfallskanäle der drei genannten Resonanzen. Die hier verwendete impulsabhängige Analysemethode birgt ein großes Potential für weitere inklusive Rekonstruktionen. Jedoch muss die Untergrundsreduktion weiter optimiert werden mittels einer Überarbeitung der generischen MC Untergrundsimulation. Zudem wären weitere Datensätze ausreichender Liminosität außerhalb des untersuchten Energiebereiches hilfreich, um die Form des Kontinuums besser zu beschreiben. Eine besseres Modell zur Beschreibung des Kontinuums würde eine genauere Beschreibung der Resonanzen im Wirkungsquerschnitt ermöglichen.

[1] Die Werte der Resonanzparameter entstammen der simultanen Fitfunktion angewendet auf den ISR korrigierten Wirkungsquerschnitt.

Zusammenfassung

Theoretischer Hintergrund

Das Standardmodell der Elementarteilchenphysik (SM) beschreibt Elementarteilchen und ihre Interaktionen. Da seit 50 Jahren Experimente seine Gültigkeit bestätigen, ist es im Allgemeinen als die grundlegende Theorie der Elementarteilchenphysik anerkannt. Dennoch gibt es bis heute ungeklärte Sachverhalte, wie beispielsweise das Phänomen des "Confinements" und die Entdeckung der überzähligen XYZ Zustände. Die Eigenschaften dieser XYZ Zustände mit Massen im Charmoniumbereich können bis heute nicht umfassend erklärt werden.

Das BESIII Experiment

Das BESIII Experiment (Beijing Spectrometer III) und der BEPCII (Beijing Electron-Positron Collider II) werden seit 2008 am IHEP (Institute for High Energy Physics) in Peking, VR China, betrieben. Leptonen (e^+e^-) werden mit Schwerpunktsenergien zwischen 2.0 und 4.95 GeV zur Kollision gebracht und decken somit den Massebereich von XYZ Zuständen ab. Die innere Struktur und weitere Eigenschaften dieser überzähligen Zustände können so untersucht werden.

Mittels des BESIII Detektors wurden die bisher größten Datensätze von J/ψ, $\psi(2S)$ und $\psi(3770)$ Produktionsreaktionen aufgenommen.

Die *XYZ* Zustände

Innerhalb des SM können konventionelle charm-Quarkonia wie das J/ψ und das $\psi(2S)$ gut mittels des Potentialmodells beschrieben werden. Seit mehr als 20 Jahren werden überzählige und unkonventionelle Zustände u.a. an den Experimenten BESIII, Belle und BaBar entdeckt, die dieses Modell nicht umfasst. Diese nach dem Potentialmodell unkonventionellen Zustände können möglicherweise als exotische, innerhalb der QCD (Quanten Chromo Dynamic) erlaubte und vorhergesagte Zustände interpretiert werden.

Analog der Atomspektroskopie können konventionelle charm-Quarkonia im Rahmen eines Termschemas beschrieben werden. Zustände unterhalb der $D\bar{D}$ Masse stimmen mit der spektroskopischen Beschreibung überein, wohingegen oberhalb dieses Grenzwertes viele Zustände dieser Beschreibung nicht folgen. Ungewöhnlicherweise zerfällt das $Y(4230)$ bevorzugt in $c\bar{c}$ Zustände ("hidden charm decay") wie das J/ψ, und nicht in D-Mesonen Paare ("open charm decay"), obwohl es mit seiner Masse oberhalb des Schwellenwertes liegt.

Motivation der Arbeit

In dieser Arbeit wurde die Reaktion $e^+e^- \to \Lambda^0 X$ $(+\,c.c.)$ rekonstruiert. Die verwendeten 21 Datensätze, mit einer totalen integrierten Luminosität von $14.5\,\mathrm{fb}^{-1}$, wurden in den Jahren 2012, 2016, 2017 und 2019 durch BESIII aufgenommen. Die Motivation in der Messung der beiden energieabhägigen Wirkungsquerschnitte $\sigma_{\Lambda^0 X}(\sqrt{s})$ und $\sigma_{\bar{\Lambda}^0 X}(\sqrt{s})$ begründet sich durch zwei durch BESIII veröffentlichten Messungen: Zunächst die exklusive Rekonstruktion der Reaktion $e^+e^- \to \Lambda\bar{\Lambda}$ im Jahr 2021, die eine Resonanz bei $\sqrt{s} = 3.77\,\mathrm{GeV}$ zeigte, die als das $\psi(3770)$ intepretiert wird, und die exklusive Rekonstruktion der Reaktion $e^+e^- \to K^+K^-J/\psi$, 2022 veröffentlicht. Letztere zeigte eine bekannte Resonanz bei $\sqrt{s} = 4.23\,\mathrm{GeV}$, dem $Y(4230)$, und eine bei $\sqrt{s} = 4.5\,\mathrm{GeV}$ die als neuer Zustand interpretiert wird, dem $Y(4500)$.

Die zweite Messung zeigt einen "open strange" Zerfall des $Y(4230)$ in K-Mesonen, d.h. es kann vermutet werden, dass es weitere strange Quark beinhaltende Zerfallkanäle des $Y(4230)$ gibt. Jedoch ist die erste Publikation auf das $\Lambda\bar{\Lambda}$ System als Endzustand beschränkt und zeigte keine Resonanzen im Massebereich $\sqrt{s} > 4\,\text{GeV}$. Um auch baryonische Zerfallskanäle mit Strangeness (sogenannte Hyperonen) zu berücksichtigen, wurde eine inklusive Rekonstruktion in dieser Analyse durchgeführt.

Methode und Ergebnis der Arbeit

Zur Effizienz- und Akzeptanzbestimmung werden sogenannte "generische MC-Simulationsereignisse" verwendet, da sie den verfügbaren Phasenraum durch einen Mix aus bekannten Reaktionskanälen in akzeptabler Weise ausfüllen. Aufgrund des Unterschieds der Form der Protonenimpulsverteilung von der experimentell gemessenen Verteilung, wurde die impulsabhängige Analysemethode verwendet: Teilchenausbeute (N) und Effizienz (ε) werden in Abhängigkeit des Protonenimpulses bestimmt, d.h. die weitere Analyse erfolgte unter Verwendung des Tochterteilchens, des (Anti-)Protons, als Repräsentant des Λ^0 ($\bar{\Lambda}^0$).

Nach einer Optimierung der Selektion des untersuchten Protonenimpulsbereiches wurden neben den individuellen Fits auch ein simultaner Fit auf die resultierenden energieabhängigen Wirkungsquerschnittverteilungen $\sigma_{\Lambda^0 X}(\sqrt{s})$ und $\sigma_{\bar{\Lambda}^0 X}(\sqrt{s})$ durchgeführt.

Unter Verwendung der simultanen Fitfunktion erfolgte iterativ die Berechnung der ISR (Initial State Radiation) Korrekturfaktoren. Diese Strahlungskorrektur wurde auf den Eingangszustand angewendet, zur Emittlung des sogenannten "Dressed"-Wirkungsquerschnittes. Im Anschluss wurden wieder individuelle und simultane Fits durchgeführt.

Es wurden drei Resonanzen[1] in dem energieabhängigen Wirkungsquerschnitt beobachtet: Die erste mit einer Masse von $(4222.01 \pm 5.68)\,\text{MeV}$ und einer Breite von $(154.26 \pm 28.16)\,\text{MeV}$, die zweite mit einer Masse von $(4358.88 \pm 4.97)\,\text{MeV}$ und einer Breite von $(49.58 \pm 13.54)\,\text{MeV}$ und eine dritte mit einer Masse von $(4416.41 \pm 2.37)\,\text{MeV}$ und einer Breite von $(23.88 \pm 7.18)\,\text{MeV}$.

Schlussfolgerung

Die beobachteten Resonanzen können als die Zustände $Y(4230)$, $Y(4360)$ und $\psi(4415)$ interpretiert werden und weisen jeweils eine statistische Signifikanz $Z > 5\sigma$ auf. Unter der betrachteten Hypothese ist dies der erste Nachweis baryonischer bzw. hyperonischer Zerfallskanäle der drei genannten Resonanzen.

Die Untergrundsreduktion muss weiter optimiert werden mittels einer Überarbeitung der generischen MC Untergrundsimulation. Zudem wären weitere Datensätze ausreichender Liminosität außerhalb des untersuchten Energiebereiches hilfreich, um die Form des Kontinuums besser zu beschreiben. Eine besseres Modell zur Beschreibung des Kontinuums würde eine genauere Beschreibung der Resonanzen im Wirkungsquerschnitt ermöglichen.

[1] Die Werte der Resonanzparameter entstammen der simultanen Fitfunktion angewendet auf den ISR korrigierten Wirkungsquerschnitt.

Appendices

A & B: Analysis of antiprotons from $\bar{\Lambda}^0$ candidates

For better clarity, the results of the $\bar{\Lambda}^0$ reconstruction had been omitted in the sections 3.2.2, 3.5.1, 3.5.2 and 3.6, and are shown here in A and B. To simplify a comparison, the corresponding figures of the Λ^0 reconstruction are referenced in parentheses at the beginning in the captions.

C: Acceptance Correction

A brief discussion of the influence of the lower and higher (anti-)proton selection boundary on the acceptance takes place in C.

D: Look-up Tables and Multiplicity Distribution

For better clarity, several look-up tables had been omitted in section 4 and are shown here: first, the PID uncertainty and an exemplary sideband-subtracted multiplicity $(\cos(\theta), p)$ for D4230 of protons. Then again, all look-up tables of the PID uncertainty and tracking error of $p, \overline{p}, \pi^+, \pi^-$.

A. Event Selection

A.1. The Difference in Antiproton Momentum Spectra between Data and MC

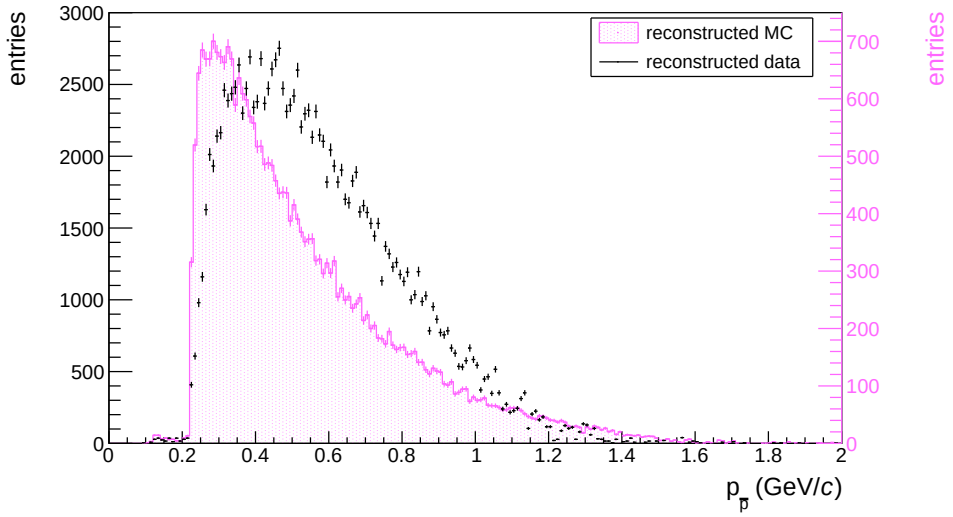

Figure A.1: (3.2) Sideband-subtracted antiproton momentum spectra ($\bar{\Lambda}^0$ reconstruction) of *generic MC* (pink, right scale) and of measured data (black, left scale) of D4230 with applied selections (table 5).

B. Inclusive Yield and Reconstruction Efficiency

B.1. Efficiency Calculation

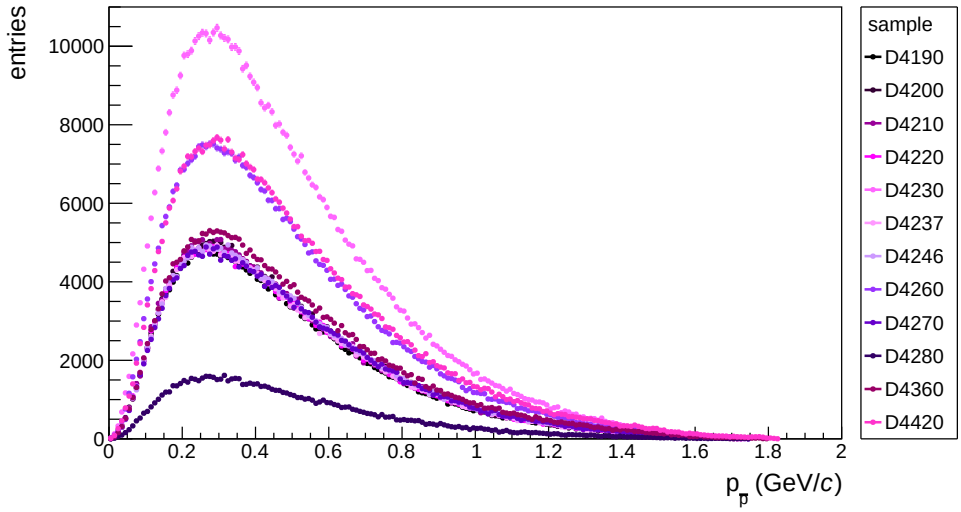

Figure B.1: (3.9) *Generic MC*: Momentum spectra of MC generator antiprotons.

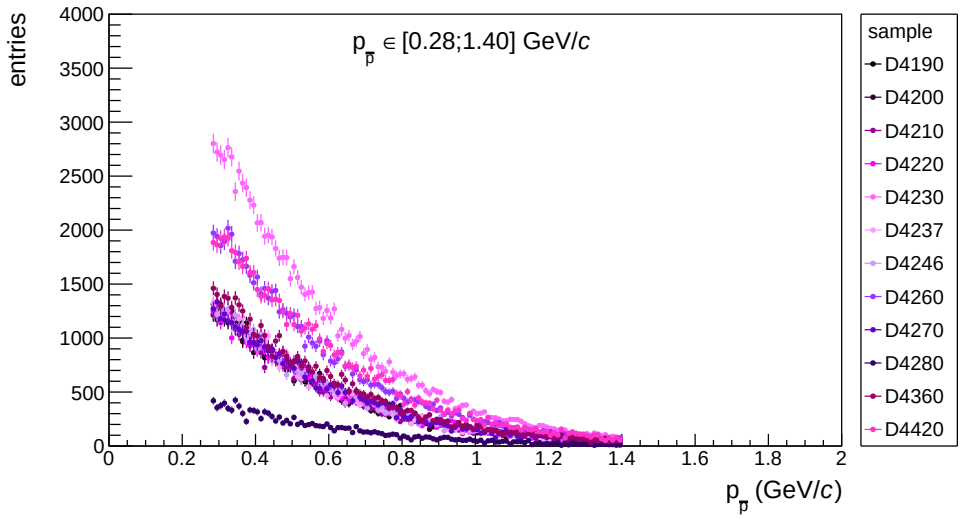

Figure B.2: (3.10) Sideband-subtracted momentum spectra of reconstructed MC antiprotons with applied selections (table 5).

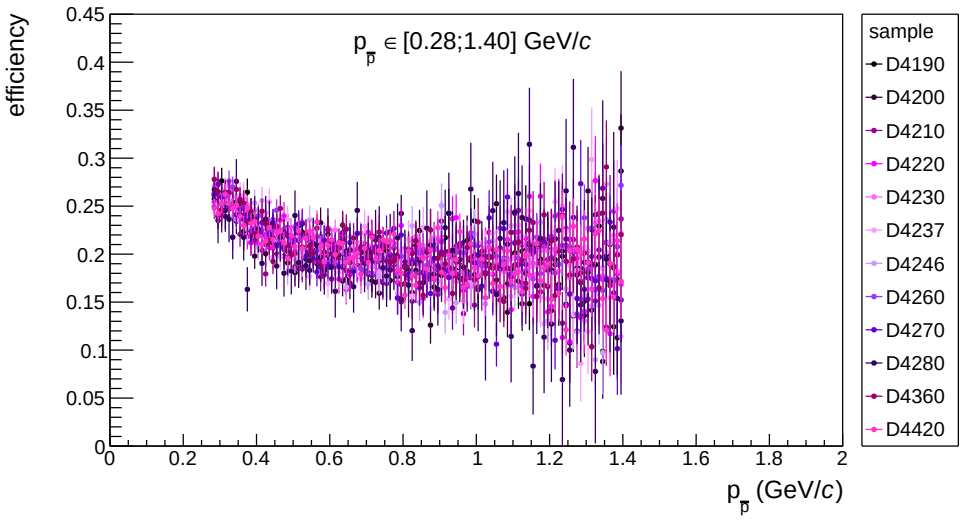

Figure B.3: (3.11) Distributions of reconstruction efficiency per antiproton momentum bin with applied selections (table 5).

B.2. Yield Measurement

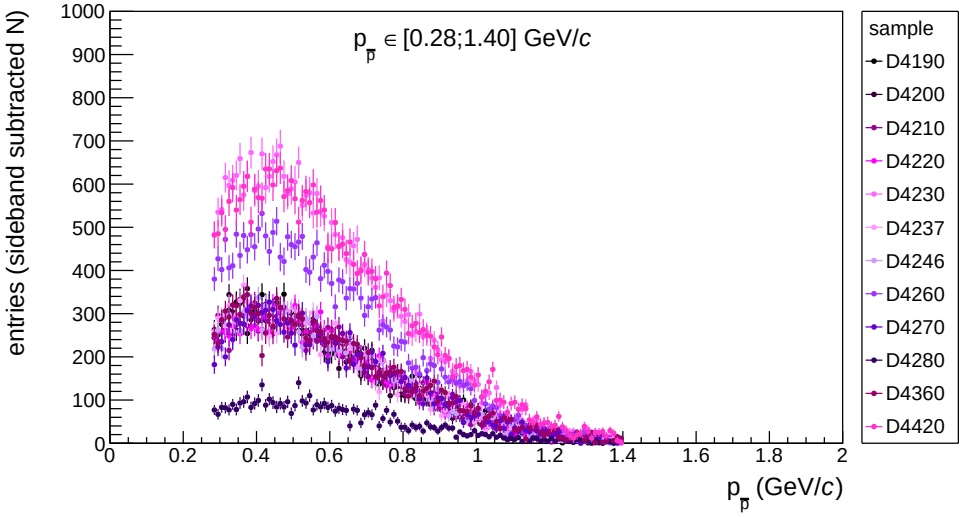

Figure B.4: (3.12) Sideband subtracted momentum spectra of reconstructed antiprotons from $\bar{\Lambda}^0$ candidates of measured data with applied selections (table 5).

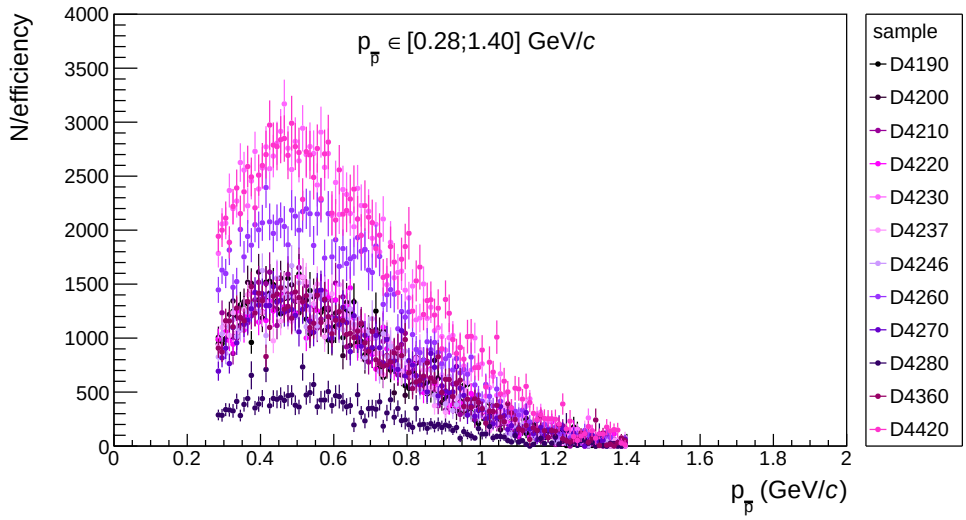

Figure B.5: (3.13) Sideband-subtracted momentum distribution of reconstructed antiprotons from $\bar{\Lambda}^0$ candidates divided by the reconstruction efficiency with applied selections (table 5).

B.3. The Antiproton Momentum Cut

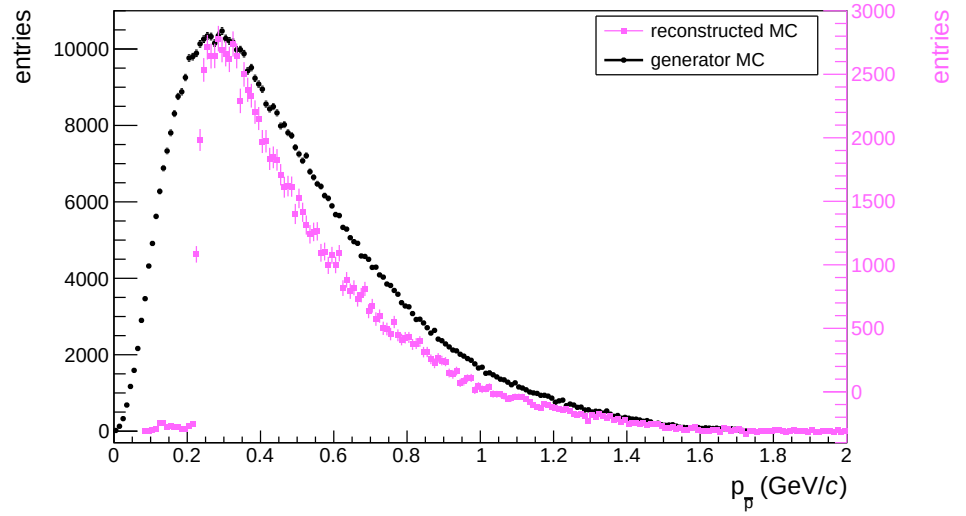

Figure B.6: (3.17) *Generic MC* of D4230: Momentum spectra of antiprotons from $\bar{\Lambda}^0$ cancidates before (black, left scale) and after (pink, right scale) passing the reconstruction procedure.

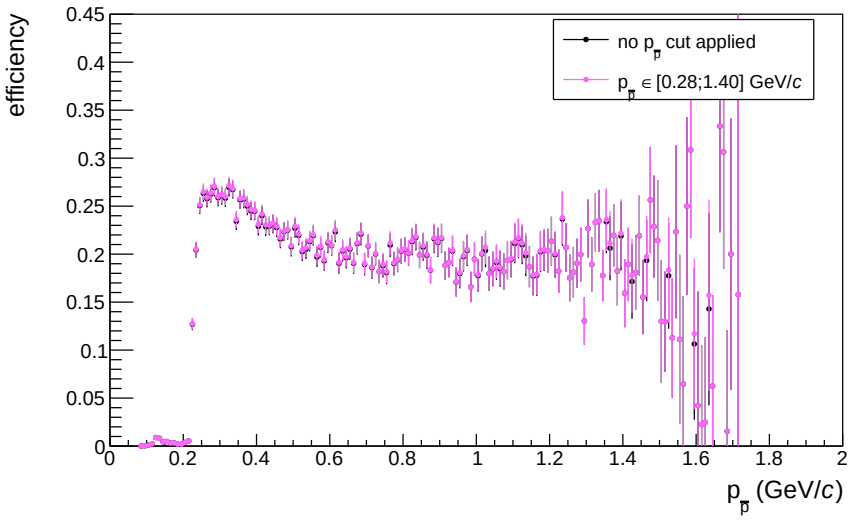

Figure B.7: (3.18) Reconstruction efficiency distributions of antiprotons from $\bar{\Lambda}^0$ candidates of D4230 with and without applied momentum cut.

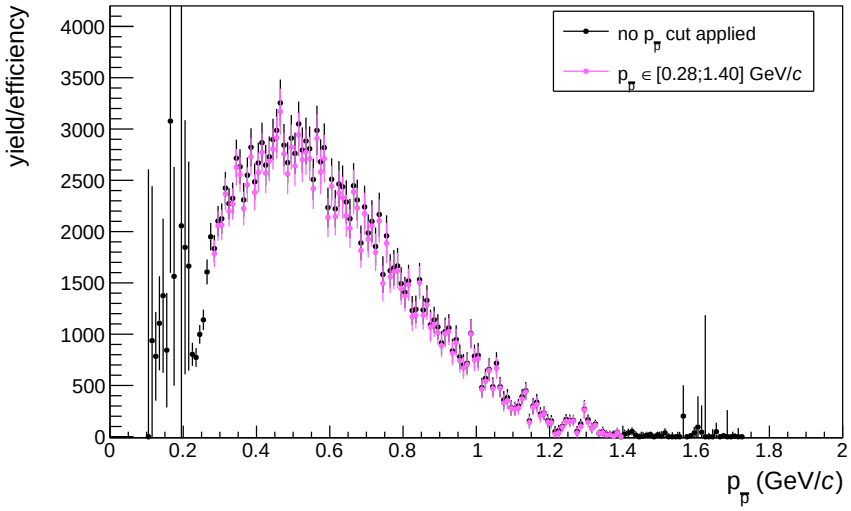

Figure B.8: (3.18) Efficiency-corrected yield distributions of antiprotons from $\bar{\Lambda}^0$ candidates of D4230 with and without applied momentum cut.

C. Acceptance Correction

Figure C.1 and figure C.2 show the acceptance of (anti-)protons of the Λ^0 ($\bar{\Lambda}^0$) reconstruction in dependence on the center-of-mass energy $\sqrt{s}$. Each subfigure shows three acceptance distributions of different high proton momentum cuts (p_{high}). The lower proton momentum cut is exemplarily chosen: $p_{low} = 0.20\,\mathrm{GeV}/c$ (figure C.1) and $p_{low} = 0.50\,\mathrm{GeV}/c$ (figure C.2). The course of the three acceptance distributions in each subfigure are nearby each other (the difference between all three is smaller than 0.01). Then again, the slopes of the distributions (fit functions) in figure C.2 are significantly steeper than those in figure C.1. This leads to the conclusion, that a more rigourous cut ($0.50\,\mathrm{GeV}/c$) affects data samples of low center-of-mass energies more than those of high energies.

Overall, it can be noted that the influence of p_{high} is less pronounced than the one of p_{low}. This sensitivity of the data samples on p_{low} is another motivation to scan this area in fine increments to determine the optimal proton momentum cut (section 3.6.1).

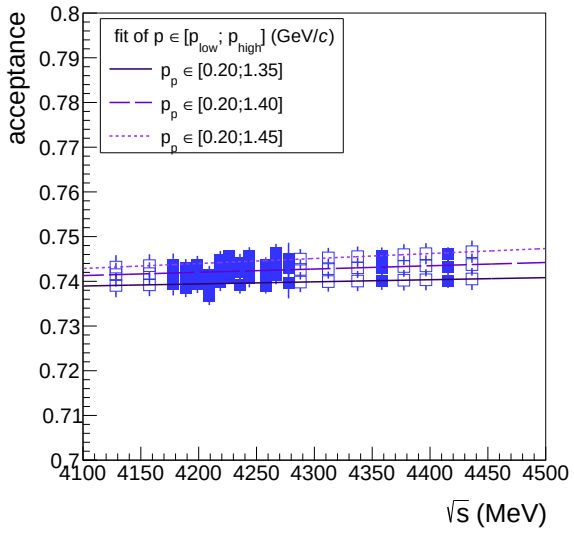

(a) Acceptance of p

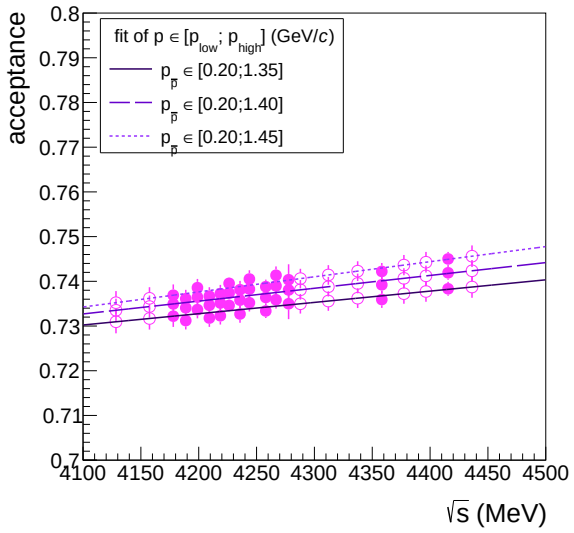

(b) Acceptance of $\overline{p}$

Figure C.1: Detector acceptance in dependence on $\sqrt{s}$. The three high p_p ($p_{\overline{p}}$) cuts are shown with one selected low cut: $p_{low} = 0.20\,\mathrm{GeV}/c$. Open symbols represent interpolated values as there is no *generic MC* for some data samples. An angular cut is applied.

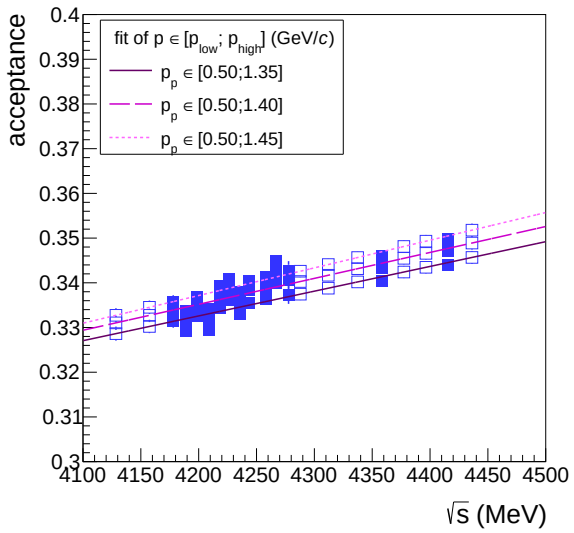

(a) Acceptance of p

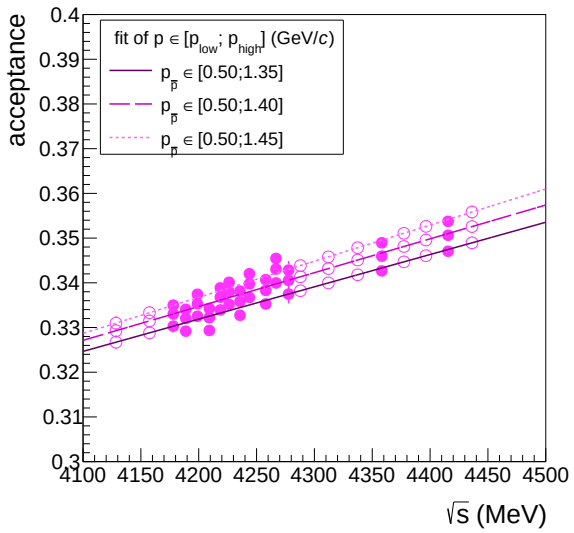

(b) Acceptance of $\overline{p}$

Figure C.2: Detector acceptance in dependence on $\sqrt{s}$. The three high p_p ($p_{\overline{p}}$) cuts are shown with one selected low cut: $p_{low} = 0.50\,\mathrm{GeV}/c$. Open symbols represent interpolated values as there is no *generic MC* for some data samples. An angular cut is applied.

D. Systematic Uncertainties - All Look-Up Tables

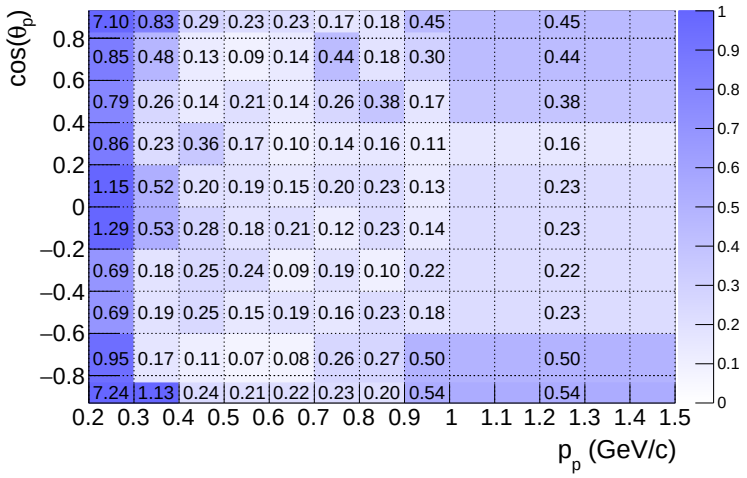

Figure D.1: PID uncertainty (δ_i) of p (in %) per $(\cos(\theta_p), p)$ bin.

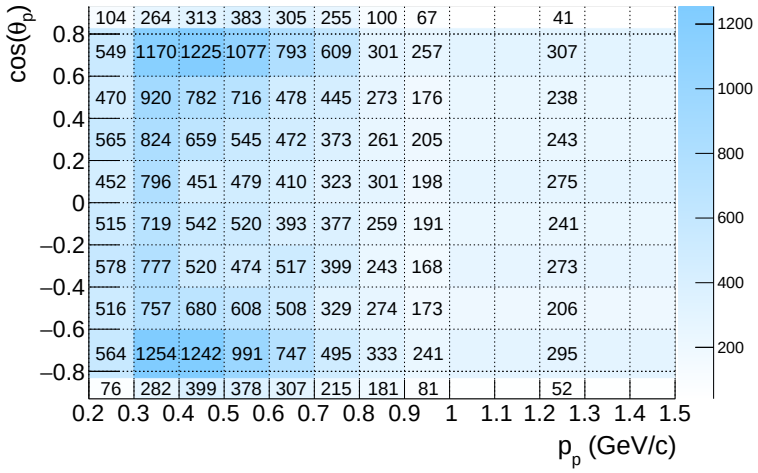

Figure D.2: Sideband-subtracted multiplicity of p per $(\cos(\theta_p), p)$ bin, $N_{total} = 8466$.

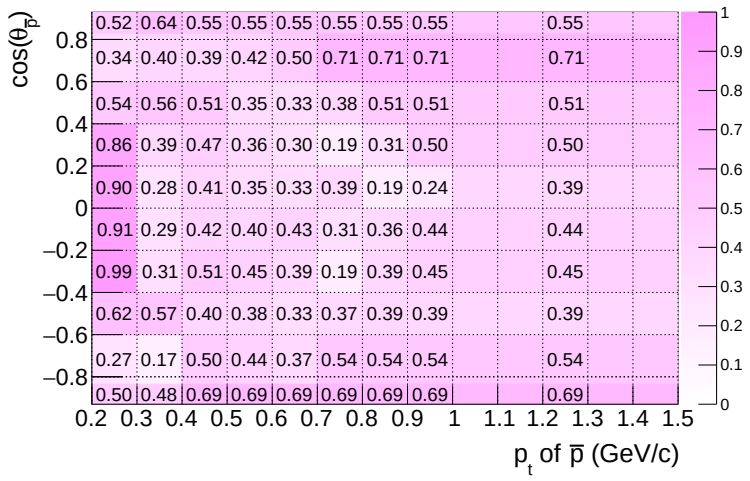

Figure D.3: Tracking uncertainty of $\overline{p}$ (in %) per $(\cos(\theta_{\overline{p}}), p_t)$ bin.

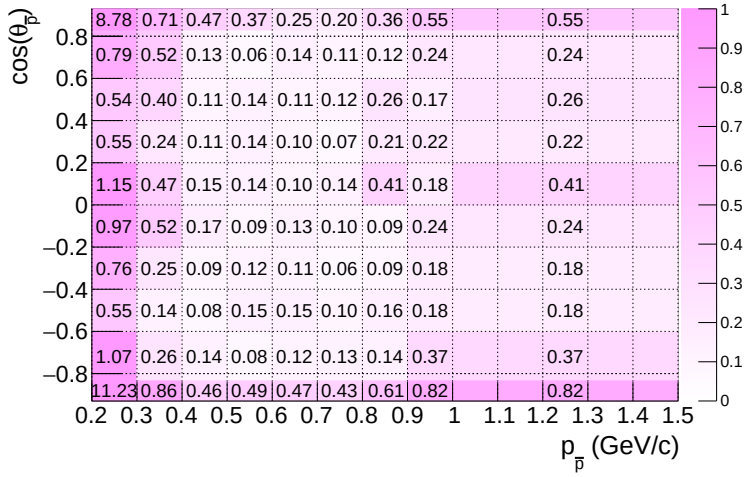

Figure D.4: PID uncertainty of $\overline{p}$ (in %) per $(\cos(\theta_{\overline{p}}), p_{\overline{p}})$ bin.

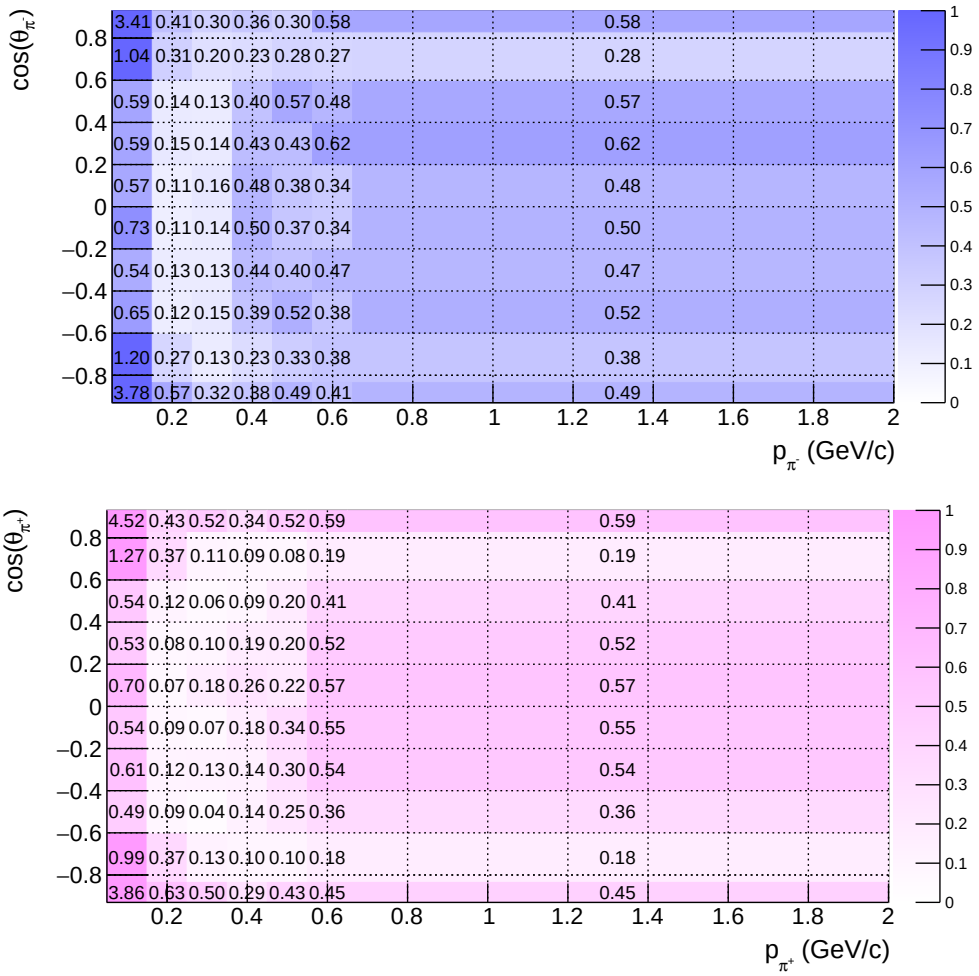

Figure D.5: PID uncertainty of π^- (upper figure) and π^+ per $(\cos(\theta_\pi), p_\pi)$ bin.

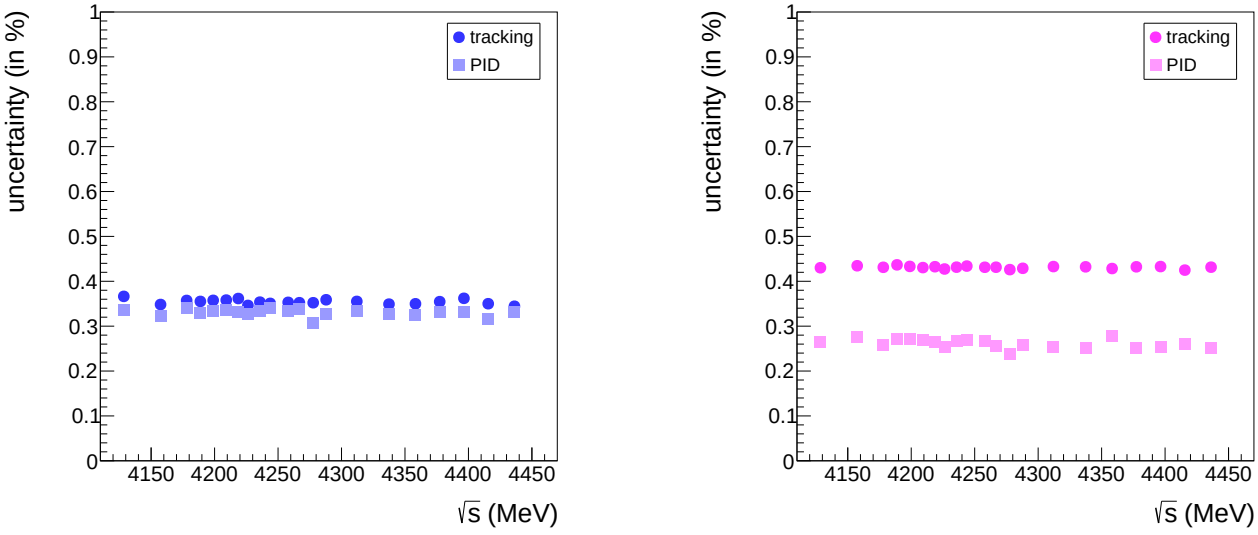

(a) Tracking and PID uncertainty of p

(b) Tracking and PID uncertainty of $\overline{p}$

Figure D.6: Tracking and PID uncertainty of (anti-)protons

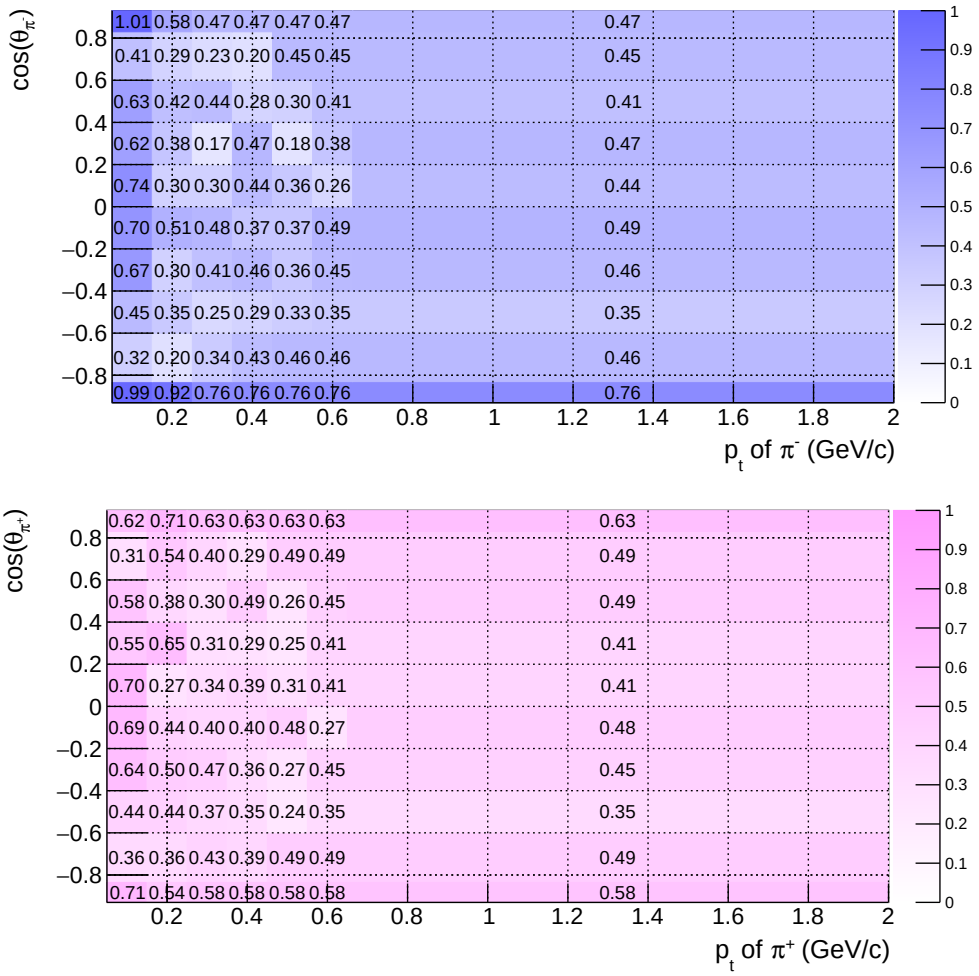

Figure D.7: Tracking uncertainty of π^- (upper figure) and π^+ per $(\cos(\theta_\pi), p_t)$ bin.

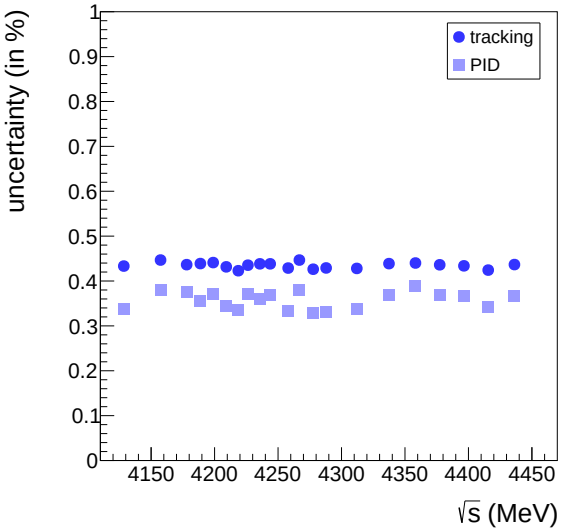

(a) Tracking and PID uncertainty of π^-

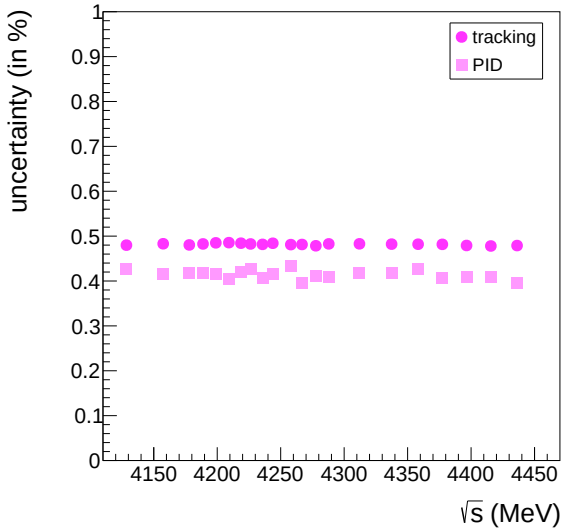

(b) Tracking and PID uncertainty of π^+

Figure D.8: Tracking and PID uncertainty of π^- and π^+

List of Acronyms

BEPC Beijing Electron-Positron Collider

BEPCII Beijing Electron-Positron Collider II

BES Beijing Spectrometer

BESIII Beijing Spectrometer III

BNL Brookhaven National Laboratory

BOSS BESIII Offline Software System

CDF Collider Detector at Fermilab

CERN Conseil Européenne pour la Recherche Nucléaire

CKM Cabibbo-Kobayashi-Maskawa

CMT Configuration Management Tool

CP Charge Parity

DST Data Summary Tape

EMC Electromagnetic Calorimeter

FWHM Full Width at Half Maximum

Geant4 **Ge**ometry **an**d **t**racking

IHEP Institute for High Energy Physics

INFN Istituto Nazionale di Fisica Nucleare

IP Interaction Point

ISR Initial State Radiation

KEK Kō Enerugī Kasokuki Kenkyū Kikō

KKMC KK Monte Carlo

LHC Large Hadron Collider

LINAC Linear Accelerator

MC Monte Carlo

MC *Monte Carlo*

MDC Multilayer Drift Chamber

PDG Particle Data Group

PID Particle Identification

PMT Photomultiplyer

RPC Resistive Plate Chambers

SCQ Superconducting Quadrupoles

SLAC Stanford Linear Accelerator Center

SM Standard Model

SSM Superconducting Solenoid Magnet

TOF Time-of-Flight system

QCD Quantum Chromodynamics

QED Quantum Electrodynamics

List of Figures

List of Tables

Bibliography

[1] Stephen Weinberg. A Model of Leptons. Phys. Rev. Lett., 19:1264, 1967. URL https://journals.aps.org/prl/pdf/10.1103/PhysRevLett.19.1264.

[2] wikipedia. https://en.wikipedia.org/wiki/Standard_Model, 2022.

[3] Georges Aad et al. Combined Measurement of the Higgs Boson Mass in pp Collisions at $\sqrt{s} = 7$ and 8 TeV with the ATLAS and CMS Experiments. Phys. Rev. Lett., 114: 191803, 2015. doi: 10.1103/PhysRevLett.114.191803.

[4] Peter W. Higgs. Broken Symmetries and the Masses of Gauge Bosons. Phys. Rev. Lett., 13:508–509, 1964. doi: 10.1103/PhysRevLett.13.508.

[5] M. Gell-Mann. A schematic model of baryons and mesons. Physics Letters, 8(3):214–215, 1964. ISSN 0031-9163. doi: https://doi.org/10.1016/S0031-9163(64)92001-3. URL https://www.sciencedirect.com/science/article/pii/S0031916364920013.

[6] G. Zweig. An SU(3) model for strong interaction symmetry and its breaking. Version 1. Jan 1964.

[7] E. D. Bloom et al. High-energy inelastic $e-p$ scattering at 6° and 10°. Phys. Rev. Lett., 23:930–934, Oct 1969. doi: 10.1103/PhysRevLett.23.930. URL https://link.aps.org/doi/10.1103/PhysRevLett.23.930.

[8] A. J. Buchmann. Structure of strange baryons. In Proceedings of The IX International Conference on Hypernuclear and Strange Particle Physics, pages 329–333, Berlin, Heidelberg, 2007. Springer Berlin Heidelberg. ISBN 978-3-540-76367-3.

[9] Zhengguo Zhao. R values in low energy e^+e^- annihilation. URL https://www.slac.stanford.edu/econf/C990809/docs/zhao.pdf.

[10] J. Huston, K. Rabbertz, and Zanderighi; G. Quantum chromodynamics. 23, Aug 2021. doi: 10.1103/PhysRevLett.23.930. URL https://pdg.lbl.gov/2021/reviews/rpp2021-rev-qcd.pdf.

[11] B. Povh, K. Rith, C. Scholz, and F. Zetsche. Teilchen und Kerne. Springer, 6 edition, 2004. ISBN 3-540-21065-2.

[12] N. Brambilla et al. The XYZ states: Experimental and theoretical status and perspectives. Physics Reports, 873:1–154, Aug 2020. doi: 10.1016/j.physrep.2020.05.001. URL https://doi.org/10.1016%2Fj.physrep.2020.05.001.

[13] David Griffiths. Introduction to Elementary Particles. Wiley-VCH, 2 edition, 2008. ISBN 978-3527406012.

[14] M. Tanabashi et al. Review of Particle Physics. Phys. Rev. D, 98(3):030001, 2018. doi: 10.1103/PhysRevD.98.030001.

[15] J. E. Augustin, A. M. Boyarski, Breidenbach, et al. Discovery of a narrow resonance in e^+e^- annihilation. Phys. Rev. Lett., 33:1406–1408, Dec 1974. doi: 10.1103/PhysRevLett.33.1406. URL https://link.aps.org/doi/10.1103/PhysRevLett.33.1406.

[16] J. J. Aubert, U. Becker, P. J. Biggs, et al. Experimental observation of a heavy particle J. Phys. Rev. Lett., 33:1404–1406, Dec 1974. doi: 10.1103/PhysRevLett.33.1404. URL https://link.aps.org/doi/10.1103/PhysRevLett.33.1404.

[17] V. Luth et al. The Quantum Numbers and Decay Widths of the psi-prime (3684). Phys. Rev. Lett., 35:1124–1126, 1975. doi: 10.1103/PhysRevLett.35.1124.

[18] E. G. Cazzoli et al. Evidence for $\Delta s = -\Delta q$ currents or charmed-baryon production by neutrinos. Phys. Rev. Lett., 34:1125–1128, Apr 1975. doi: 10.1103/PhysRevLett.34.1125. URL https://link.aps.org/doi/10.1103/PhysRevLett.34.1125.

[19] C. P. Shen et al. Evidence for a new resonance and search for the Y(4140) in the $\gamma\gamma \to \phi J/\psi$ process. Phys. Rev. Lett., 104:112004, 2010. doi: 10.1103/PhysRevLett.104.112004.

[20] C. A. Meyer and Y. Van Haarlem. Status of exotic-quantum-number mesons. Physical Review C, 82(2), Aug 2010. doi: 10.1103/physrevc.82.025208. URL https://doi.org/10.1103%2Fphysrevc.82.025208.

[21] S. Dubynskiy and M.B. Voloshin. Hadro-charmonium. Physics Letters B, 666(4):344–346, Sep 2008. doi: 10.1016/j.physletb.2008.07.086. URL https://doi.org/10.1016%2Fj.physletb.2008.07.086.

[22] T. Barnes, F. E. Close, and E. S. Swanson. Hybrid and conventional mesons in the flux tube model: Numerical studies and their phenomenological implications. Physical Review D, 52(9):5242–5256, Nov 1995. doi: 10.1103/physrevd.52.5242. URL https://doi.org/10.1103%2Fphysrevd.52.5242.

[23] Eric S. Swanson. The new heavy mesons: A status report. Physics Reports, 429(5), Jul 2006. doi: 10.1016/j.physrep.2006.04.003. URL https://doi.org/10.1016%2Fj.physrep.2006.04.003.

[24] Gunnar S. Bali. Lattice calculations of hadron properties. The European Physical Journal A, 19(S1):1–8, Feb 2004. doi: 10.1140/epjad/s2004-03-001-5. URL https://doi.org/10.1140%2Fepjad%2Fs2004-03-001-5.

[25] S.-K. Choi et al. Observation of a narrow charmoniumlike state in exclusive $B^{\pm} \to K^{\pm}\pi^{+}\pi^{-}J/\psi$ decays. Phys. Rev. Lett., 91:262001, Dec 2003. doi: 10.1103/PhysRevLett.91.262001. URL https://link.aps.org/doi/10.1103/PhysRevLett.91.262001.

[26] B. Aubert et al. The BABAR detector. Nuc. Inst. and Methods in Phys. Research Sect. A: Accelerators, Spectrometers, Detectors and Associated Equipment, 479(1):1–116, Feb 2002. URL https://doi.org/10.1016%2Fs0168-9002%2801%2902012-5.

[27] A. Augusto Alves, Jr. et al. The LHCb Detector at the LHC. JINST, 3:S08005, 2008. doi: 10.1088/1748-0221/3/08/S08005.

[28] M. Ablikim et al. Design and Construction of the BESIII Detector. https://arxiv.org/pdf/0911.4960.pdf, 2009.

[29] A. Abashian et al. The Belle Detector. Nucl. Instrum. Meth. A, 479:117–232, 2002. doi: 10.1016/S0168-9002(01)02013-7.

[30] Xiang Liu. An overview of XYZ new particles. Chinese Science Bulletin, 59(29-30):3815–3830, May 2014. doi: 10.1007/s11434-014-0407-2. URL https://doi.org/10.1007%2Fs11434-014-0407-2.

[31] S.-K. Choi et al. Observation of a narrow charmoniumlike state in exclusive $B^{\pm} \to K^{\pm}\pi^{+}\pi^{-}J/\psi$ decays. Phys. Rev. Lett., 91:262001, Dec 2003. doi: 10.1103/PhysRevLett.91.262001. URL https://link.aps.org/doi/10.1103/PhysRevLett.91.262001.

[32] D. Acosta et al. Observation of the narrow state $X(3872) \to J/\psi\pi^{+}\pi^{-}$ in $\bar{p}p$ collisions at $\sqrt{s} = 1.96$ TeV. Phys. Rev. Lett., 93:072001, Aug 2004. doi: 10.1103/PhysRevLett.93.072001. URL https://link.aps.org/doi/10.1103/PhysRevLett.93.072001.

[33] B. Aubert et al. Study of the $B^{-} \to J/\psi K^{-}\pi^{+}\pi^{-}$ decay and measurement of the $B^{-} \to X(3872)K^{-}$ branching fraction. Phys. Rev. D, 71:071103, Apr 2005. URL https://link.aps.org/doi/10.1103/PhysRevD.71.071103.

[34] R. Aaij et al. Determination of the $X(3872)$ Meson Quantum Numbers. Phys. Rev. Lett., 110:222001, May 2013. doi: 10.1103/PhysRevLett.110.222001. URL https://link.aps.org/doi/10.1103/PhysRevLett.110.222001.

[35] Qi Wu, Dian-Yong Chen, and Takayuki Matsuki. A phenomenological analysis on isospin-violating decay of $X(3872)$. The European Physical Journal, 81, Feb 2021. URL https://link.springer.com/content/pdf/10.1140/epjc/s10052-021-08984-2.pdf.

[36] J. Vijande, F. Fernández, and A. Valcarce. Describing non-$q\overline{q}$ candidates. International Journal of Modern Physics A, 20(02n03):702–704, 2005. doi: 10.1142/S0217751X05022214. URL https://doi.org/10.1142/S0217751X05022214.

[37] F.E Close and Stephen Godfrey. Charmonium hybrid production in exclusive B-meson decays. Physics Letters B, 574(3):210–216, 2003. ISSN 0370-2693. doi: https://doi.org/10.1016/j.physletb.2003.09.011. URL https://www.sciencedirect.com/science/article/pii/S0370269303013534.

[38] M.B. Voloshin. Interference and binding effects in decays of possible molecular component of $X(3872)$. Physics Letters B, 579(3-4):316–320, Jan 2004. doi: 10.1016/j.physletb.2003.11.014. URL https://doi.org/10.1016%2Fj.physletb.2003.11.014.

[39] M. Ablikim et al. Observation of $e^{+}e^{-} \to \gamma X(3872)$ at BESIII. Phys. Rev. Lett., 112:092001, Mar 2014. doi: 10.1103/PhysRevLett.112.092001. URL https://link.aps.org/doi/10.1103/PhysRevLett.112.092001.

[40] S.-K. Choi et al. Observation of a resonancelike structure in the $\pi^{\pm}\psi^{'}$ mass distribution in exclusive $B \to K\pi^{\pm}\psi^{'}$ decays. Phys. Rev. Lett., 100:142001, Apr 2008. URL https://link.aps.org/doi/10.1103/PhysRevLett.100.142001.

[41] M Ablikim et al. Observation of a Charged Charmoniumlike Structure in $e^{+}e^{-} \to J/\psi\pi^{+}\pi^{-}$ at $\sqrt{s}$=4.26 GeV. In 30 Years of BES Physics: Proceedings of the Symposium, pages 229–235. World Scientific, 2013.

[42] M. Ablikim et al. Observation of a charged $(D\overline{D}^{*})^{\pm}$ mass peak in $e^{+}e^{-} \to \pi d\overline{d}^{*}$ at $\sqrt{s} = 4.26$ GeV. Phys. Rev. Lett., 112:022001, Jan 2014. doi: 10.1103/PhysRevLett.112.022001. URL https://link.aps.org/doi/10.1103/PhysRevLett.112.022001.

[43] M Ablikim et al. Observation of a Charged Charmoniumlike Structure $Z_c(4020)$ and Search for the $Z_c(3900)$ in $e^+e^- \to h_c\pi^+\pi^-$. Phys. Rev. Lett., 111(24):242001, Dec 2013. doi: 10.1103/PhysRevLett.111.242001. URL https://link.aps.org/doi/10.1103/PhysRevLett.111.242001.

[44] M. Ablikim et al. Observation of $e^+e^- \to \pi^0\pi^0 h_c$ and a neutral charmoniumlike structure $Z_c(4020)^0$. Phys. Rev. Lett., 113:212002, Nov 2014. doi: 10.1103/PhysRevLett.113.212002. URL https://link.aps.org/doi/10.1103/PhysRevLett.113.212002.

[45] M. Ablikim et al. Evidence of Two Resonant Structures in $e^+e^- \to \pi^+\pi^- h_c$. Phys. Rev. Lett., 118:092002, Mar 2017. doi: 10.1103/PhysRevLett.118.092002. URL https://link.aps.org/doi/10.1103/PhysRevLett.118.092002.

[46] M. Ablikim et al. Observation of the $Y(4230)$ and a new structure in $e^+e^- \to K^+K^- J/\psi$, Apr 2022.

[47] J. Siegrist et al. Observation of a resonance at 4.4 GeV and additional structure near 4.1 GeV in e^+e^- annihilation. Phys. Rev. Lett., 36:700–703, Mar 1976. URL https://link.aps.org/doi/10.1103/PhysRevLett.36.700.

[48] Bernard Aubert et al. Exclusive Initial-State-Radiation Production of the D anti-D, D^* anti-D^*, and D^* anti-D^* Systems. Phys. Rev. D, 79:092001, 2009. doi: 10.1103/PhysRevD.79.092001.

[49] G. Pakhlova et al. Measurement of the near-threshold $e^+e^- \to D$ anti-D cross section using initial-state radiation. Phys. Rev. D, 77:011103, 2008. doi: 10.1103/PhysRevD.77.011103.

[50] G. Pakhlova et al. Observation of $\psi(4415) \to D\bar{D}_2^*(2460)$ decay using initial-state radiation. Phys. Rev. Lett., 100:062001, 2008. doi: 10.1103/PhysRevLett.100.062001.

[51] T. Barnes, S. Godfrey, and E. S. Swanson. Higher charmonia. Phys. Rev. D, 72:054026, Sep 2005. doi: 10.1103/PhysRevD.72.054026. URL https://link.aps.org/doi/10.1103/PhysRevD.72.054026.

[52] Bernard Aubert et al. Observation of a broad structure in the $\pi^+\pi^- J/\psi$ mass spectrum around 4.26 GeV/c^2. Phys. Rev. Lett., 95:142001, 2005. doi: 10.1103/PhysRevLett.95.142001.

[53] C. Z. Yuan et al. Measurement of the $e^+e^- \to \pi^+\pi^- J/\psi$ cross section via initial-state radiation at Belle. Phys. Rev. Lett., 99:182004, Nov 2007. doi: 10.1103/PhysRevLett.99.182004. URL https://link.aps.org/doi/10.1103/PhysRevLett.99.182004.

[54] Q. He et al. Confirmation of the $Y(4260)$ resonance production in initial state radiation. Phys. Rev. D, 74:091104, Nov 2006. doi: 10.1103/PhysRevD.74.091104. URL https://link.aps.org/doi/10.1103/PhysRevD.74.091104.

[55] T. Barnes. Hadron05 summary: Heavy quark hadrons and theory. 814, Oct 2005. doi: 10.1063/1.2176573. URL https://www.researchgate.net/figure/The-Y4260-reported-by-BaBar-in-the-ISR-process-e-e-g-ISR-J-psp-p-8_fig2_2017713.

[56] M. Ablikim et al. Precise measurement of the $e^+e^- \to \pi^+\pi^- J/\psi$ cross section at center-of-mass energies from 3.77 to 4.60 GeV. Phys. Rev. Lett., 118:092001, Mar 2017. doi: 10.1103/PhysRevLett.118.092001. URL https://link.aps.org/doi/10.1103/PhysRevLett.118.092001.

[57] R. L. Workman and Others. Review of Particle Physics. PTEP, 2022:083C01, 2022. doi: 10.1093/ptep/ptac097.

[58] M. Ablikim et al. Observation of a charged $(D\bar{D}^*)^\pm$ mass peak in $e^+e^- \to \pi D\bar{D}^*$ at $\sqrt{s} =$ 4.26 GeV . Phys. Rev. Lett., 112(2):022001, 2014. doi: 10.1103/PhysRevLett.112.022001.

[59] M. Ablikim et al. Determination of the $\psi(3770)$, $\psi(4040)$, $\psi(4160)$ and $\psi(4415)$ resonance parameters. eConf, C070805:02, 2007. doi: 10.1016/j.physletb.2007.11.100.

[60] M. Ablikim et al. Observation of a Charged Charmoniumlike Structure in $e^+e^- \to \pi^+\pi^- J/\psi$ at $\sqrt{s}$ =4.26 GeV. Phys. Rev. Lett., 110:252001, 2013. doi: 10.1103/PhysRevLett.110.252001.

[61] M. Ablikim et al. Study of the process $e^+e^- \to \pi^0\pi^0 J/\psi$ and neutral charmoniumlike state $Z_c(3900)^0$. Phys. Rev. D, 102:012009, Jul 2020. doi: 10.1103/PhysRevD.102.012009. URL https://link.aps.org/doi/10.1103/PhysRevD.102.012009.

[62] T. Barnes, F. E. Close, and E. S. Swanson. Hybrid and conventional mesons in the flux tube model: Numerical studies and their phenomenological implications. Phys. Rev. D, 52:5242–5256, 1995. URL https://link.aps.org/doi/10.1103/PhysRevD.52.5242.

[63] Shi-Lin Zhu. The possible interpretations of Y(4260). Physics Letters B, 625(3-4):212–216, Oct 2005. doi: 10.1016/j.physletb.2005.08.068. URL https://doi.org/10.1016%2Fj.physletb.2005.08.068.

[64] Martin Cleven, Qian Wang, Feng-Kun Guo, Christoph Hanhart, Ulf-G. Meißner, and Qiang Zhao. Physical Review D, 90(7), Oct 2014. doi: 10.1103/physrevd.90.074039. URL https://doi.org/10.1103%2Fphysrevd.90.074039.

[65] Martin Cleven, Qian Wang, Feng-Kun Guo, Christoph Hanhart, Ulf-G. Meißner, and Qiang Zhao. $Y(4260)$ as the first s-wave open charm vector molecular state? Phys. Rev. D, 90:074039, Oct 2014. doi: 10.1103/PhysRevD.90.074039. URL https://link.aps.org/doi/10.1103/PhysRevD.90.074039.

[66] L. Maiani, F. Piccinini, A. D. Polosa, and V. Riquer. Four quark interpretation of $Y(4260)$. Phys. Rev. D, 72:031502, Aug 2005. doi: 10.1103/PhysRevD.72.031502. URL https://link.aps.org/doi/10.1103/PhysRevD.72.031502.

[67] Xin Li and M. Voloshin. Y(4260) and Y(4360) as mixed hadrocharmonium. Modern Physics Letters A, 29, Sep 2013. doi: 10.1142/S0217732314500606.

[68] Qian Wang, Christoph Hanhart, and Qiang Zhao. Decoding the riddle of $Y(4260)$ and $Z_c(3900)$. Phys. Rev. Lett., 111:132003, Sep 2013. doi: 10.1103/PhysRevLett.111.132003. URL https://link.aps.org/doi/10.1103/PhysRevLett.111.132003.

[69] M. Ablikim et al. Measurements of $e^+e^- \to \eta_c\pi^+\pi^-\pi^0$, $\eta_c\pi^+\pi^-$ and $\eta_c\pi^0\gamma$ at $\sqrt{s}$ from 4.18 to 4.60 GeV, and search for a Z_c state close to the $D\bar{D}$ threshold decaying to $\eta_c\pi$ at $\sqrt{s} = 4.23$ GeV. Phys. Rev. D, 103(3):032006, 2021. doi: 10.1103/PhysRevD.103.032006.

[70] M. Ablikim et al. Cross section measurement of $e^+e^- \to \pi^+\pi^-(3686)$ from $\sqrt{s} = 4.0076$ to 4.6984 GeV. Phys. Rev. D, 104(5):052012, 2021. doi: 10.1103/PhysRevD.104.052012.

[71] Felipe J. Llanes-Estrada. Y(4260) and possible charmonium assignment. Physical Review D, 72(3), Aug 2005. doi: 10.1103/physrevd.72.031503. URL https://doi.org/10.1103%2Fphysrevd.72.031503.

[72] P. A. Rapidis et al. Observation of a resonance in e^+e^- annihilation just above charm threshold. Phys. Rev. Lett., 39:526–529, Aug 1977. doi: 10.1103/PhysRevLett.39.526. URL https://link.aps.org/doi/10.1103/PhysRevLett.39.526.

[73] G. Goldhaber et al. D^0 and $D^{\pm}$ meson production near 4 GeV in e^+e^- annihilation. Physics Letters B, 69(4):503–507, 1977. URL https://www.sciencedirect.com/science/article/pii/0370269377908553.

[74] Medina Ablikim et al. Precise measurement of the $e^+e^- \to \pi^+\pi^- J/\psi$ cross section at center-of-mass energies from 3.77 to 4.60 GeV. Phys. Rev. Lett., page 092001, 2017. URL https://link.aps.org/doi/10.1103/PhysRevLett.118.092001.

[75] X. L. Wang et al. Physical Review Letters, 99(14), Oct 2007. doi: 10.1103/physrevlett.99.142002. URL https://doi.org/10.1103%2Fphysrevlett.99.142002.

[76] Bernard Aubert et al. Evidence of a broad structure at an invariant mass of 4.32- GeV/c^2 in the reaction $e^+e^- \to \pi^+\pi^-\psi_{2S}$ measured at BaBar. Phys. Rev. Lett., 98:212001, 2007. doi: 10.1103/PhysRevLett.98.212001.

[77] X. L. Wang et al. Observation of Two Resonant Structures in $e^+e^- \to \pi^+\pi^-\psi(2S)$ via Initial State Radiation at Belle. Phys. Rev. Lett., 99:142002, 2007. doi: 10.1103/PhysRevLett.99.142002.

[78] Bai-Qing Li and Kuang-Ta Chao. Higher charmonia and X, Y, Z states with screened potential. Physical Review D, 79(9):094004, 2009.

[79] Medina Ablikim et al. Cross section measurement of $e^+e^- \to p\bar{p}\eta$ and $e^+e^- \to p\bar{p}\omega$ at center-of-mass energies between 3.773 GeV and 4.6 GeV. Phys. Rev. D, 104(9):092008, 2021. doi: 10.1103/PhysRevD.104.092008.

[80] N. Brambilla et al. Heavy quarkonium: progress, puzzles, and opportunities. The European Physical Journal C, 71(2), Feb 2011. doi: 10.1140/epjc/s10052-010-1534-9. URL https://doi.org/10.1140%2Fepjc%2Fs10052-010-1534-9.

[81] M. Ablikim et al. Measurement of the cross section for $e^+e^- \to \Lambda\bar{\Lambda}$ and evidence of the decay $\psi(3770) \to \Lambda\bar{\Lambda}$. Phys. Rev. D, 104(9):L091104, 2021. doi: 10.1103/PhysRevD.104.L091104.

[82] D. M. Asner et al. Physics at BESIII. 2008. doi: 10.48550/ARXIV.0809.1869. URL https://arxiv.org/abs/0809.1869.

[83] M. Ablikim et al. Future physics programme of BESIII. Chinese Physics C, 44(4): 040001, Apr 2020. doi: 10.1088/1674-1137/44/4/040001. URL https://doi.org/10.1088/1674-1137/44/4/040001.

[84] Bernard Aubert et al. The BaBar Detector. Nucl. Instrum. Meth. A, 479:1–116, 2002. doi: 10.1016/S0168-9002(01)02012-5.

[85] A. Abashian et al. The Belle Detector. Nucl. Instrum. Meth. A, 479:117–232, 2002. doi: 10.1016/S0168-9002(01)02013-7.

[86] T. Abe et al. Achievements of KEKB. PTEP, 2013, Mar 2013. doi: 10.1093/ptep/pts102.

[87] https://www.claymath.org/millennium-problems.

[88] S. Bethke. Experimental tests of asymptotic freedom. Progress in Particle and Nuclear Physics, 58(2):351–386, 2007. ISSN 0146-6410. doi: https://doi.org/10.1016/j.ppnp.2006.06.001. URL https://www.sciencedirect.com/science/article/pii/S0146641006000615.

[89] Yu. A. Simonov. Chiral dynamics with confinement versus the standard chiral theory. Int. J. Mod. Phys. A, 36(33):2150248, 2021. doi: 10.1142/S0217751X21502481.

[90] Particle Data Group and P. A. et others Zyla. Review of Particle Physics. Progress of Theoretical and Experimental Physics, 2020(8), Aug 2020. ISSN 2050-3911. doi: 10.1093/ptep/ptaa104. URL https://doi.org/10.1093/ptep/ptaa104. 083C01.

[91] Chang-Zheng Yuan. Charmonium and charmoniumlike states at the BESIII experiment. National Science Review, 8(11), Oct 2021. ISSN 2095-5138. doi: 10.1093/nsr/nwab182. URL https://doi.org/10.1093/nsr/nwab182. nwab182.

[92] M. Ablikim et al. Precision measurements of $B(D^+ \to \mu^+\nu_\mu)$, the pseudoscalar decay constant f_{D^+}, and the quark mixing matrix element $|V_{\rm cd}|$. Phys. Rev. D, 89:051104, Mar 2014. URL https://link.aps.org/doi/10.1103/PhysRevD.89.051104.

[93] https://pdg.lbl.gov/2021/web/viewer.html?file=https://pdg.lbl.gov/2021/reviews/rpp2021-rev-d-dbar-mixing.pdf.

[94] J. P. Lees et al. Search for CP Violation in the Decay $\tau^- \to \pi^- K^0_S(\geq 0\pi^0)\nu_{tau}$. Phys. Rev. D, 85:031102, 2012. [Erratum: Phys.Rev.D 85, 099904 (2012)].

[95] https://accelconf.web.cern.ch/IPAC2012/talks/tuya03_talk.pdf, IPAC 2012.

[96] https://accelconf.web.cern.ch/l04/TALKS/MOP34_TALK.PDF.

[97] C.H. Yu et al. BEPCII Performance and Beam Dynamics Studies on Luminosity. In Proc. of International Particle Accelerator Conference (IPAC'16), pages 1014–1018, Jun 2016. URL http://jacow.org/ipac2016/papers/tuya01.pdf.

[98] https://root.cern/.

[99] http://paw.web.cern.ch/paw/.

[100] https://fortranwiki.org/fortran/show/HomePage.

[101] https://geant4.web.cern.ch/.

[102] J. Allison et al. Geant4 developments and applications. IEEE Transactions on Nuclear Science, 53(1):270–278, 2006. doi: 10.1109/TNS.2006.869826.

[103] https://www.slac.stanford.edu/comp/physics/geant4/Using_G4_and_GDML.html.

[104] S. Jadach, B. F. L. Ward, and Z. Was. The Precision Monte Carlo event generator KK for two fermion final states in e^+e^- collisions. Comput. Phys. Commun., 130:260–325, 2000. doi: 10.1016/S0010-4655(00)00048-5.

[105] D. J. Lange. The EvtGen particle decay simulation package. Nucl. Instrum. Meth. A, 462:152–155, 2001. doi: 10.1016/S0168-9002(01)00089-4.

[106] G. Barrand et al. GAUDI - A software architecture and framework for building HEP data processing applications. Computer Physics Communications, 140 (1):45–55, 2001. URL https://www.sciencedirect.com/science/article/pii/S0010465501002545. CHEP2000.

[107] Liang Yan et al. Lagrange multiplier method used in BESIII kinematic fitting. Chin. Phys. C, 34:204–209, 2010. doi: 10.1088/1674-1137/34/2/009.

[108] P. Avery. Applied Fitting Theory I: General Least Squares Theory. CBX-91-72, 1991.

[109] P. Avery. Applied Fitting Theory VI: Formulas for Kinematic Fitting. CBX-98-37, 1998.

[110] I. Adachi et al. First observation of the P-wave spin-singlet bottomonium states $h_b(1P)$ and $h_b(2P)$. Phys. Rev. Lett., 108:032001, 2012. doi: 10.1103/PhysRevLett.108.032001.

[111] Kazuo Abe et al. Observation of a new charmonium state in double charmonium production in e^+e^- annihilation at $\sqrt{s} \approx 10.6\,\text{GeV}$. Phys. Rev. Lett., 98:082001, 2007. doi: 10.1103/PhysRevLett.98.082001.

[112] Kuang-Ta Chao. Interpretations for the X(4160) observed in the double charm production at B factories. https://arxiv.org/pdf/0707.3982.pdf, 2008.

[113] P. Kisel, I. Kisel, P. Senger, I. Vassiliev, and M. Zyzak. Strange Particle Reconstruction by the Missing Mass Method. In Europ. Phys. Journal Web of Conferences, volume 173 of Europ. Phys. Journal Web of Conferences, page 04009, Feb 2018.

[114] https://epaper.kek.jp/IPAC2012/talks/tuya03_talk.pdf.

[115] L. Landau. On the energy loss of fast particles by ionization. J. Phys. (USSR), 8:201, 1944.

[116] D.H. Perkins. Introduction to High Energy Physics, 3rd edition. Addison-Wesley, 1987.

[117] V. P. Druzhinin, S. I. Eidelman, S. I. Serednyakov, and E. P. Solodov. Hadron production via e^+e^- collisions with initial state radiation. Reviews of Modern Physics, 83(4):1545–1588, Dec 2011. doi: 10.1103/revmodphys.83.1545. URL https://doi.org/10.1103%2Frevmodphys.83.1545.

[118] Frank Jegerlehner. Variations on photon vacuum polarization. Nov 2017.

[119] BESIII Collaboration, M. Ablikim, et al. Observation of the $Y(4230)$ and a new structure in $e^+e^- \to K^+K^-J/\psi$, Apr 2022.

[120] M. Ablikim et al. Measurements of cross section of $e^+e^- \to p\bar{p}\pi^0$ at center-of-mass energies between 4.008 and 4.600 GeV. Physics Letters B, 771, May 2017. doi: 10.1016/j.physletb.2017.05.033.

[121] M. Ablikim et al. Precision measurement of the integrated luminosity of the data taken by BESIII at center-of-mass energies between 3.810 GeV and 4.600 GeV. Chinese Physics C, 39, 2015. doi: DOI:10.1088/1674-1137/39/9/093001.

[122] Jiada Lu. Study of tracking uncertainty from $J/\psi \to p\bar{p}\pi^+\pi^-$. BESIII internal memo; lujd@ihep.ac.cn, May 2020.

[123] Jiada Lu. Study of particle identification efficiency and its systematic uncertainty from $J/\psi \to p\bar{p}\pi^+\pi^-$. BESIII internal memo; lujd@ihep.ac.cn, May 2020.

[124] W.-L. Yuan, X. Ai, X.-B. Ji, S.-J. Chen, Y. Zhang, L.-H. Wu, L.-L. Wang, and Y. Yuan. Study of tracking efficiency and its systematic uncertainty from $J/\psi \to p\bar{p}\pi^+\pi^-$ at besiii. Chinese Physics C, 40:026201, Feb 2016.

[125] R.L. Workman et al. (Particle Data Group). Review of Particle Physics. Prog. Theor. Exp. Phys., page 083C01, 2022. doi: 10.1093/ptep/ptaa104.

[126] Glen Cowen. CERN, pages 6–8, 2020. URL `https://pdg.lbl.gov/2020/reviews/rpp2020-rev-statistics.pdf`.

All cited webpages were lastly called in November 2022.

A black belt is a white belt
who never gave up.
– unknown –